Spring 2015

An investigation into the phenomenological relation between solar activity and nuclear beta-decay rates

Tasneem M. Mohsinally
Purdue University

Graduate School Form 30
Updated 1/15/2015

PURDUE UNIVERSITY
GRADUATE SCHOOL
Thesis/Dissertation Acceptance

This is to certify that the thesis/dissertation prepared

By Tasneem M. Mohsinally

Entitled

AN INVESTIGATION INTO THE PHENOMENOLOGICAL RELATION BETWEEN SOLAR ACTIVITY AND NUCLEAR BETA-DECAY RATES

For the degree of Doctor of Philosophy

Is approved by the final examining committee:

Ephraim Fischbach
Chair

Andrew S. Hirsch

John P. Finley

Virgil E. Barnes

To the best of my knowledge and as understood by the student in the Thesis/Dissertation Agreement, Publication Delay, and Certification Disclaimer (Graduate School Form 32), this thesis/dissertation adheres to the provisions of Purdue University's "Policy of Integrity in Research" and the use of copyright material.

Approved by Major Professor(s): Ephraim Fischbach

Approved by: Andrew S. Hirsch 4/22/2015

Head of the Departmental Graduate Program Date

AN INVESTIGATION INTO THE PHENOMENOLOGICAL RELATION BETWEEN SOLAR ACTIVITY AND NUCLEAR BETA-DECAY RATES

A Dissertation

Submitted to the Faculty

of

Purdue University

by

Tasneem M. Mohsinally

In Partial Fulfillment of the

Requirements for the Degree

of

Doctor of Philosophy

May 2015

Purdue University

West Lafayette, Indiana

For my Father, and equally my Mother.

ACKNOWLEDGMENTS

I would like to thank my advisor, Ephraim Fischbach for his extraordinary support during this thesis process. Ephraim's eternal optimism supported me through this endeavor and helped me to see the light at the end of the tunnel. His guidance has been invaluable in shaping the kind of educator and researcher I hope to become. I would also like to thank my committee members Dr. Andrew Hirsch, Dr. John Finley, and Dr. Virgil Barnes for their patience, instruction and support during my time at Purdue.

I would like to thank Jere Jenkins for all his efforts in helping me understand the numerous intricacies that are involved in designing a viable experiment, and dealing with the unforeseeable hiccups along the way, as well as Dr. Peter Sturrock, Tom Gruenwald and Robert Lee for their direction and assistance. Additionally, special thanks are given to Daniel O'Keefe and Michael Czerny for their early involvement in this project, and especially to Sean Fancher whose insight and contribution has been essential to me.

A significant amount of gratitude goes out to Jonathan Nistor and Jordan Heim, great friends and colleagues, without whom this work would not have been possible. Their aid and advice, in matters both scientific and otherwise, cannot be measured and for which I will always be indebted. I wish them success in their future pursuits as they have always helped me to achieve mine.

Finally, I would like to extend my thanks to the Physics Department for their financial support and exemplary teaching opportunities. The faculty and staff have been truly helpful, with special thanks to Sandy Formica and Carol Buuck, who manage to work wonders on a daily basis.

TABLE OF CONTENTS

Page

LIST OF TABLES vi

LIST OF FIGURES viii

ABBREVIATIONS xiii

ABSTRACT xiv

1 Introduction 1

2 Case Studies 4
2.1 BNL ^{32}Si 4
2.1.1 Investigation into Possible Systematic Influences 7
2.1.2 Analysis of BNL ^{32}Si 9
2.2 PTB ^{226}Ra 12
2.2.1 Investigation into Possible Systematic Influences 13
2.2.2 Analysis of PTB ^{226}Ra 15
2.2.3 Comparison with BNL data 16
2.3 Purdue ^{54}Mn December 2006 19
2.3.1 Investigation into Possible Systematic Influences 25
2.4 Purdue ^{54}Mn Experiment 26

3 Solar Activity 30
3.1 Solar Neutrino Production 32
3.2 Flares and Coronal Mass Ejections 33
3.2.1 Classification of Flares 35
3.3 Effects of Solar Disturbances 36
3.4 Current Methods of Observation 39
3.5 Solar Indices 42
3.5.1 10.7 cm Solar Flux 43
3.5.2 Ap Index & K Value 43
3.5.3 Hard/Soft (Short/Long) X-rays 45
3.5.4 NOAA Solar Activity Indices 46

4 Detection Algorithms 51
4.1 Correlation Coefficient 51
4.2 Signal Detection Algorithms 52
4.2.1 Two-Sided Cumulative Sum 53
4.2.2 Geometric Moving Average 54

Page

4.2.3 Slope Test . . . 55
4.2.4 Runs Test . . . 56
4.2.5 F-Probability Test . . . 57
4.3 Spectral Analysis . . . 60
4.3.1 Lomb-Scargle Procedure . . . 61

5 CHANGEMASTER Algorithms . . . 66

6 Correlation Analysis . . . 75
6.1 Correlation to Solar Activity . . . 75
6.1.1 Computational Checks . . . 79
6.1.2 Negative Findings . . . 84

7 Discussion . . . 88
7.1 Multiple Decay Sites . . . 88
7.2 Conclusions & Remarks . . . 92

A Isotope Decay Schematic . . . 96
A.1 ^{32}Si via β^- decay . . . 96
A.2 ^{226}Ra via alpha decay . . . 96
A.3 ^{54}Mn via K-capture . . . 98

B Perturbation of β decay rates . . . 99
B.1 General Theoretical Framework . . . 100

LIST OF REFERENCES . . . 107

VITA . . . 112

LIST OF TABLES

Table Page

1.1 Experiments exhibiting significant decay rate fluctuations. These span a variety of different isotopes, decay processes and detectors reducing the probability of observed frequencies being a product of systemic influences. [5] 3

2.1 BNL parameters used to monitor systematic effects on detector readings. [3] 9

3.1 Principal reactions of the solar p–p chain. The p–p chain is responsible for 98.2% of energy generated from the $4^1H \longrightarrow^4 He+2e^+ +2\nu_e$ nuclear fusion reaction in the Sun. The three terminators of the p–p chain (Reactions # 4, 7 & 9), including various permutations of the C-N cycles, all generate the same total energy— 25.7 MeV. [40] 33

3.2 Solar flare classification schemes. 36

3.3 Highly energetic solar flares in history. Flare strengths are classified according to the x-ray flare scale (see Table 3.2). Included is a brief description of damage caused to communication and power services. 38

3.4 Ap index and K value relative strengths. Courtesy SWPC, NOAA. 44

5.1 Optimized *Changemaster* test parameters for 2010. The parameters for each test are adjusted to provide the optimal quality control schemes (a.k.a detection algorithms) to identify changes in the incoming signal. See text for details. 69

6.1 Four solar indices issued by NOAA which are direct measures of flare strength during solar eruptions. These thresholds filter out small scale storms, focusing on flare strengths of M-class and higher. 76

6.2 Fraction of Solar events preceded by a decay flag within 48 hours (SPD). Results are obtained from comparison of distributions from 2010-2011. The ANY-ALL entry indicates an overall 49.2% of the 413 strongest flare alerts issued were preceded by a decay flag identifying variations in the ^{54}Mn decay rate. 78

6.3 Fraction of decay flags followed by a solar index warning within 48 hours (DFS). Results are obtained from comparison of distributions taken from 2010-2011. The ANY-ALL entry shows that 37.2% of the 239 decay flags identified by *Changemaster* were indeed followed by NOAA flare alerts. 79

Table Page

6.4 Expected fractions of coincidence between decay flags and solar events assuming no correlation between them. The expected fraction of solar events randomly preceded by decay flags is 34.1%. The fraction of flags randomly followed by an alert within 48 hours is 28.1%. These are both lower than the actual SPD and DFS values which are 49.2% and 37.2% respectively. 80

LIST OF FIGURES

Figure Page

2.1 Ratio of ^{32}Si /^{36}Cl counts. Comparison against an exponential fit shows $T_{\frac{1}{2}} = 171.6(3.3)$ yr with a standard deviation of 3.2 yr. [3] 6

2.2 Points from Figure 2.1 de-trended for decay with half-life of 172 yr and normalised to 1 for the average of all points. Error bars indicate true statistical uncertainties. The curve gives an amplitude of 3.4 standard deviations. [3] 7

2.3 Plot of ^{32}Si /^{36}Cl ratio and inverse-square of Earth-Sun distance ($1/R^2$) against a coincident time interval spanning years 1982 - 1986. 10

2.4 Plot of 5 point rolling average of ^{32}Si /^{36}Cl ratio and inverse-square of Earth-Sun distance ($1/R^2$) against a coincident time interval from 1982 - 1986. 11

2.5 Residuals of ^{226}Ra . Points are residual percentages of average measurements of ^{226}Ra recorded against an exponential fit used for the decay function. The vertical lines indicate the position of January 1 within a 10 year interval. [4] 13

2.6 Plot of normalised count rate for the PTB ^{226}Ra against inverse-square distance between the Earth and Sun ($1/R^2$) spanning a interval 1984 - 1998. The correlation coefficient between the two data sets for N = 1968 data points is $\rho = 0.625$. This corresponds to a probability $P(\rho) = 9.29 \times 10^{-214}$ for the two sets being uncorrelated. 16

2.7 Correlation between raw decay rates of ^{32}Si /^{36}Cl recorded at BNL and ^{226}Ra measured at PTB . The correlation coefficient between the BNL and PTB data is $\rho = 0.66$ for N = 39 data points. This coefficient translates to a probability of 6×10^{-6} that such a coefficient value could arise from two uncorrelated data sets. Superimposed is the inverse Earth-Sun distance ($1/R^2$) for this coincident period. [10] 17

2.8 Solar region 930 erupts in a class X3 solar flare. Image captured at 2006/12/13 7:01 UT. Courtesy of Hinode Science Data Center Europe. 21

2.9 5 minute solar x-ray flux reported by GOES SEM for Dec 13-15, 2006. The sharp rise in long and short x-ray fluxes on Dec 13, 2006 correspond with the eruption of an X3 flare. Data courtesy of NOAA. 21

Figure Page

2.10 Solar particle flux reported by GOES SEM for Dec 13-15, 2006. This plot was generated by the NGDC division at NOAA. 22

2.11 Normalised ^{54}Mn counts during Dec 2006 overlayed with GOES-11 integral x-ray flux data. The ^{54}Mn data are 4 h count rates normalised to the expected rate, with error bars representing the fractional statistical uncertainty $\frac{1}{\sqrt{N}} \sim 2 \times 10^{-4}$. [14] 23

2.12 Earth-face view of the Sun for Dec 6 and 13, 2006 at 05:00 UT depicting solar positioning for region 930. Solar events occurring towards the western limb of the Sun are most likely to be Earth-ward oriented. The X9 flare on Dec 5 was not Earth-directed and not accompanied by a significant dip in ^{54}Mn count rate. By Dec 13 region 930 had rotated toward the western solar limb and any solar activity from it is more likely to be Earth directed. Solar location of active regions are provided by SWPC division at NOAA. 24

2.13 Logarithmic plot of ^{54}Mn decay data during December 2008. A region of anomalous behaviour in the measured data on Dec 16 is coincident in time with CME activity occurring on Dec 16 at 09:30 UT. 27

2.14 Coronal Mass ejection erupts over the solar eastern limb on Dec 16 2008 at 09:30 UT. Courtesy SOHO (ESA , NASA). 27

2.15 ^{54}Mn normalised net cpd plotted against inverse-square Earth-Sun distance ($1/R^2$). Data covers the period from November 13, 2008 to March 1, 2013. The correlation coefficient determined is $\rho = 0.4986$. The probability that this coefficient value could arise from two uncorrelated data sets is 8.436×10^{-89}. 28

3.1 Schematic of evolution of flare intensities at various wavelengths. [42] . 35

3.2 Carrington flare on September 1, 1859. Pictured is an illustration by Carrington of the solar region he observed during the flare eruption. Locations A and B indicate areas of initial positions of the intensely bright event, which drift to C and D over a period of 5 minutes. [43] 39

3.3 Detailed view of full-disk magnetogram image of the Sun on 27 May 1978. Individual bipolar active regions are outlined with dashed curves. White and dark regions correspond to areas of positive and negative polarity respectively. [45] 41

3.4 Stackplot formed from strips of synoptic maps for latitudes N10-N40 over Carrington rotations 1655-1681 (1977-1979). The column is created from strips taken from FLUX maps. Numerals on the right specify month and day on which each Carrington rotation begins. Extended periods without observations are blacked-out. [45] 42

Figure Page

3.5 A plot of 5 minute averaged solar x-ray flux in the long (1 - 8 Å) and short (0.5 - 4.0 Å) x-ray passbands. Courtesy SWPC, NOAA. 46

3.6 Sample list of SWPC/NOAA generated solar events for November 2, 2013. Detailed information on the event type including time of occurrence, observing facility, solar location and active region number are reported. Courtesy SWPC, NOAA. 50

4.1 Periodic signal sampled at a rate of 1 month^{-1}. The shortest period that can be resolved from this sampling rate is given by the Nyquist limit and is a signal with a period of 2 months. 64

5.1 Natural logarithm of ^{54}Mn data during May 2010. Expected decay behaviour (blued dashed curve) and predicted count rate produced using the F-Probability test (red curve) are also plotted. 67

5.2 Multiplicity and Variety flag outputs for August-October 2011. Normalised ^{54}Mn data are processed by the CUSUM2, GMA, RUNS, Tslope and Dslope tests, generating triggers during periods of fluctuations in decay rate. The resulting hits are aggregated and filtered to produce decay flags. Thresholds in red indicate that 5 or more hits are required to produce a MULT flag, and 2 or more distinct hit types will generate a VRTY flag. Note the coincidence in times between the MULT and VRTY flags, suggesting the occurrence of solar events. 71

5.3 Flow of decay data through *Changemaster* . The program analyses normalised decay data for anomalies in the incoming signal. Using a variety of signal detection algorithms and cut-off thresholds, aggregated decay flags are listed in the text file *Masterflaglist*. 72

5.4 Normalised ^{54}Mn hourly count rate recorded from August - October 2011. Superimposed below the horizontal axis in black are the hits triggered by each statistical test. In color, above the horizontal axis, are positions of aggregated decay flags VRTY, MULT, AREA, ERFC indicating areas of statistically relevant anomalous activity in the signal. 74

6.1 Solar Cycle 24 Sunspot number progression. The 11-year solar cycle can be clearly seen with a minimum in observed Sunspots occurring during 2009. The vertical lines denote January 1 of the indicated year. Courtesy SWPC, NOAA. 75

Figure Page

6.2 Distribution of Purdue ^{54}Mn decay flags and solar events from January 3, 2010 through December 30, 2011. Decay flags are listed in red from top to bottom: VRTY , MULT , AREA , ERFC . The red stars indicate regions where two or more decay flags overlap. In blue from bottom to top are the solar indices: XRA, RSP , RBR , FLA . The blue diamonds indicate regions where more than one type of index is issued. We note the presence of regions where there is an absence of both solar event alerts as well as decay flags. 77

6.3 Results from 10,000 shuffle tests for the DFS fraction. Randomized mean and standard deviation are found to be 0.282 and 0.0324 respectively. The actual results are thus statistically more significant than the randomized results by 2.79σ. 81

6.4 Results from 10,000 shuffle tests for the SPD fraction. Randomized mean and standard deviation are found to be 0.422 and 0.0773 respectively. The actual results are thus statistically more significant than the randomized results by 0.91σ. 81

6.5 Results of the SPD pac-T test for ^{54}Mn data from January 2010 to December 2011. For a cyclic 6 hour time shift in data, the average SPD value is 35.2% compared to 49.2% for the actual measured data. Since 96.9% of the cyclically permuted SPD correlations are smaller than those arising from the experimental data, the results of the pac-T test are significant at the 1.8 σ level. 82

6.6 Results of the DFS pac-T test for ^{54}Mn from January 2010 to December 2011. Data are cyclically permuted in 6 hour increments. The average DFS value obtained from time shifted data is 28.1% compared to 37.2% from actual experimental data. The results of the pac-T test are significant to the 2.3 σ level since 98.4% of the permuted DFS correlations are smaller than the actual data. 83

6.7 ^{54}Mn data analysed over March 2012. NOAA issued an alert for an X5.4 flare on 7 March 2012. The associated sunspot remained active until March 13 with the eruption of an M-class flare. During March 6-13 we find a grouping of decay flags coincident in time with the heightened solar activity. 85

6.8 Distribution of Solar events (blue) and ^{54}Mn decay flags (red) for August 2011. Although the decay data fail to show significant perturbations on August 9$^{\text{th}}$ following the X6.9 flare, several decay flags are issued on August 3-5 in conjunction with several M class flares originating from the same Sunspot 11263 a few days earlier, as well as an M9.3 flare from the neighboring spot 11261. 86

Figure Page

7.1 Simulated decay data for 1 site. Data describe a decaying exponential over 2 years. The green dashed lines identify regions of heightened activity, introduced at a frequency of 12 yr^{-1}, along with a spread of random noise. 13% of flags occur in a 48 hour period beginning at the start of each peak. The false positive rate is considerably high at 87%. 90

7.2 Averaged simulated decay data, with identical periods of heightened activity, from 10 sites over 2 years. The aggregated decay flags from a 10 site comparison clearly picks out the monthly spike generated in each of the simulated data sets. After the filtering criterion is applied, 63% of the surviving flags fall within a 48 hour period beginning at the start of each peak. 91

7.3 Comparison of all (non-zero) NOAA indices that were preceded by any type of decay flag within a 48 hour window. These indices were compared to ^{54}Mn decay data over the 2 year period from January 2010 to December 2011. 95

A.1 Beta Decay of ^{32}Si . ^{32}Si decays by β^- to ^{32}P which then decays 100% by beta emission to the ground state of ^{32}Si 96

A.2 ^{226}Ra decay chain. The decays of interest are noted with α decays directed to the right and β^- decays proceed leftwards. The concentration of daughter production are almost entirely in equilibrium with the parent ^{226}Ra 97

A.3 Beta Decay of ^{54}Mn . ^{54}Mn decays by K-capture to ^{54}Cr emitting an electron neutrino in the process. 98

B.1 Feynman diagram describing neutron β^- decay. A neutron spontaneously decays via weak interaction into a proton and electron, emitting an electron antineutrino. 101

B.2 Feynman diagram describing modified β^- decay. There is an additional proposed interaction between the emitted antineutrino by neutron decay and a solar neutrino ν_s. [62] 102

B.3 The Kurie plot for ^{3}H decay, demonstrating how a static, spatially constant and spin-dependent potential V produces a Kurie function which mimics the experimentally observed anomalous end-point behaviour. The red straight-dashed line is the Kurie function for $V^2 = 0$, $m_\nu^2 = 0$, and intersects the horizontal axis at E = $E_o \sim 529$ keV. The blue dotted-dashed curve is the Kurie function corresponding to Eq. (B.1.3) for $m_\nu^2 = +\ 130$ eV^2, while the purple dashed line is the Kurie function for Eq. (B.1.14) with $m_\nu^2 = -130$ eV^2. The solid line is the Kurie function for Eq. (B.1.17) with $V^2 = 65$ eV^2. [62] 106

ABBREVIATIONS

BNL	Brookhaven National Laboratory
CME	Coronal Mass Ejection
DFS	Decay flag Followed by Solar Event
ESA	European Space Agency
GOES	Geostationary Operational Environmental Satellites
HFIR	High Flux Isotope Reactor
NGDC	National Geophysical Data Center
NNDC	National Nuclear Data Center
NOAA	National Oceanic and Atmospheric Administration
NSO	National Solar Observatory
ORNL	Oak Ridgle National Laboratory
PTB	Physikalisch-Technische Bundesanstalt
SOHO	Solar and Heliospheric Observatory
SPD	Solar event Preceded by Decay flag
SWPC	Space Weather Prediction Center

ABSTRACT

Mohsinally, Tasneem M. Ph.D., Purdue University, May 2015. An Investigation into the Phenomenological Relation between Solar Activity and Nuclear Beta-Decay Rates. Major Professor: Ephraim Fischbach.

We investigate experimental evidence for time-varying nuclear decay rates, in contrast to the widely-accepted view that nuclear decaying isotopes disintegrate at a constant rate unaffected by external conditions. We study several past cases of radioactive isotopes exhibiting annual periodicities in their decay rates, presumably related to the annual variation in Earth-Sun distance. Following recent indications of shorter-lived anomalies in ^{54}Mn decay rates concomitant with an X-class flare in 2006, we attempt to design and develop a series of unique signal detection algorithms to identify regions of anomalous activity in a nuclear decay signal. With stringent threshold cut-offs and filtering processes, these regions are isolated as exhibiting statistically significant deviations from an expected exponential decay model. The isolated decay flags are compared to daily distributions of multiple solar indices associated with heightened flare activity. We present the findings from a 2 year period of data collection on ^{54}Mn . Of the several computational checks performed to verify the validity of these results, none were able to produce values as good as those generated from the actual decay measurements.

1. Introduction

It is widely accepted that the spontaneous radioactive decay of unstable isotopes occurs at a constant rate specific to the particular isotope. This decay is described by the familiar exponential decay law, see below, where the decay constant λ describes the rate at which a nuclide disintegrates. The process of radioactive decay was extensively investigated in the early 20th century, partly to see if λ was truly a constant of nature unaffected by its external environment. In 1930, results of investigations carried out by several groups [1, 2] led Rutherford, Chadwick and Ellis to conclude 'the rate of transformation of an element through radioactive decay was indeed found to be constant under all conditions'.[1]

To begin, we provide a brief overview of the theory behind exponential radioactive decay. Underlying the decay law is the assumption that the decay of every nucleus occurs randomly in time, and independently of any other. Consider an isotope sample containing a population of $N(t)$ atoms at time t. The atoms randomly decay at the isotope's characteristic decay rate, λ, and at a time t its activity is given by

$$-\dot{N}(t) \equiv -\frac{dN(t)}{dt} = \lambda N(t). \tag{1.1}$$

Equation (1.1) leads to the familiar exponential radioactive decay law:

$$N(t) = N_o e^{-\lambda t}, \tag{1.2}$$

where $N_o \equiv N(t = 0)$. The amount of time required for a sample of N atoms to decay to half its initial population is denoted by the half-life $T_{\frac{1}{2}}$. The half-life is related to

[1]This is true except for cases of decays proceeding by electron capture. Here, the decay rate can be modified to a minimal degree by subjecting the nucleus to extreme electromagnetic fields or pressure. In such cases the rate of decay is influenced by the overlap of the electron's wave function and that of the nucleus.

the decay constant λ by $T_{\frac{1}{2}} = \frac{ln(2)}{\lambda}$ and should also be a constant value. Taking the natural logarithm, $\ln(\dot{N}(t))$ versus time generates a linear relationship where the decay parameter[2] is obtained from the slope of the line. Following this theoretical framework, one would expect experimental data to follow a random spread about an exponential fit predicted by theory with no apparent signal embedded within the residuals. However, analysis of previous data sets, BNL [3] and PTB [4], small fluctuations of the order 0.1% were noted in the decay rates. Although these fluctuations had relatively little effect upon experiments running for significantly longer than the period of oscillation, it is of interest to investigate further, either to support or prove false, the possibility that the rate of nuclear decay may be influenced by external sources.

While studying various isotopic measurements from other experiments, used for determining half-life values, the presence of inherent periodicities embedded within the raw data collected were noticed by several groups. Table 1.1 lists the annual variations found in a number of different isotopes noted by our group as well as others. Also included are the different detector set-ups which vary between experiment and isotope, reducing the possibility of the observed periodicities arising from systematic influences. The purpose of this investigation is to explore possible relationships these fluctuations may have with several other known phenomena exhibiting similar periodicities. These include a possible connection, up to some phase, to the Earth-Sun distance, or some apparent association to activity occurring on the solar surface. The characteristics of these fluctuations are complex as we search not only for physical periodicities occurring over a long time-scale, but also for shorter lived anomalies that can indicate regions of interest in the measured nuclear decay data.

[2]In order to avoid the oxy-moronic phrase "time-dependent decay constant," we will henceforth refer to λ as the decay parameter.

Table 1.1: Experiments exhibiting significant decay rate fluctuations. These span a variety of different isotopes, decay processes and detectors reducing the probability of observed frequencies being a product of systemic influences. [5]

Isotope(Decay)	Detector	Measured	Observed Frequency	Refs
^{3}H (β^-)	Photodiodes	β^-	1 yr^{-1}	[6]
^{3}H (β^-)	Liquid Scintillator	β^-	1 d^{-1},12.1 yr^{-1}, 1 yr^{-1}	[7]
^{3}H (β^-)	Solid State (Si)	β^-	2 yr^{-1}	[8]
^{22}Na/^{44}Ti (β^+, κ)	Solid State (Ge)	γ	1 yr^{-1}	[9]
^{36}Cl (β^-)	Prop. Counter	β^-	1 yr^{-1}, 11.7 yr^{-1}, 2.1 yr^{-1}	[10–12]
^{36}Cl (β^-)	Geiger-Muller	β^-	1 yr^{-1}	[13]
^{54}Mn (κ)	Scintillation	γ	Short term decrease	[14]
^{54}Mn (κ)	Scintillation	γ	1 yr^{-1}	[15]
^{54}Mn (β^-)	Scintillation	γ	1 yr^{-1}	[16]
^{60}Co (β^-)	Geiger-Muller	β^- ,γ	1 yr^{-1}	[17, 18]
^{60}Co (β^-)	Scintillation	γ	1 d^{-1}, 12.1 yr^{-1}	[19]
^{85}Kr (β^-)	Ion Chamber	γ	1 yr^{-1}	[20]
^{90}Sr/^{90}Y (β^-)	Geiger-Muller	β^-	1 yr^{-1}, 11.7 yr^{-1}	[17, 18, 21]
^{108m}Ag (κ)	Ion Chamber	γ	1 yr^{-1}	[20]
^{133}Ba (β^-)	Ion Chamber	γ	1 yr^{-1}	[22]
^{137}Cs (β^-)	Scintillation	γ	1 d^{-1}, 12.1 yr^{-1}	[19]
^{152}Eu (β^- ,κ)	Solid State (Ge)	γ	1 yr^{-1}	[4]
^{152}Eu (β^- ,κ)	Ion Chamber	γ	1 yr^{-1}	[20]
^{154}Eu (β^- ,κ)	Ion Chamber	γ	1 yr^{-1}	[20]
^{222}Rn (α,β^-)	Scintillation	γ	1 yr^{-1}, 2.11 yr^{-1}, 11.7 yr^{-1}	[23]
^{226}Ra (α,β^-)	Ion Chamber	γ	1 yr^{-1}, 2.1 yr^{-1}, 11.7 yr^{-1}	[10, 12, 24]
^{239}Pu (β^-)	Solid State	α	1 d^{-1}, 1 yr^{-1}, 13.5 yr^{-1}	[7]

2. Case Studies

In this section we outline several experiments, both from independent sources as well as those carried out by our collaboration, where the data collected show time-dependent fluctuations for certain isotopes outside what would be expected from statistical fluctuations. Further, we outline an analysis of the detection systems in order to demonstrate that these fluctuations are likely not due to equipment or environment but rather a property resulting from the intrinsic behaviour of the decay itself.

2.1 BNL ^{32}Si

An experiment conducted at Brookhaven National Laboratory (BNL) by Alburger et al. during 1982 to 1986 [3] was among the initial studies which brought attention to such unexplained anomalies in recorded nuclear decay data. The group at BNL monitored the count rate from a sample of ^{32}Si during this period in an attempt to determine its half-life. This particular radioisotope of silicon decays via β^- emission to the daughter isotope ^{32}P, emitting an electron anti-neutrino and a β^- particle in the process. Due to the considerable attenuation of low energy (225(19) keV) β^-decay by a copper foil surrounding the sample in their detector set-up, the decay of the relatively higher-energy daughter nucleus ^{32}P ($T_{\frac{1}{2}} = 14.28$ d)[1], which decays 100% by β^- to the ground state of ^{32}S, was measured. See Appendix A.1 for a decay schematic. In addition, measurements of ^{32}Si [2] and ^{32}P were recorded and the intensities of each component distributions were equal to within measuring uncertainties of a few percent. Their known end-point energies were also consistent with known Q_{β^-} values for

[1] Half-life values and energies noted here are as published by Alburger et al. [3]

[2] The ^{32}Si component was observed in the spectrum of the same material in a liquid scintillation detector

^{32}Si ($Q_{\beta^-} = 225$ keV) and ^{32}P ($Q_{\beta^-} = 1710$ keV). The result of their analysis determined the half-life of ^{32}Si to be $T_{\frac{1}{2}} = 172(4)$ yr. During operation, the Brookhaven team used ^{36}Cl as a control due to its long half life of 301,000 yr. ^{36}Cl decays to the ground state of ^{36}Ar ($Q_{\beta^-} = 709.6$ keV) with a branching ratio of 98.1% β^- decay, and to the ground state of ^{36}S ($Q_{\varepsilon} = 1144$ keV) 1.9% through electron capture.

Comparison counts were taken from the ^{36}Cl source using a gas-flow proportional counter and the two samples were interchanged via a precision apparatus. Runs consisted of 30 minutes of counting for each source with a 20 s delay while the detector was exchanged between samples, for a total of 10 hr on each isotope each day. This was carried out successively for 4 days each month and the results were averaged to give one datum of ^{32}Si /^{36}Cl ratio.[3]

In addition to the ^{32}Si /^{36}Cl ratio, single measurements of ^{32}Si and ^{36}Cl were also recorded, and the error in the ratio for a typical 4 day run calculated from the statistical uncertainties for the ^{32}Si total counts (0.017%) and ^{36}Cl total counts (0.014%) was found to be 0.022%. Determining the ratio of the two samples should accommodate for systematic errors affecting both samples, and therefore systematics should not be a significant contributing factor to the fluctuations seen in the ratio data.

Figure 2.1 depicts the ratio of ^{32}Si /^{36}Cl counts measured over a period of 48 months with error bars arbitrarily set by the authors at 3 times the actual statistical uncertainties. Results from approximately four years of data collection indicated the presence of an annual periodic effect embedded in the recorded measurements. Since the authors were unable to explain these fluctuations from a smooth exponential decay curve they tried to average out any annual periodicity by analysing data in multiples of 12 months, producing a resultant half-life of $T_{\frac{1}{2}} = 172(4)$ yr. While not relevant to possible time-variations of the decay constant, it is of passing interest to note highly discrepant values of the ^{32}Si half-life from Atomic Mass Spectroscopic (AMS) measurements. Utilizing this technique, Elmore et al. [25] obtained a ^{32}Si half-life of

[3]Notes from the BNL group indicate that though the experiment was run continuously, data were recorded at intervals that were not always uniform, ranging from 10 hr to 53 d with a median interval of 1 day.

108(18) yr, while an AMS experiment by Kutschera et al. [26] performed simultaneously at Argonne National Laboratory reported $T_{\frac{1}{2}} = 101(18)$ yr. The systematics of the AMS method are very different from those in a counting experiment, and require, amongst other things, knowledge of the absolute efficiency in counting all decays of the sample nuclei. More recently, Nijampurkar et al. published a half-life $T_{\frac{1}{2}} = 178(10)$ yr by studying the geochemical constituents of sediment cores [27]. Among these varying results, the National Nuclear Data Center (NNDC), considered to be the international standard for decay activity listings, currently lists the half-life of ^{32}Si to be $T_{\frac{1}{2}} = 153(19)$ yr— a 12% difference from the value published by Alburger et al.

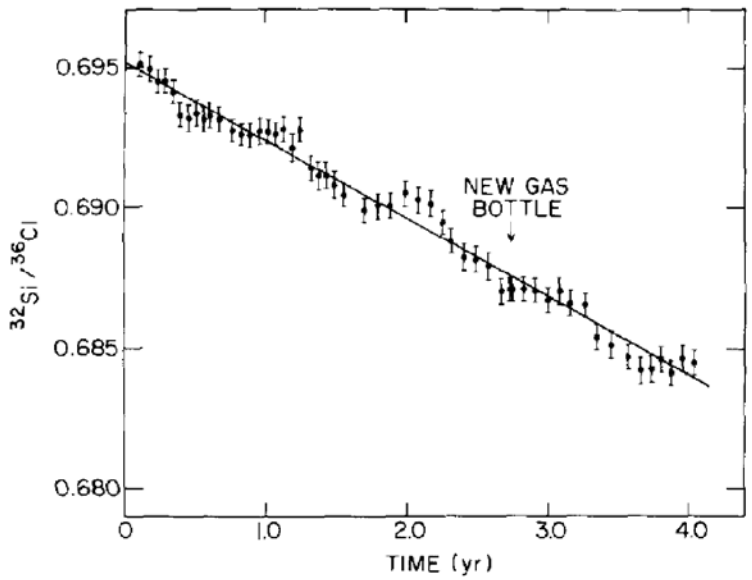

Figure 2.1.: Ratio of ^{32}Si /^{36}Cl counts. Comparison against an exponential fit shows $T_{\frac{1}{2}} = 171.6(3.3)$ yr with a standard deviation of 3.2 yr. [3]

Alburger et al. de-trended the ^{32}Si /^{36}Cl for decay using $T_{\frac{1}{2}} = 172$ yr, renormalising the results for each year. Figure 2.2 shows the 4 yearly-segmented sections overlayed against a 12-month sinusoidal curve. This curve displays an amplitude of 3.4 standard deviations, with maxima and minima falling on February 9 and August 6 respectively. Even after considering the possible influence of temperature and hu-

midity variations having an effect on the indoor climate (see Sec. 2.1.1), Alburger et al. conclude that the 'systematic periodic variations are present and cannot be fully accounted for by our tests or estimates'.[4]

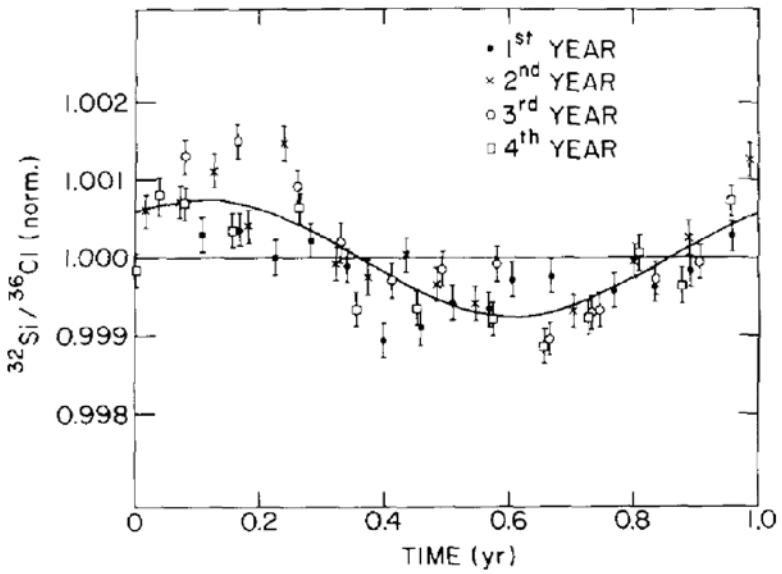

Figure 2.2.: Points from Figure 2.1 de-trended for decay with half-life of 172 yr and normalised to 1 for the average of all points. Error bars indicate true statistical uncertainties. The curve gives an amplitude of 3.4 standard deviations. [3]

2.1.1 Investigation into Possible Systematic Influences

Alburger et al. tested their experimental apparatus to see if any single factor could produce a convincing explanation for the fluctuations they saw. The various factors that can affect counting rate measurement include the counter voltage, the gas-flow rate in the counter, box pressure, source positioning, discriminator and amplifier gain, and relative temperature and humidity of the system. Following their investigation, we list the results published by Alburger et al., and Table 2.1 summarises the results of their analysis [3].

[4]Alburger et al. also note the long-term stability of their counting system from the ^{36}Cl points which fluctuated about a constant value.

The BNL team ruled out the detector positioning apparatus as a possible factor. They cite the 'high quality of mechanical construction' and micro-meter source mounts as reasons to presume accurate source positioning.

The counter voltage was set at 2150 V. It can be inferred that in order to produce fluctuations in ^{32}Si /^{36}Cl ratio equal to one standard deviation (0.022%) would require a 25 V change in applied voltage. However, the power supply specifications allowed less than 0.5 V shift in long term drift and resolvability at 2150 V.

Gas-flow in the counter would require the gauge reading to change by 0.01 to produce an effect to the order of one standard deviation. However, they note the gas-flow gauge readings were accurate to within 0.002 units on their gauge.

An optimum operating value for the box pressure was set at 29.38″ Hg. The box pressure would have to vary by 0.15″ Hg to produce any sizable effects. During run-time, the pressure was maintained to within 0.03″ Hg.

The temperature and humidity were the only parameters observed to have a possible effect on the ^{32}Si /^{36}Cl ratio within one standard deviation. Noting that temperature and relative humidity can affect air density which would produce pressure changes, they calculate that a 2.0°F change in temperature, or variation in relative humidity from 30% - 80%, would be needed to produce a one standard deviation change in ^{32}Si /^{36}Cl measurements. Data for these two parameters were recorded only for the final five months of the experiment. During that time, the average temperature was measured to be 72.4°F - 74.7°F and the average humidity varied between 35% - 76%.

In addition to systematic effects, background radiation was also monitored. The background count rate measured 6.6(3) counts min^{-1} before the sources were installed and 6.5(3) counts min^{-1} at the end of all runs. Average counting rates for the ^{36}Cl source and ^{32}Si -^{32}P sample were 21,500 counts min^{-1} and 14,800 counts min^{-1} respectively. The fractional change for such a small background measurement would be $\sim 10^{-4}$, making it unlikely for such effects to be caused by the background flux.[5]

[5]For the final measurement of background count rate the ^{36}Cl source remained, and the source changer was positioned on the empty ^{32}Si slot.

Table 2.1: BNL parameters used to monitor systematic effects on detector readings. [3]

Parameter	Setting	Δ ^{32}Si rate	Δ ^{32}Si /^{36}Cl rate
Counter voltage	2150 V	3.1 %/100 V	0.086 %/100 V
Counter gas flow	0.042 gauge	0.16 %/0.01 gauge	0.025 %/0.01 gauge
Box pressure	29.38″	0.1 %/0.1″	0.016 %/0.1″

2.1.2 Analysis of BNL ^{32}Si

Assuming a monotonically decreasing exponential decay form, fluctuations recorded in ^{32}Si counting rates should be within ranges predicted by statistical uncertainties and have no correlation to any external influences. During the four years this experiment was carried out the ^{32}Si counting rate was recorded using the same detector apparatus throughout and compared against a long-lived isotope ^{36}Cl , with a half-life of 301,000 yr. Since the fractional change in ^{36}Cl count rate over the experiment period was $\sim 10^{-5}$, its count rate was considered to remain stable over the lifetime of this experiment, making it an ideal control agent. This fractional difference was much smaller than the overall uncertainty calculated for ^{32}Si .

In preparation for analysis we normalise the ^{32}Si and ^{36}Cl data by dividing the measurements with an expected exponential decay trend, where the decay rate λ is the average value obtained from a best fit curve to the data set. In principle, computing the ratio should suppress any systematic effects influenced by instrumentation, should they arise. This ratio reveals the presence of an embedded signal that cannot be explained by any known effects from changes in the environment or equipment (see Sec. 2.1.1). If we are to postulate that this signal either arises from, or occurs in coincidence with, activity from the Sun, then it is reasonable to look at a function of the Earth-Sun distance R as a first initiative. Figure 2.3 compares the normalised values for ^{32}Si /^{36}Cl ratio from 1982 - 1986, for N = 293 data points, against the

inverse-square of Earth-Sun distance ($1/R^2$). Earth-Sun distance data are provided by the U.S. Naval Observatory (USNO) in astronomical units (a.u). Here the maxima and minima correspond to the perihelion and aphelion which occur during the first week of January and July respectively. The ^{32}Si count rate shows a fractional change of 3 x 10^{-3} between maxima and minima.[6]

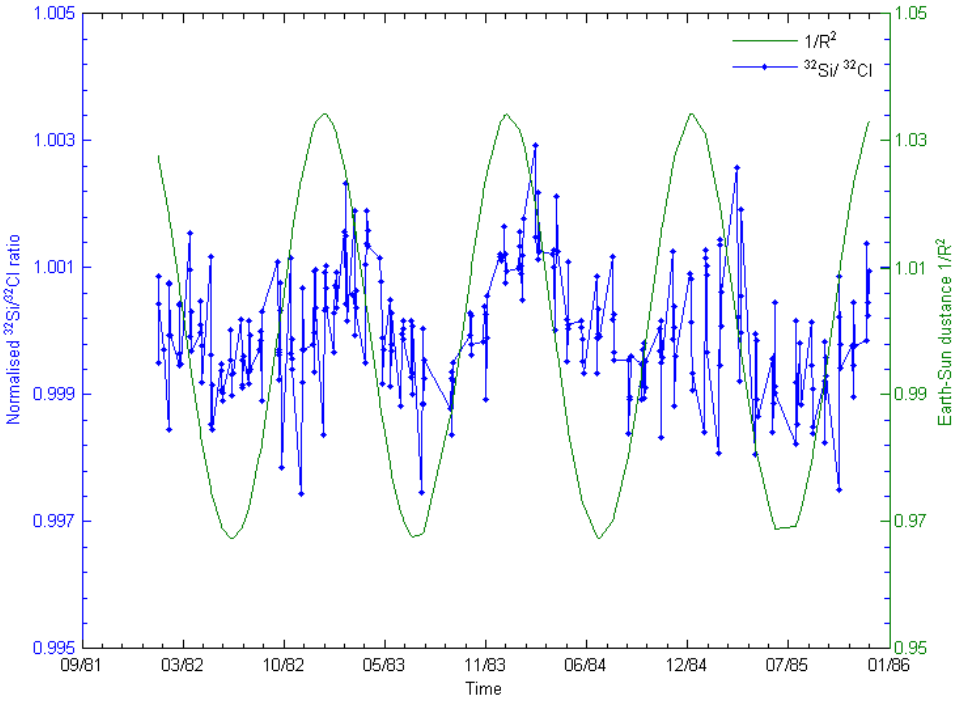

Figure 2.3.: Plot of ^{32}Si /^{36}Cl ratio and inverse-square of Earth-Sun distance ($1/R^2$) against a coincident time interval spanning years 1982 - 1986.

We perform a Pearson correlation calculation to obtain a statistically significant value for any similarity seen between BNL ^{32}Si /^{36}Cl ratio and $1/R^2$. Without accounting for a phase shift between the two arrays, the Pearson correlation coefficient calculated is $\rho = 0.407$ for the above N = 293 data points. The likelihood of ob-

[6]The *phase* of a sinusoidal signal denotes the calender day during the year when the observed count rate is a maximum.

taining such a value for the coefficient from two *uncorrelated* variables is given by Eq. (4.4) in Sec. 4.1. In this case $P_{293}(\rho) = 4.06 \text{ x } 10^{-13}$, indicating a highly unlikely probability that the two sets have no connection. Taking a 5 point rolling average of ^{32}Si /^{36}Cl ratio against $1/R^2$, Fig. 2.4, provides a clear view of the trend followed by both sets of data. Here each point is centred around the original datum.

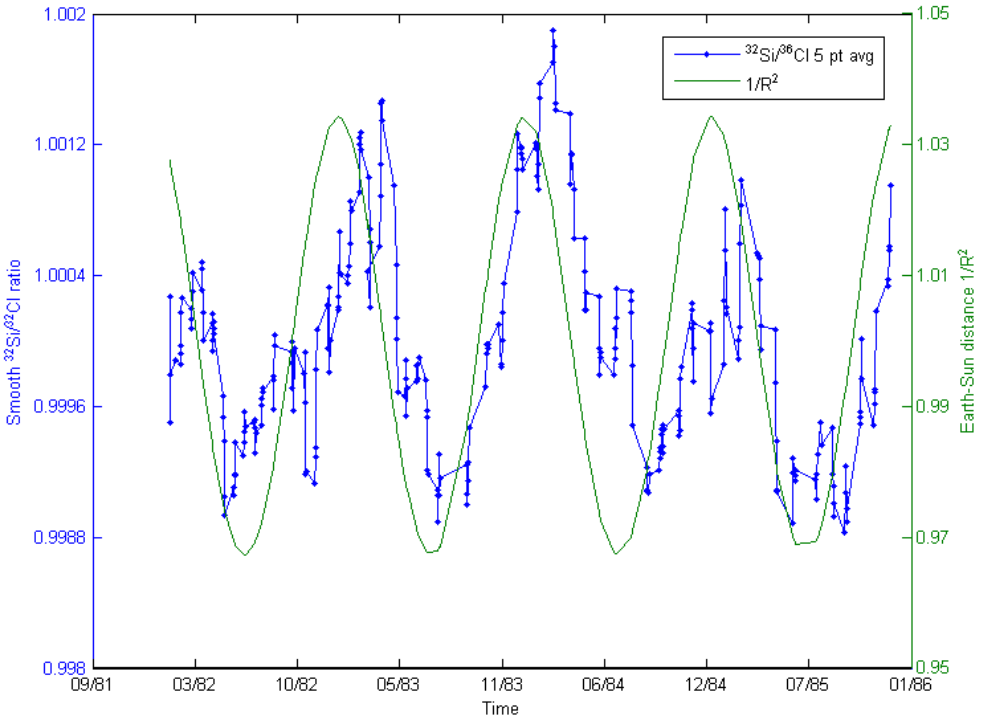

Figure 2.4.: Plot of 5 point rolling average of ^{32}Si /^{36}Cl ratio and inverse-square of Earth-Sun distance ($1/R^2$) against a coincident time interval from 1982 - 1986.

2.2 PTB ^{226}Ra

Siegert et al. conducted an investigation at the Physikalisch-Technische Bundesanstalt (PTB) located in Brunswick, Germany, during 1983 - 1998 attempting to measure the half-life of europium isotopes ^{152}Eu and ^{154}Eu using a pressurized $4\pi\gamma$ ionization chamber [4]. The control used was an isotope of radium, ^{226}Ra , with a long half-life of $T_{\frac{1}{2}} = 1600(7)$ yr [28]. Although ^{226}Ra itself decays via α-emission, several of its daughters undergo β decay within the decay chain, with almost all remaining in equilibrium with ^{226}Ra (see Appendix A.2). In each measurement cycle the reference source was measured alternately with europium isotopes and background. Due to the high intensity of the ^{226}Ra source, data were recorded in the form of ionization currents generated by the large number of gammas from the decaying isotopes.

Siegert et al. note that the raw data recorded for ^{226}Ra from the ionization chamber "show small periodic fluctuations...[which] may be fitted by a superposition of an exponential decay and a periodic function with a yearly period" [4]. Figure 2.5 illustrates the residual values for ^{226}Ra as a function of time. Here, the residuals are the remaining fluctuations obtained after their data were de-trended using $e^{\lambda t}$, where λ is the decay constant for ^{226}Ra . The points are averaged over several days, ≈ 30 individual current measurements taken over 3 days, and corrected for background. On analysis of the ^{226}Ra data alone, they observed a yearly oscillation with an amplitude of 0.15% with maxima and minima occurring near early February and early August respectively. The phase[7] seen in PTB data is shifted from perihelion (January 3) by approximately 30 days, and similarly from aphelion (near July 4) with the same delay. In addition, the authors noted an average decrease in the efficiency of their detector on the order of 0.005% per year.

[7]The *phase* of a sinusoidal signal denotes the calender day during the year when the observed count rate is a maximum.

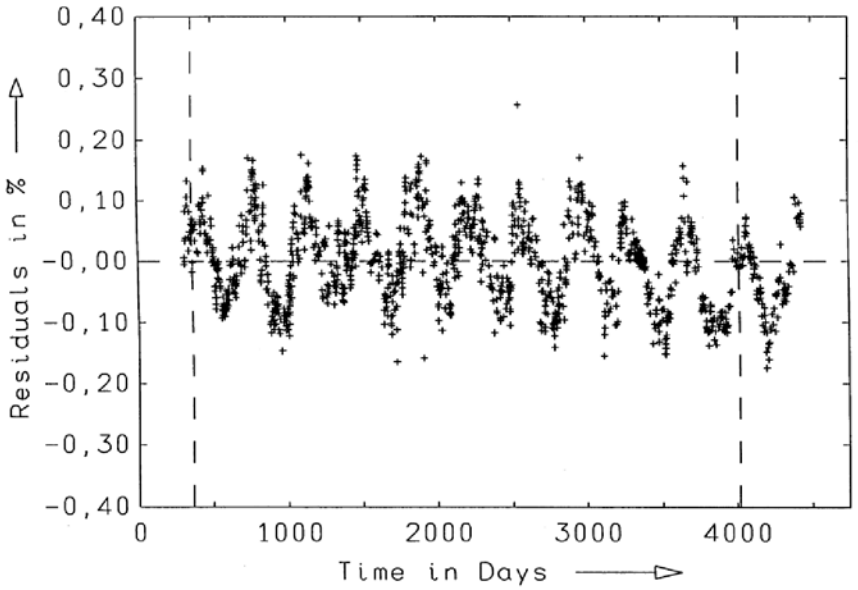

Figure 2.5.: Residuals of ^{226}Ra . Points are residual percentages of average measurements of ^{226}Ra recorded against an exponential fit used for the decay function. The vertical lines indicate the position of January 1 within a 10 year interval. [4]

2.2.1 Investigation into Possible Systematic Influences

Following an in-depth analysis conducted by Jenkins, Mundy, and Fischbach [29] we summarize the results of studying any effects or influences external or environmental conditions may have had on the detector equipment utilised at PTB .

The $4\pi\gamma$ ionization chamber used at PTB recorded the output current generated by electron-ion pairs when argon gas inside the chamber ionizes. The bias voltage was set at 500 V— this value is sufficiently high to prevent recombination of electron-ion pairs but not large enough to provide an amplified effect within the detector. Thus, the output current is based on the number of pairs created by the incident γ-radiation only. In addition, since the current is essentially independent of voltages applied within the chamber, such detectors are relatively insensitive to changes in the applied bias voltage.

Next, we consider the effect changes in room temperature will have on the detection system. The argon gas within the chamber was filled (to 20 atm) by the manufacturer, and then welded shut before being delivered to PTB — thus, the number of argon atoms inside the chamber remains constant. Since the detector was relatively well shielded from its surroundings, any changes in room temperature would result in negligible changes in chamber volume thus barely affecting gas pressure within [29]. Following from the ideal gas law, for a constant volume, the density of argon gas is independent of room temperature and only shows a dependence on the gas pressure inside. Also, argon's potential for ionization is constant over pressures from 1 - 200 bar. Hence, the ionization gas, which is proportional to the energy deposited by incident γ-radiation, finds little dependence on changes in room temperatures.

Further attention was paid to external environmental influences such as humidity, air pressure, etc. Since the detector was in a closed system, these effects proved to have little influence on the detector chamber.

Of concern is background contamination from ^{222}Rn which is known to exhibit seasonal and diurnal variations. An analysis conducted by Abbady et al. in Hanover, Germany, recorded these fluctuations in indoor concentrations of ^{222}Rn [30][8]. While these fluctuations do exist, the actual activities (15 - 90 Bq m^{-3}) are extremely small when compared to the flux from the 300 μg sample of ^{226}Ra, which would produce activity on the order of 10^7 Bq. Thus, the ^{222}Rn contamination would have a negligible effect on the count rate. Additionally, the period and phase observed in ^{222}Rn concentrations do not coincide with the ^{226}Ra data reported by Seigert et al. Any effects from other background contaminants, such as muons or natural potassium, were minimized by shielding the detector system in a 5 cm thick lead space. Particularly, atmospheric muons are produced when highly energetic cosmic radiation interact with the nuclei of atmospheric particles. The resulting pions decay into muons and their corresponding neutrinos which are known to fluctuate seasonally, up to 10% the average flux value [31]. Though it is true that we would expect the

[8]Measurements were recorded every 2 hrs daily for a period of 1 year.

muon flux to follow variations in atmospheric density and temperature, the observed average muon flux at sea level is $\sim 10^3$ counts d^{-1} cm^{-2} [32]. This value is too small to significantly affect the ^{226}Ra sample's high activity rate ($\sim 10^{11}$ counts d^{-1}). Additionally, the muon signal would be expected to produce counts over all of the detector's energy bins indiscriminately. That the decay fluctuation is seen primarily within the isotope's region of interest (ROI) energy channels supports the claim that the observed signal is not attributed to the atmospheric muon flux.

2.2.2 Analysis of PTB ^{226}Ra

As noted above, it was the discovery of an anomalous signal embedded in results published by Alburger et al., coincident with the annual modulation of the inverse square of the Earth-Sun distance, that prompted further investigation into measurements obtained from other decaying isotopes as well. Analysis of experiments with data sets that were taken continuously over a relatively long period of time led us to the Physikalisch- Technische Bundesandstalt (PTB) in Germany (see Sec. 2.2). Siegert et al. measured the decay emissions from ^{152}Eu and ^{226}Ra for a period of 15 years, overlapping with data from the BNL group for approximately 2 years. We were able to obtain the original raw data for the control isotope used by the PTB group— ^{226}Ra ($T_{\frac{1}{2}} = 1600(7)$ yr). Figure 2.5 exhibits the annual variations in ^{226}Ra data similar to those analysed in BNL 's ^{32}Si /^{36}Cl ratio. We similarly treat the PTB measurements, plotting these data against the annual variation in Earth-Sun distance, as seen in Fig. 2.6. There is a fractional change in ^{226}Ra count rate of ~ 3 x 10^{-3} between perihelion and aphelion.

Carrying out a Pearson correlation test (see Sec. 5.1) on the N = 1968 data points spanning years 1983 - 1998 plotted in Fig. 2.6 against $1/R^2$, results in a correlation coefficient $\rho = 0.625$. This translates to a probability $P(\rho) = 9.29$ x 10^{-214} for such a coefficient value arising from two uncorrelated data sets.

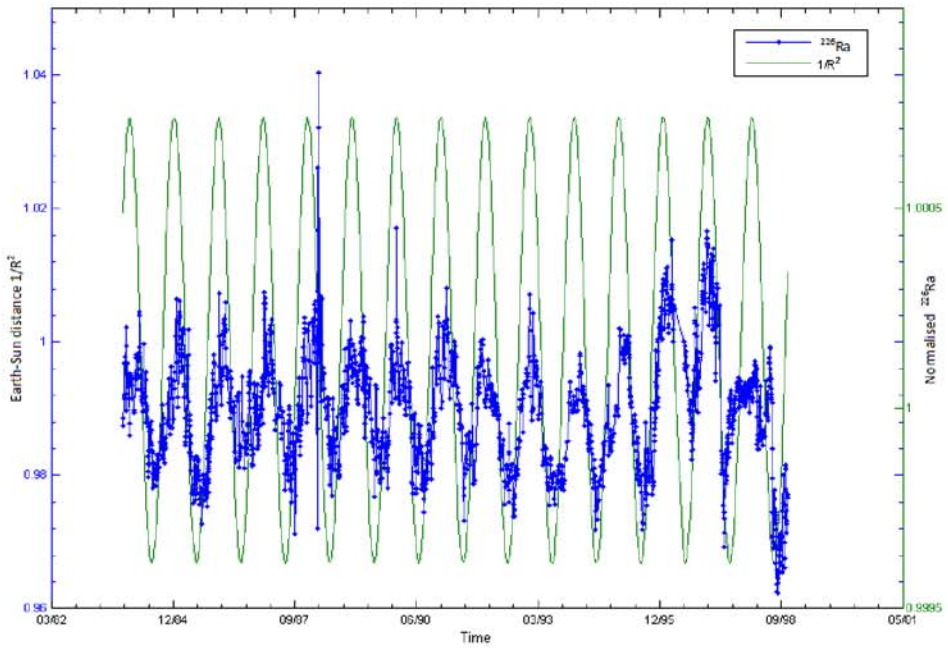

Figure 2.6.: Plot of normalised count rate for the PTB ^{226}Ra against inverse-square distance between the Earth and Sun ($1/R^2$) spanning a interval 1984 - 1998. The correlation coefficient between the two data sets for N = 1968 data points is $\rho = 0.625$. This corresponds to a probability P(ρ) = 9.29 x 10^{-214} for the two sets being uncorrelated.

2.2.3 Comparison with BNL data

Considering the period of overlap between PTB and BNL data sets from 1983 - 1985, shown in Fig. 2.7, we calculate the correlation between the two decay data sets. The raw decay rates of ^{32}Si /^{36}Cl from BNL and ^{226}Ra from PTB are averaged in common weekly bins. The resultant N = 39 data points are used to compute the Pearson correlation coefficient which is $\rho = 0.66$, corresponding to a probability P(ρ) = 6 x 10^{-6} that these data sets are uncorrelated. Such a low probability indicates that it is highly unlikely that this value of correlation could arise from two unconnected sets as a result of statistical fluctuation.

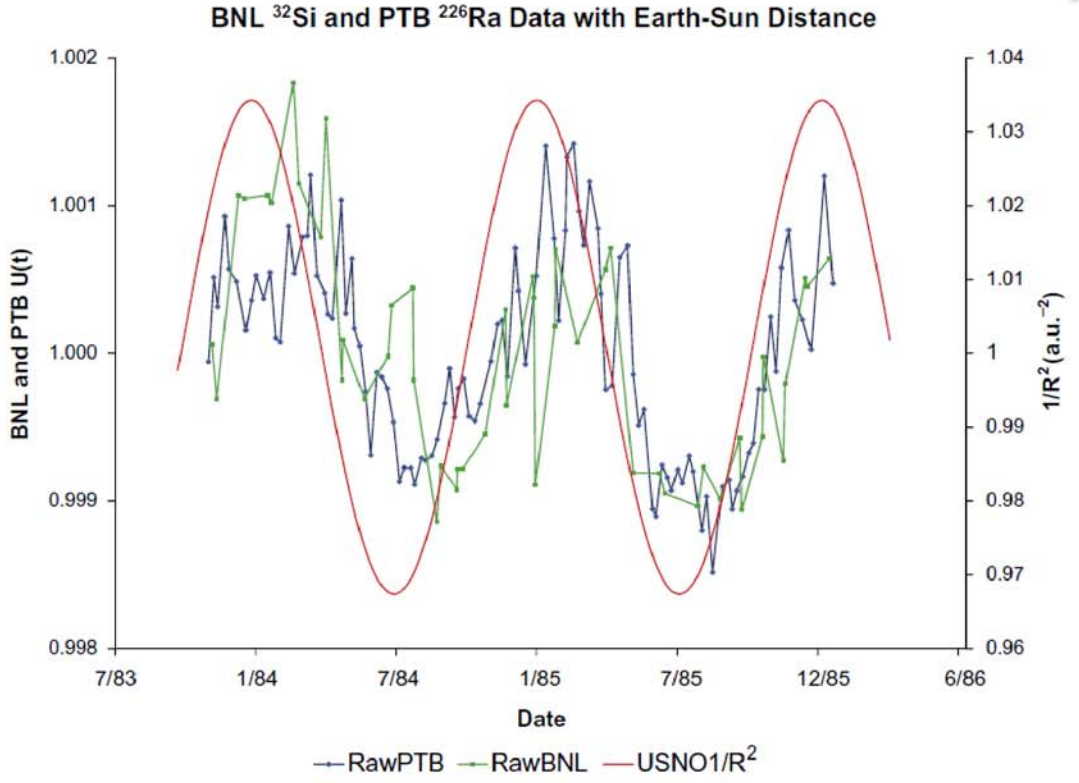

Figure 2.7.: Correlation between raw decay rates of ^{32}Si /^{36}Cl recorded at BNL and ^{226}Ra measured at PTB . The correlation coefficient between the BNL and PTB data is $\rho = 0.66$ for N = 39 data points. This coefficient translates to a probability of 6 x 10^{-6} that such a coefficient value could arise from two uncorrelated data sets. Superimposed is the inverse Earth-Sun distance ($1/R^2$) for this coincident period. [10]

One might argue that such a correlation between nuclear decay activity and Earth-Sun distance is in fact a result of an influence from seasonal variations. However, both the difference in latitudes between the locations of the BNL (*40N 51′ 59.80″*) and PTB (*52N 17″ 47.51″*) experiments, as well as their dissimilar climatic conditions, provide adequate reason to rule out the experimental set-up being influenced by seasonal environmental factors such as temperature, humidity, pressure, etc. To elucidate, Siegert et. al. [4] note the known seasonal variation in radon concentrations, suggesting that the detector apparatus could have been influenced by a seasonally de-

pendent charge distribution from ^{222}Ra decay. However, according to Wissmann [33], who conducted an investigation on the environmental radiation conditions at ground level at PTB, the low decay rate from ^{222}Ra background would produce a negligible effect. Additionally, the PTB ^{226}Ra data were corrected for any background effects.

In addition to the differing climates and latitudinal coordinates, the difference in detection systems employed by each research team provides a compelling case for ruling out suggestions that the observed fluctuations are by-products of some form of similar systematic experimental interference. As noted previously, Siegert et al. used a pressurized $4\pi\gamma$ high-pressure ionization chamber to measure ^{226}Ra count rate by recording the ionization current produced by the decay products. They also used germanium and silicon semiconductor detectors to record the count rate from a radioactive sample of ^{152}Eu. In contrast, investigators at BNL used a gas-flow proportional counter system to measure the 1710.3(6) keV emission from ^{32}P β^- decay to the ^{32}S ground state.

Another factor is the difference in decay processes exhibited between the two isotopes ^{32}Si and ^{226}Ra . While ^{32}Si has a simple chain of decay (see Appendix A.1)—β^- decay 100 % of the time to ^{32}P, which subsequently decays to ^{32}S , the decay chain for ^{226}Ra is a relatively complex decay process (see Appendix A.2). Although ^{226}Ra itself decays via the emission of an alpha particle, it has several daughters which β^- decay and quickly reach equilibrium with the initial parent ^{226}Ra concentration, as noted above. This difference in processes hints at the observed fluctuations being a result of an external influence interacting with the decaying nuclei and affecting the decay rate.

2.3 Purdue ^{54}Mn December 2006

After considering the possibility of embedded signals within radioactive decay measurements reflecting changes in the Earth-Sun distance, we discuss a more direct approach for correlating changes in isotope count rates to activity occurring in the Sun. Though the notion that radioactive decay rates could be affected by any external influence is not a widely accepted view, we find on analysing our data sets that the results in fact suggest the possibility of such a phenomenological occurrence.

Specifically, we discuss the apparent fluctuation in count rate seen in the Purdue ^{54}Mn signal coinciding with the December 13, 2006 solar flare [14]. In later sections we develop a computational package that runs a series of signal detection tests on ^{54}Mn data collected at Purdue University over several years. It is our aim to compare the times of anomalous activity in the decay measurements with several solar indices obtained from various national agencies (NASA, NOAA, NGDC) which are associated with high levels of solar activity.

During the period December 2, 2006 - January 2, 2007, the research group at Purdue University collected data on a $\sim$ 1 μCi sample of ^{54}Mn , with a half-life of 312.05(4) d[9]. ^{54}Mn decays 100% via K-capture (Q_{gs} = 1377.1(10) keV) to its daughter nucleus ^{54}Cr (see Appendix A.3). The ^{54}Mn decay is then detected by the subsequent decay of ^{54}Cr to its ground state via the emission of a 834.8 keV gamma ray. The sample was attached to a thallium doped sodium iodide detector (Bicron 2 x 2″ NaI(Tl) crystal detector (Model # 2M2/2X) connected to a photomultiplier tube (PMT) base and pre-amplifier (Ortec # 276 PMT base). The incoming pre-amplified signal was analysed using multi-channel analyser (MCA) software running on an Ortec Trump^{TM}PCI chip. Lead bricks were positioned on all sides of the detector and sample, except at the end of the PMT base to allow cables to pass through, provided shielding. Apart from this shielding, the entire set-up was located within a windowless interior room where temperature was monitored and maintained at a constant 19.5(5)°C [14]. The average count rate for a 4 h live period was 2.5×10^7

[9]As published by the National Nuclear Data Center (NNDC)

counts with a statistical uncertainty of $\sqrt{N} = 5 \times 10^3$ counts. The 4.25 h real-time resulted in 10.7% dead-time rate. While the detector was live, it recorded the 834.8 keV γ emitted from ^{54}Cr as it de-excited to its ground state. The ^{54}Mn counts obtained during live-time data collection were normalised using the expected negative growth rate governed by a monotonic exponential decay $N(t) = N_o e^{-\lambda t}$. Here, Jenkins et al. calculate the decay constant $\lambda = 0.002347(2)$ d^{-1} from a least squares fit to the experimental data. They analysed the evident dip in ^{54}Mn count rate, seen in Fig. 2.11, to determine the deviation from expected counts over the interval. Considering an 84 h period from December 11 (22:52 UT) - December 15 (11:59 UT) they calculated the deviation of measured counts N_m from the expected number of counts N_e provided by an exponential decrease in the count rate. The deficit in counts over this period was found to be $(N_e - N_m) = (7.51 \pm 1.07) \times 10^5$ [14]. This deficit is significantly larger than the overall uncertainty expected from statistical fluctuations in ^{54}Mn count rates.

While the experiment was in progress, solar region 930 erupted in an X3 class solar flare on December 13, 2006 02:37 UT. Figure 2.8 shows an image of the entangled magnetic field around region 930 exploding as the storm continues, captured by Hinode's Solar Optical Telescope (SOT). The resultant coronal mass ejection (CME) ejected waves of relativistic heavy ions which caused radiation storms around near-Earth space for several days following the flare. Figure 2.9 is generated by NOAA's Geostationary Operational Environmental Satellites (GOES) and shows the sudden increase in long (1 - 8 Å) and short (0.5 - 4 Å) x-ray fluxes corresponding to the sudden eruption of active region 930. A more detailed graph of x-ray and energetic particle fluxes ejected during the storm is shown in Fig. 2.10. The increase in short and long x-ray bands and electron/proton/α-particle flux by several orders of magnitude coincident with the time of the eruption is clearly observable around the time of the storm and is typical for an event of this size.

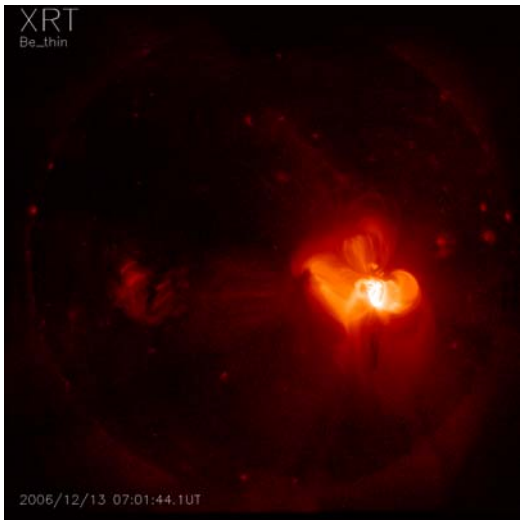

Figure 2.8.: Solar region 930 erupts in a class X3 solar flare. Image captured at 2006/12/13 7:01 UT. Courtesy of Hinode Science Data Center Europe.

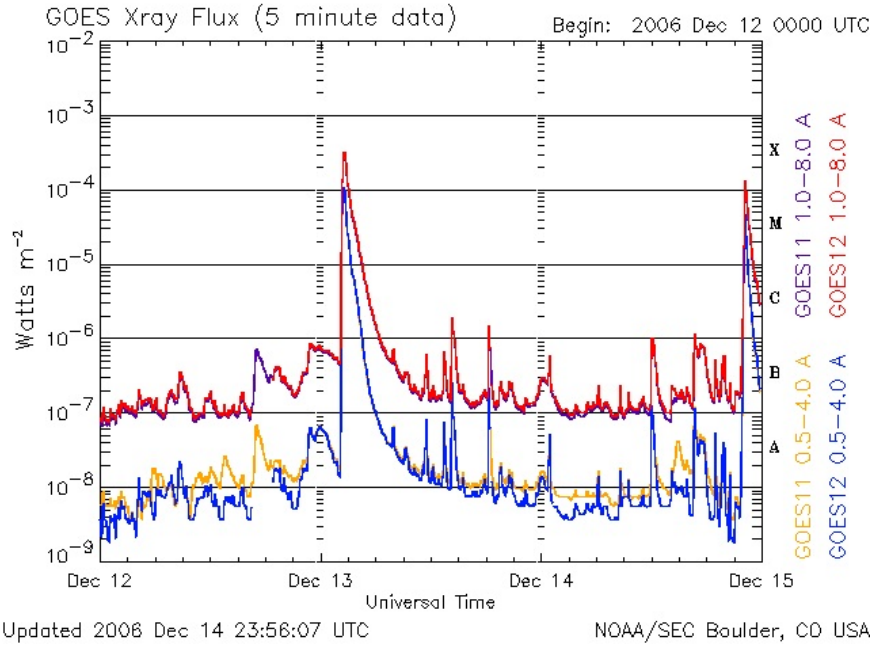

Figure 2.9.: 5 minute solar x-ray flux reported by GOES SEM for Dec 13-15, 2006. The sharp rise in long and short x-ray fluxes on Dec 13, 2006 correspond with the eruption of an X3 flare. Data courtesy of NOAA.

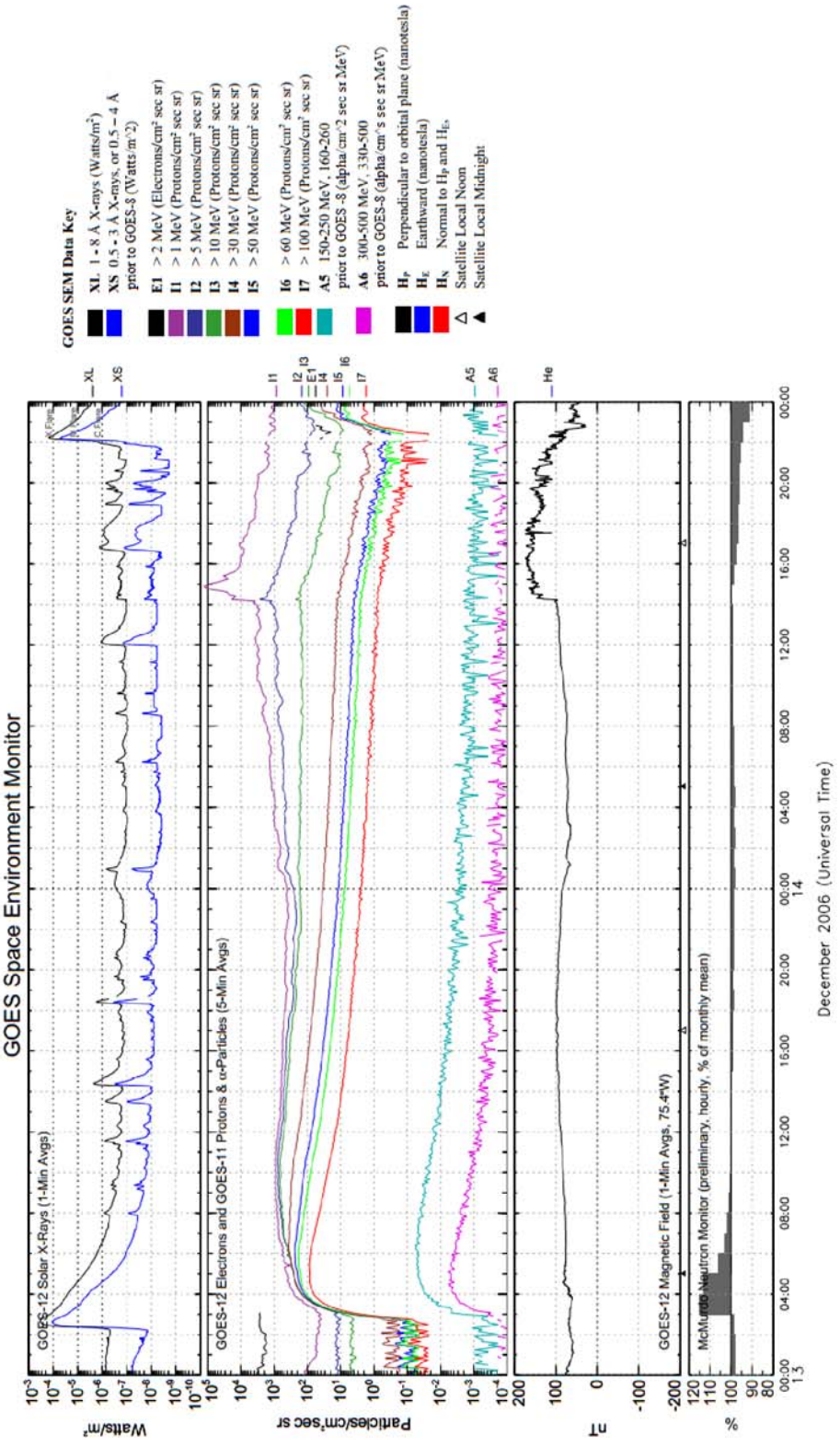

Figure 2.10.: Solar particle flux reported by GOES SEM for Dec 13-15, 2006. This plot was generated by the NGDC division at NOAA.

To investigate the correlation between the anomalous count rate and solar activity, Fig. 2.11 shows the normalised ^{54}Mn data superimposed with the x-ray flux recorded aboard GOES-11 for December 12, 2006 - January 1, 2006 [14]. There is a significant dip in ^{54}Mn counts from expectation coincident with the rise in the first peak x-ray flux that occurred with the X3 flare which was Earth directed (solar location S05W23). A second spike occurred on December 14 at 22:15 UT, again associated with a continued negative response from ^{54}Mn . A third and final spike on December 17 at 17:40 UT was accompanied by a larger deficit in count rate.

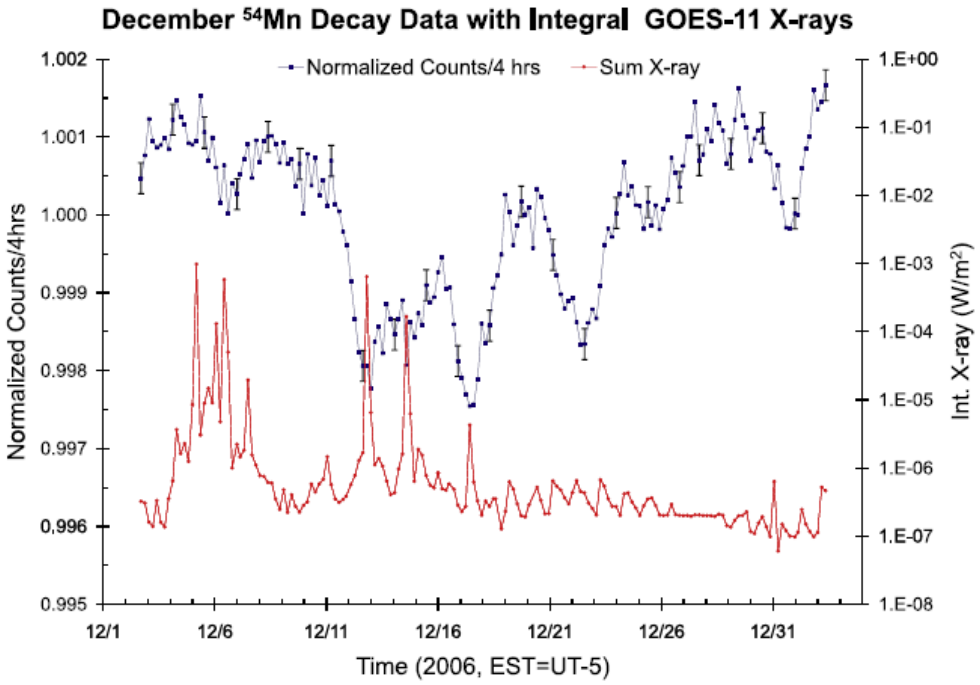

Figure 2.11.: Normalised ^{54}Mn counts during Dec 2006 overlayed with GOES-11 integral x-ray flux data. The ^{54}Mn data are 4 h count rates normalised to the expected rate, with error bars representing the fractional statistical uncertainty $\frac{1}{\sqrt{N}} \sim 2 \times 10^{-4}$. [14]

Other features in Fig. 2.11 deserve scrutiny as well. The X9 flare on December 5, considerably powerful in its own right, was not accompanied by any obvious fluctuations in the ^{54}Mn data. That this flare was not Earth directed (S07E79) hints to

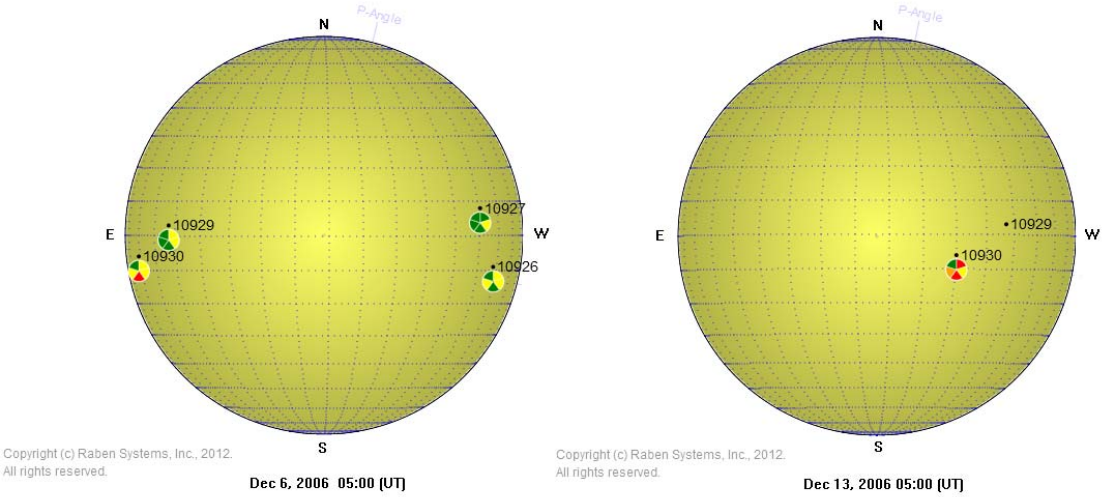

Figure 2.12.: Earth-face view of the Sun for Dec 6 and 13, 2006 at 05:00 UT depicting solar positioning for region 930. Solar events occurring towards the western limb of the Sun are most likely to be Earth-ward oriented. The X9 flare on Dec 5 was not Earth-directed and not accompanied by a significant dip in ^{54}Mn count rate. By Dec 13 region 930 had rotated toward the western solar limb and any solar activity from it is more likely to be Earth directed. Solar location of active regions are provided by SWPC division at NOAA.

a possible directionality in any effect solar activity may have on isotopic decay rates. The images in Fig. 2.12 provided by Raben Inc. show the Earth-side solar surface for December 6 and 13, 2006 (05:00 UT). The sunspot region locations are provided by SWPC. Events occurring in regions near the western limb of the Sun are most likely Earth-directed. Thus, the left image shows the orientation of energetic particles accelerated from Region 930 during the December 5 flare was not Earth-oriented, whereas this same region had completed a quarter solar revolution and had rotated towards the western limb (S05W23) by the 13^{th}.

2.3.1 Investigation into Possible Systematic Influences

We outline the results of a series of tests which were carried out to investigate the possibility that fluctuations seen in ^{54}Mn were a product of external influences on the detector system utilized in this experiment rather than on the rate of disintegration itself.

First, we examine fluctuations in line voltages feeding to the detector system. Neither the Purdue University power plant nor the Midwest Independent Systems Operator (MISO) that supplies power to Purdue University reported aberrant behaviour in neutral current flow during December 10-18, 2006. If the line voltage exceeded the 115 - 126 V range an alert would have been triggered by the Purdue power plant. No alerts were issued during the flare period. Additionally, the effect a power surge would have is to shift the 834.8 keV peak ROI which would have been corrected for during data acquisition.

In order to test the response of the NaI(Tl) detector under severe magnetic fields (larger than 100 times that seen immediately following the flare period), Jenkins et al. placed the detector crystal and PMT between a pair of Helmholtz coils 33 cm apart, its position similarly oriented to that during the actual flare period. The Earth's local magnetic field strength was determined to be 0.42(1) Gauss. For various values of the applied external field $|\vec{B}_{\oplus}|$= 0, 0.42 and 0.85 Gauss, none produced statistically significant fluctuations in the ^{54}Mn count rate [14]. To account for any effect changes in orientation might incur, the detector was also rotated 45° about its symmetry axis and the test was rerun, producing no new evidence of the detector being affected by strong external magnetic fields. It is important to note that the sharp spike in Ap index describing the Earth's geomagnetic field activity occurred on December 15, 2006 05:00 UT with the arrival of charged particle flux ejected from the flare, approximately 2 days after the initial X-class storm, whereas the decrease in ^{54}Mn count rates began over a day prior to any x-ray signal detected by GOES-11 [14].

2.4 Purdue ^{54}Mn Experiment

Since the initial counting period in December 2006, our collaboration took data on a 1 μCi sample of ^{54}Mn beginning November 13, 2008 till March 1, 2013. A 2 x 2" NaI scintillation detector records the gross count rate under a ROI peak centered around the 834.8 keV gamma emitted when the daughter ^{54}Cr decays to its ground state. The live-time period has been considerably shortened to 1 hr with an average dead-time of 2.7 %. The 1 hr data bins collect an initial count rate of 12.4 million counts with a fractional statistical error of 2.8 $\times 10^{-4}$. The experiment is carried out within a monitored and controlled environment where the detector system is sufficiently shielded with lead bricks, and the temperature, humidity and voltage are monitored. While gross counts provide a simple integration of the area under the ROI curve, for a more robust analysis it is beneficial to utilize the net counts detected. The net counts are corrected for effects arising from background sources such as ^{40}K and other contaminants, including cascade summing and pileup-effects within the detector.

After the initial runs were completed, an early check was carried out to confirm that data collected were indeed robust and the detector apparatus reliable. Figure 2.13 shows an early sample of data collected over December 2008. During this period the Sun was extremely quiet with virtually no occurrences of solar storms. As expected, the decay data show no signs of anomalous behaviour with the exception of an observable deviation of ^{54}Mn count rate from expectation on December 16, 2008. On December 16, 2008 at 9:30 UT, the Solar and Heliospheric Observatory (SOHO) captured images of a large Coronal Mass Ejection (CME) over the eastern solar limb shown in Fig. 2.14. The CME is assumed to be the product of an explosion on the far-side of the Sun, and further supports the possibility of directionality playing a role in solar activity affecting decay rates on Earth. Although NASA's Stereo-B satellite was situated over the solar eastern limb, its instrumentation was off-line; no flare activity or solar x-ray spikes were recorded during this time frame.

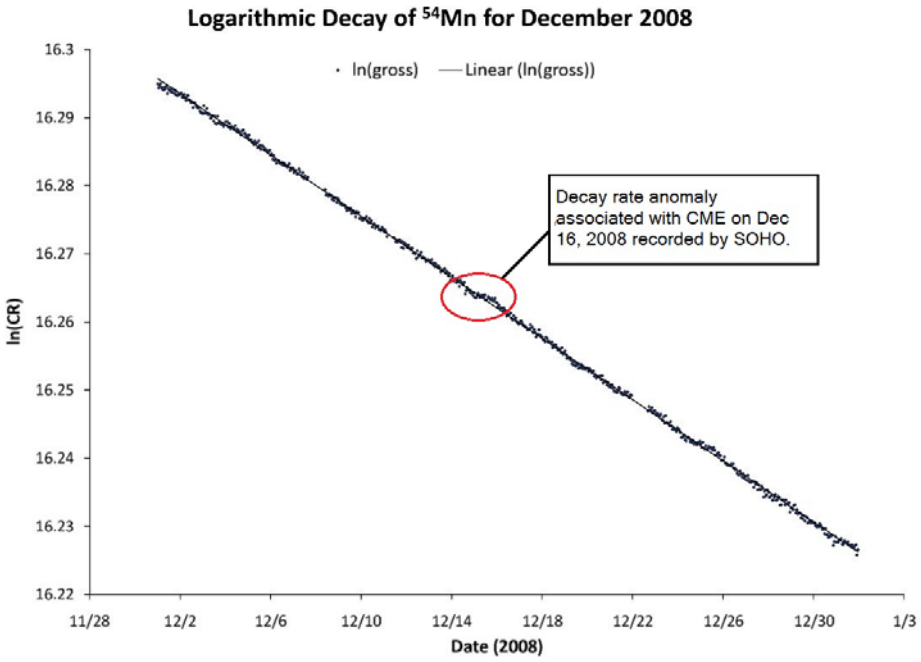

Figure 2.13.: Logarithmic plot of ^{54}Mn decay data during December 2008. A region of anomalous behaviour in the measured data on Dec 16 is coincident in time with CME activity occurring on Dec 16 at 09:30 UT.

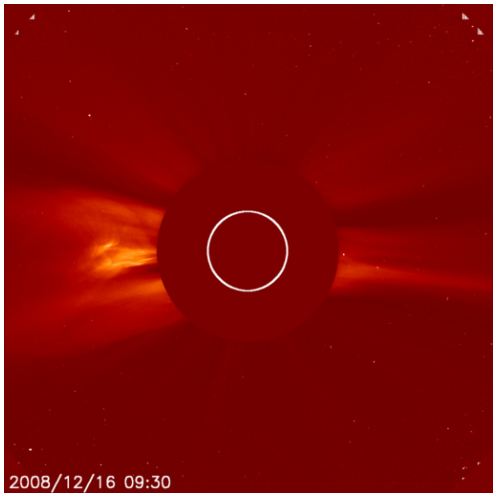

Figure 2.14.: Coronal Mass ejection erupts over the solar eastern limb on Dec 16 2008 at 09:30 UT. Courtesy SOHO (ESA , NASA).

Figure 2.15 shows a preliminary analysis of the ^{54}Mn data compared to the inverse squared Earth-Sun distance $1/R^2$. The decay data set spans 4 years from November 13, 2008 8:03 EST to March 1, 2013 4:03 EST. It is clear that as the sample ages, the activity declines and the relative error introduced by random fluctuation increases. The hourly net counts are averaged over daily bins and normalised by taking the residuals over the best fit to the data set. These normalised net counts per day are superimposed over $1/R^2$ data, in astronomical units, calculated at corresponding UTC time intervals for the entire 4 year period. Also included is a calculation of the 7-point moving average of decay data.

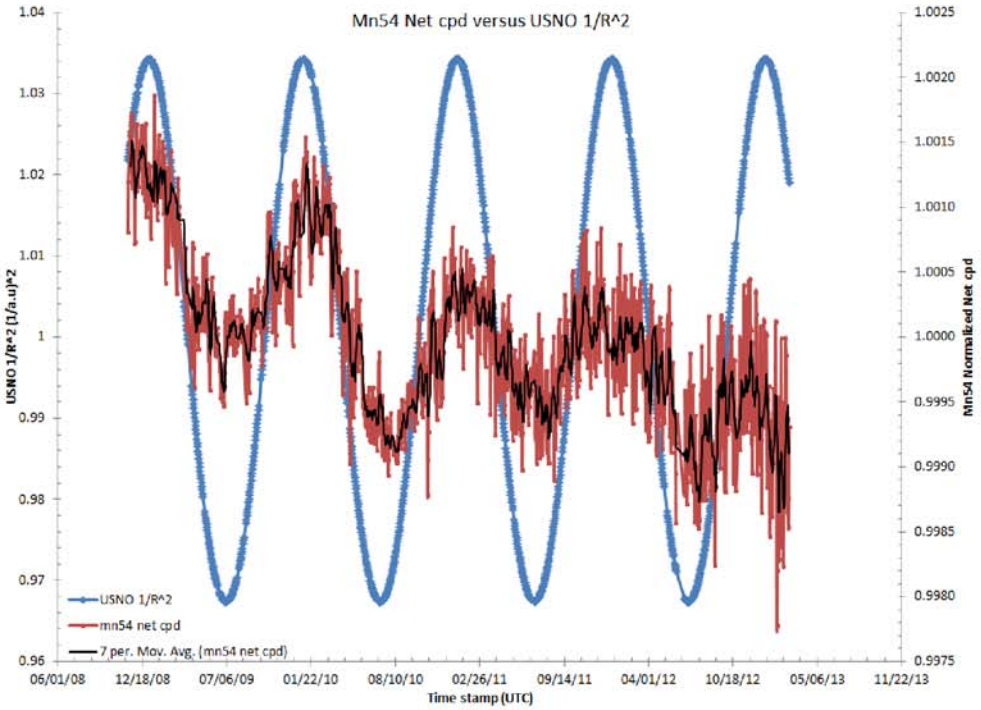

Figure 2.15.: ^{54}Mn normalised net cpd plotted against inverse-square Earth-Sun distance ($1/R^2$). Data covers the period from November 13, 2008 to March 1, 2013. The correlation coefficient determined is $\rho = 0.4986$. The probability that this coefficient value could arise from two uncorrelated data sets is 8.436×10^{-89}.

A Pearson correlation coefficient is similarly calculated to ascertain the likelihood of these two independent variables being correlated. This 4 year period, spanning almost 5 half-lives of the ^{54}Mn sample, includes N = 1399 daily averaged data points. Following the procedure outlined in Sec. 4.1, this translates to a correlation coefficient of $\rho = 0.4986$. For such a large sample size N, the probability that this coefficient value could arise from two uncorrelated data sets is 8.436×10^{-89}. Such a low probability indicates a highly significant relationship exists between the two data sets.

The results from a more in-depth signal detection analysis of the Purdue ^{54}Mn measurements are detailed in Chapter 6. We explore the possibility of short-time scale solar activity influencing decay rates and any directionality this effect may have. To this effect, we have constructed various testing algorithms and correlation procedures, outlined in Sec. 4, to identify regions of atypical decay behaviour within the decay signal and investigate the connection to periods of heightened solar activity.

3. Solar Activity

The solar surface is peppered with active regions, the frequency of which vary with either the 22-year solar-magnetic cycle or the 11-year sunspot cycle. Solar active regions are formed from clusters of sunspots and highly energetic solar material. Here, densely packed magnetic loops (Ω loops) form photospheric footpoints where they emerge (points of north polarity) and re-enter (points of southern polarity) the Sun. These Ω loops form distinctive structures in the active regions and are generated by the solar dynamo presumed to be located within the solar interior. Following Refs. [34–37], the magnetic flux emergence is associated with both large and small scale dynamo effects, where large-scale effects account for the more general characteristics of the field such as its cyclic behaviour and active regions. The latter are responsible for the occurrences of short-lived mixed polarity structures formed outside active regions. It is of general consensus though, that the global dynamo behaviour is a result of shearing flow seen at the tachocline lines. Specifically, the differential rotation rates just below the convection zone produce strong structured magnetic fields which support the solar dynamo mechanism. The small-scale dynamo is a consequence of the cyclonic turbulence within the convection zone, and as the field is transported across the region it is amplified by the large-scale shear in the overshoot regions below. This is where the turbulent motion reaches a boundary from an unstable layer to a stable one causing an enlargement of the area which is mixed by convection, feeding the large-scale dynamo effect. Finally, the large-scale field travels through the convection zone where it is either shredded and recycled or emerges through to the photosphere forming tightly coiled flux structures. The properties of the field structure are intrinsically different from a diffused field. This plays an important role in the development of instabilities in the stored magnetic fields and the evolution of the active regions. Typically, the magnetic field is concentrated

into intense field areas such as sunspots, which can grow up to 20,000 km in diameter with field strengths of 3000 G, or be scattered into smaller magnetic elements of a few hundred kilometres with field strength of 1000 G [38].

At approximately 0.25 R_{sun} the radiative zone emerges and continues up to $\sim 0.7\ R_{sun}$. Here solar material is hot and dense enough for energy to be transferred radiatively. At the tachocline, the uniformly rotating radiative zone, and differentially revolving convective zone, result in a large shearing force. In the convective zone temperatures are too low to allow radiation to continue; thermal columns form a signature which hint at the possibility of a solar dynamo creating the complex magnetic loops seen all around the Sun.

The visible surface of the sun, through which photons can now travel freely due to the decrease in H-ions, forms the photosphere. Here, solar spots, supergranules, bright fracules and plage are visible. Up to the photosphere temperatures have dropped to 6000 K. However, through the chromosphere and corona the temperature rises to $\sim 10^4$ K where visible flares and prominences can be seen above the eastern or western limb. Its high temperature makes the corona a source of long (1 - 8 Å) and short (0.5 - 4 Å) x-rays. During solar maxima it is a highly active region where changes in solar flares, filament eruptions, and the flow of solar material in post-flare loops can be observed.

The varying density of solar matter and its oblateness result in a differential rotation rate that varies with solar latitude. The synodic[1] rotation period varies with latitude where plasma-gas velocity decreases as you move outwards from the equator, from 27.27 d to nearly 30 d at the poles. The Carrington rotation is taken as a standard with synodic rotation period of 27.26 d at solar latitude 26°. Heliosisemology predicts that the hotter radiative zone rotates at a faster rate with a period of ∼13.10 days. The radiative zone rotates almost uniformly with the possible exception of the

[1] *Synodic* period references a coordinate system fixed with respect to Earth, measuring the time it takes for a fixed feature on the Sun to rotate to its same apparent position as viewed from Earth. A *sidereal* period is measured in a coordinate system fixed with respect to distant stars. The solar synodic period is larger than its sidereal period due to the Earth's orbiting around the Sun.

inner core. The region between rotation regimes experiences strong vertical shear and this layer is called the tachocline. These differences in solar rotation rates may be connected to the rotation signature, up to a phase shift, seen in the BNL, PTB, and Purdue ^{54}Mn data sets.

3.1 Solar Neutrino Production

Nuclear fusion reactions occurring within the Sun's core are responsible for the production of solar neutrino flux. Following the standard solar model, the p-p chain reactions are responsible for 98% of the 3.9×10^{26} Js^{-1} energy flux radiated by the surface of the sun [38] [39].

Table 3.1 lists the critical reactions within the p-p chain and the branching ratios associated with the various terminal points. Though all endings generate the same amount of energy— 25.731 MeV, which is simply the mass difference between the parent and daughter nuclei in the p-p chain ($4^1H \longrightarrow^4 He + 2e^+ + 2\nu_e$), it is the branching ratios of the various reaction chains which control the distribution of neutrino fluxes produced at various energies. Whilst the initial $^1H(^1H, e^+)^2D$ is responsible for the production of neutrinos with energies up to 0.420 MeV, the relative rates of $^3He(^3He, 2p)^4He$ and $^3He(^4He, \gamma)^7Be$ reactions determine the fraction of high energy solar neutrinos produced. According to the standard solar model calculation, 82.5% of the p-p chain terminates in $^3He(^3He, 2p)^4He$ (PPI) and 15.7% of the reactions follow the $^3He(^4He, \gamma)^7Be$ reaction. In the latter case, the ^{7}Be produced can β-decay by capturing either an electron or a positron, and it is by proton capture that neutrinos of highest energy ($E_{\nu max} \approx 14$ MeV) are produced. For the case of ^{7}Be capturing one of its own atomic shell electrons,[2] ^{7}Be will decay 89.5% to the ground state of ^{7}Li producing a neutrino of energy $E_\nu = 0.862$ MeV and 10.5% to the first excited state of ^{7}Li emitting an electron neutrino with energy $E_\nu = 0.384$ MeV.

[2]Due to the high pressure and temperature range of the solar interior, ^{7}Be atoms occur mostly in the ionised state. Thus the $^7Be(e^-, \nu_e)^7Li$ reaction occurs primarily by capturing a plasmic electron and the resultant decay rate is proportional to the electron plasma density within the core.

Finally in 0.02% cases the PPIII chain will occur where ^{7}Be will capture a proton and decay to ^{8}B. Though PPIII is only a small fraction in terms of the reaction branches, the $^7Be(p,\gamma)^8B$ termination is of considerable interest because of the high energy (14 MeV) neutrinos produced when the ^{8}B decays to and excited state of ^{7}Be .

Table 3.1: Principal reactions of the solar p–p chain. The p–p chain is responsible for 98.2% of energy generated from the $4^1H \longrightarrow^4 He + 2e^+ + 2\nu_e$ nuclear fusion reaction in the Sun. The three terminators of the p–p chain (Reactions # 4, 7 & 9), including various permutations of the C-N cycles, all generate the same total energy— 25.7 MeV. [40]

Reaction #	(Freq.)	Reaction	Neutrino energy (MeV)
1		$p + p \rightarrow^2 H + e^+ + \nu_e$	0.0 - 0.4
2		$p + e^- + p \rightarrow^2 H + \nu_e$	1.4
3		$^2H + p \rightarrow^3 He + \gamma$	
4	(82.5%)	$^3He +^3 He \rightarrow^4 He + 2p$	
5		$^3He +^4 He \rightarrow^7 Be + \gamma$	
6	(15.7%)	$^7Be + e^- \rightarrow^7 Li + \nu_e$	0.86, 0.38
7		$^7Li + p \rightarrow^4 He +^4 He$	
8	(0.02%)	$^7Be + p \rightarrow^8 B + \gamma$	
9		$^8B \rightarrow^8 Be + e^+ + \nu_e$	≈ 14

3.2 Flares and Coronal Mass Ejections

Solar flares are caused by the sudden release of magnetic energy ($\sim 10^{27}$ J) in the solar atmosphere and have a life-time ranging from a few minutes to several hours [41]. Flare phenomena are observed on the solar surface as a violent eruption in the Sun's atmosphere where plasma is superheated, accelerating electrons, protons and other heavy ions to super thermal energies. The excited region emits radiation at all wavelengths across the electromagnetic spectrum, from radio to gamma rays. The

resulting shock wave interferes with the Earth's lower ionosphere and geomagnetic field, and in extreme cases can cause geomagnetic storms.

Flares generally occur in active regions around sunspots where the sudden snapping of twisted magnetic field lines releases a burst of stored magnetic energy on reconnection. Much of this energy is initially discharged in the form of heat, non-thermal particles, waves and motion. The Sun supports strong magnetic fields that change annually and reverse direction every eleven years, near the solar minimum. Occasionally, a knot of closely occurring loops will reconnect to lower arcade loops leaving a helix of magnetic field lines unconnected to the rest of the arcade. The sudden violent release of energy in the corona on reconnection produces a solar flare and the disconnected helical field, along with any particles it contains, explodes outwards forming a Coronal Mass Ejection (CME). Particularly strong flares can result in CMEs large enough where a burst of solar wind carrying lighter isotopic plasma material and excited particles, is jettisoned out into space. The low solar wind speed (~ 400 kms^{-1}) causes the delay time between the onset of a flare and the interference effects seen in near-Earth space[3]. CMEs are very large scale eruptions (300 x 10^5 km compared to the < 1000 km scale for flares) and can span 120° of solar latitude or longitude, expelling up to 10^{10} tons of coronal material. [41]

The temporal evolution of a flare can be described by a series of phases [42]: the pre-flare phase, impulsive phase, flash phase, decay phase. During the pre-flare phase, the coronal plasma heats up and is visible in soft x-rays and extreme ultraviolet (EUV) rays. Electrons and other ions are accelerated into the impulsive phase where most of the energy is released. This phase is characterized by hard x-ray sources at chromospheric altitudes. Towards the end of the impulse phase thermal soft x-rays and H_α emissions reach their maxima and the rapid increase of H_α flux indicates the onset of the flash phase. In the decay phase much of the coronal plasma returns to its original state, except higher in the coronal atmosphere. Magnetic field reconnection occurs and plasma emissions and shock waves propagate outwards,

[3]The Forbush decrease following the December 13 2006 X3 flare occurred 37 hours after the Purdue ^{54}Mn count-rate began to decline. [14]

accelerating particles and producing radiation bursts which, for Earth directed flares, reach the lower ionosphere a few hours later. Figure 3.1 depicts a schematic of how the intensities at various electromagnetic wavelengths evolve during each phase of a solar flare.

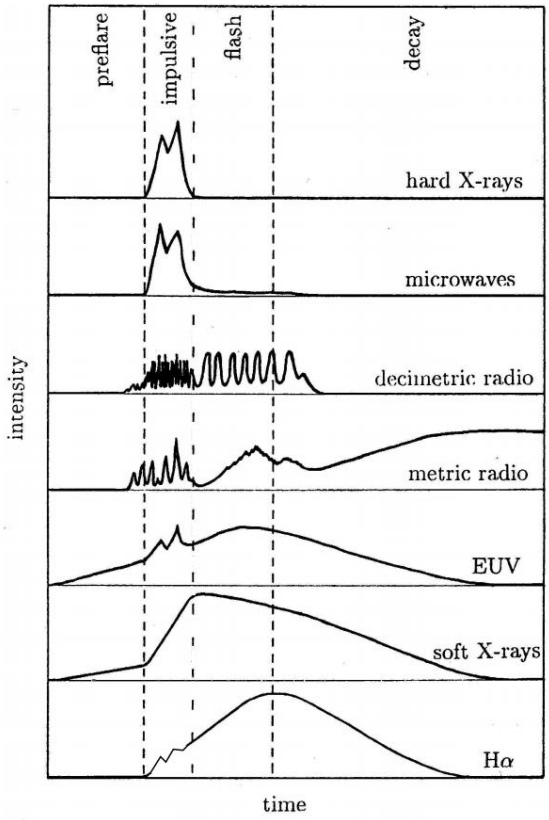

Figure 3.1.: Schematic of evolution of flare intensities at various wavelengths. [42]

3.2.1 Classification of Flares

Table 3.2 lists the two widely used classification systems that describe flare strength and/or size of solar storms. The first is the H_α classification scheme which is an optical method and was introduced in the 1930's. This scheme categorizes flares based on their area and brightness. The size is denoted by a character, S = subflare or

1, 2, 3 or 4 for successively larger flares given in terms of the solar hemisphere area A_H = 6.2 x 10^{10} km^2, and a letter describing a subjective estimate of the emission intensity: f = faint, n = normal, b = bright. Hence, the strongest flare is classified as 4b while the smallest and faintest will be Sf.

The second classification model was introduced in the 1970's. Geostationary satellites orbiting the Earth measure solar x-rays in the 1 - 8 Å band and categorize flares by their peak intensity on a logarithmic scale. Each event is described by a letter (A, B, C, M or X) corresponding to the order of the peak flux, i.e. $10^{(-8,\,-7,\,-6,\,-5\ or\ -4)}$ Wm^{-2}, and a number (from 1.0 to 9.9) that acts as a multiplicative factor. Thus, a B3.5 solar flare of middling strength has a peak flux of 3.5 x 10^{-7} Wm^{-2}.

Table 3.2: Solar flare classification schemes.

H_α SCALE		X-RAY SCALE	
Class	Area ($10^{-6}A_H$)	Class	Peak Flux (Wm^{-2})
S	$\leq$ 100	A	$\leq 10^{-7}$
1	100 - 250	B	10^{-7} - 10^{-6}
2	250 - 600	C	10^{-6} - 10^{-5}
3	600 - 1200	M	10^{-5} - 10^{-4}
4	$\geq$ 1200	X	$\geq 10^{-4}$

3.3 Effects of Solar Disturbances

Even a solar storm of moderate strength can cause sufficient damage in the vicinity around the Earth, over 90 million miles away. Solar winds propelled by flares cause disturbances in near-Earth space weather. These result in geomagnetic storms when CMEs propel streams of highly energetic charged particles which ionize the Earth's magnetosphere contributing to the aurora Borealis and aurora Australis.

The radiation emitted during a solar flare can be especially destructive to satellites and communication systems. Emissions that span the electromagnetic spectrum, from gamma rays to radio waves, affect the Earth's ionosphere. Radio waves and UV rays disrupt radar operations and other terrestrial communications systems operating at similar frequencies and damaging electric grids. Short x-rays heat up the upper atmosphere and cause orbital retardation of satellites by increasing the drag on low-orbiting satellites. During proton flares, large plasma ejections from the upper chromosphere release hard x-rays that can damage spacecraft electronics.

The risk that astronauts face if exposed to high levels of radiation during interspace walks is considerable. In such situations, they have only a few minutes after the initial photon burst from a solar eruption to find shelter before being bombarded with energetic particles which can pass through the human body causing biochemical damage. Exposure to high levels of gamma rays and microwaves can prove extremely hazardous to astronauts caught outside shielded areas. On December 13, 2006 activity aboard NASA space shuttle Discovery was interrupted when Sunspot 930 erupted in an X3 solar flare which set off a radiation storm forcing two astronauts, who were outside the space station, and those inside, to retreat to heavily shielded areas within the station.

Throughout history there have been numerous highly energetic explosions on the solar surface which have caused widespread interference with the Earth's atmosphere and geomagnetic field, resulting in large-scale damage to telecommunication systems and power facilities. Table 3.3 below lists a few of the strongest storms recorded, their strength, and a brief overview of the damage imparted.

Table 3.3: Highly energetic solar flares in history. Flare strengths are classified according to the x-ray flare scale (see Table 3.2). Included is a brief description of damage caused to communication and power services.

Date	Strength	Damage
1/9/1859	N/A	NASA reports the Carrington event to be the largest reported solar storm in the last 500 years. Global telegraph communications were interrupted, sparking fires and shocking operators.
4/8/1972	limit exceeded	Damaged/Interrupted long-distance phone communications over the Midwest and Canada. Forced AT&T to redesign its power system for transatlantic cables.
6/3/1989	X15.0	Power regulation at Hydro-Quebec Hydroelectric Complex failed leaving over 6 million without power. Transformers in New Jersey melted, with an estimated $6 billion in damage over the US Eastern Coast.
4/11/2003	X28+	Loss of a $450 million Midori-2 research satellite. Radiation effects were reported within deep-shielded areas aboard the ISS.
5/12/2006	X9.0	Disrupted satellite-to-ground communications and Global Positioning System (GPS) navigation signals. Damage to NASA's GOES-13 Solar x-ray imager instrumentation.

3.4 Current Methods of Observation

The first solar flare recorded in history was observed by R.C. Carrington (and independently by R. Hodgson) on September 1, 1859 [43]. Carrington noted the flare, now known as the Carrington event, as patches of intensely bright light adjacent to a group of dark sunspots. The original diagram by Carrington is shown in Fig. 3.2. Regions A to D mark the flare event; A and B indicate the initial positions of an extremely bright solar event which drifted to positions C and D over a 5 minute span before disappearing.

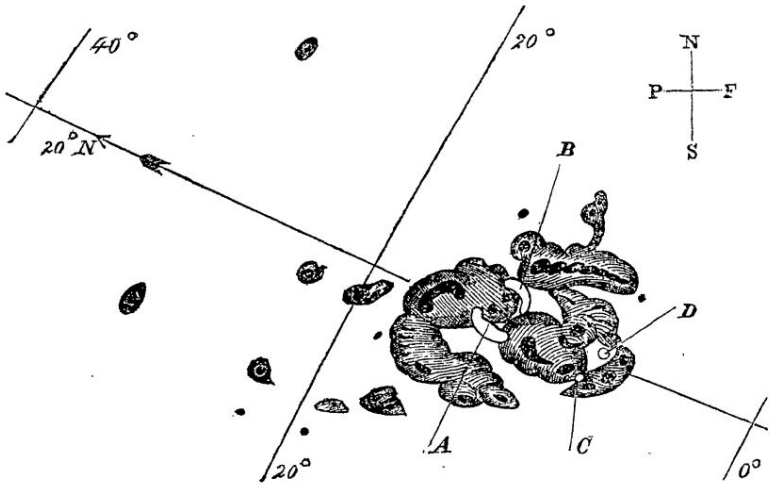

Figure 3.2.: Carrington flare on September 1, 1859. Pictured is an illustration by Carrington of the solar region he observed during the flare eruption. Locations A and B indicate areas of initial positions of the intensely bright event, which drift to C and D over a period of 5 minutes. [43]

CMEs were discovered much later with the advent of the coronagraph in 1930. The solar coronagraph is a telescope with a central disk attachment used to block out direct light from the Sun, this allows the corona and other nearby objects to be resolved. The Sun is about 10^6 times brighter than the corona and glare from the Sun would overshadow any images from objects near or around it. With the launch of the Skylab space station, and other space based coronagraphs such as the Large

Angle and Spectrometric Coronagraph (LASCO) aboard the Solar and Heliospheric Observatory (SOHO), images of CMEs are frequently recorded and studied in detail. In 1944, solar radio emissions were discovered and increases in near-Earth cosmic rays began to be associated with flare activity. With the detection of x-ray spectra from flare events, the theory that flare phenomena were confined only to thermal plasmic regions on the Sun had to be revised.

At present, a number of difficulties arise in detecting active regions on the solar surface. Solar flares are short-lived, highly energetic explosions that occur with little or no warning. Thus, observing sunspot clusters and activity complexes, whose lifetimes vary widely from a few weeks to several months, requires a characteristically different set of tests from those used to detect solar flares. Most current methods are visually based which can introduce a high level of subjectivity and error in flare analyses.

Currently, areas of high activity are identified from tabulations of *sunspot nests*, such as the Greenwich Photoheliographic Results, through a defined set of selection rules. Objective statistical techniques are applied to distinguish real clusters of active regions, reviewed and confirmed by Zwaan et al. [44]. Nests are determined from a set of characteristics which include a steady, if unique, rotation rate on the Sun, sunspot density, and ubiquity. Such protocols support the non-random spatial-time distribution seen in sunspot active sites. Another mode of detection studies the magnetic field line component of line-of-sight images of the Sun captured daily by the Vacuum Telescope of the National Science Observatory (NSO) at Kitt Peak, Arizona. Magnetic flux densities can be resolved up to three orders of magnitude, and the high resolution and range of the full-disk photospheric magnetograms pick out regions of high bipolar activity. Figure 3.3 shows a detailed view of an active region recorded on a full-disk magnetogram of the Sun taken on 27 May 1978 [45]. White regions signifying areas of positive polarity and dark regions correspond to negative polarity. Although this visual method allows one to track the boundaries of active sights, it poses an obvious subjective drawback.

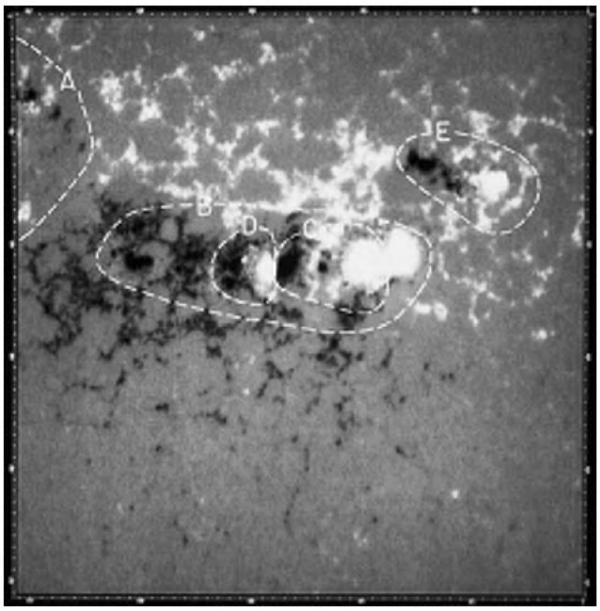

Figure 3.3.: Detailed view of full-disk magnetogram image of the Sun on 27 May 1978. Individual bipolar active regions are outlined with dashed curves. White and dark regions correspond to areas of positive and negative polarity respectively. [45]

A third pictorial method constructs stack plots where synoptic data comprised of specific latitudinal strips are assembled over a period of Carrington rotations. The stack plot illustrates a vertical track detailing the evolution of active region clusters for each hemisphere. They are constructed by stacking 30° latitudinal strips, per Carrington rotation, obtained from synoptic maps of the parallel component of magnetic flux $B_{||}$. These images reveal a cyclic change in active regions over the phase of a solar cycle. During the onset and decay of a solar cycle the clusters are widely spaced longitudinally but move close together during the phase of maximum activity. They also indicate an average lifespan of about 1 solar rotation for the majority of mid-sized clusters.

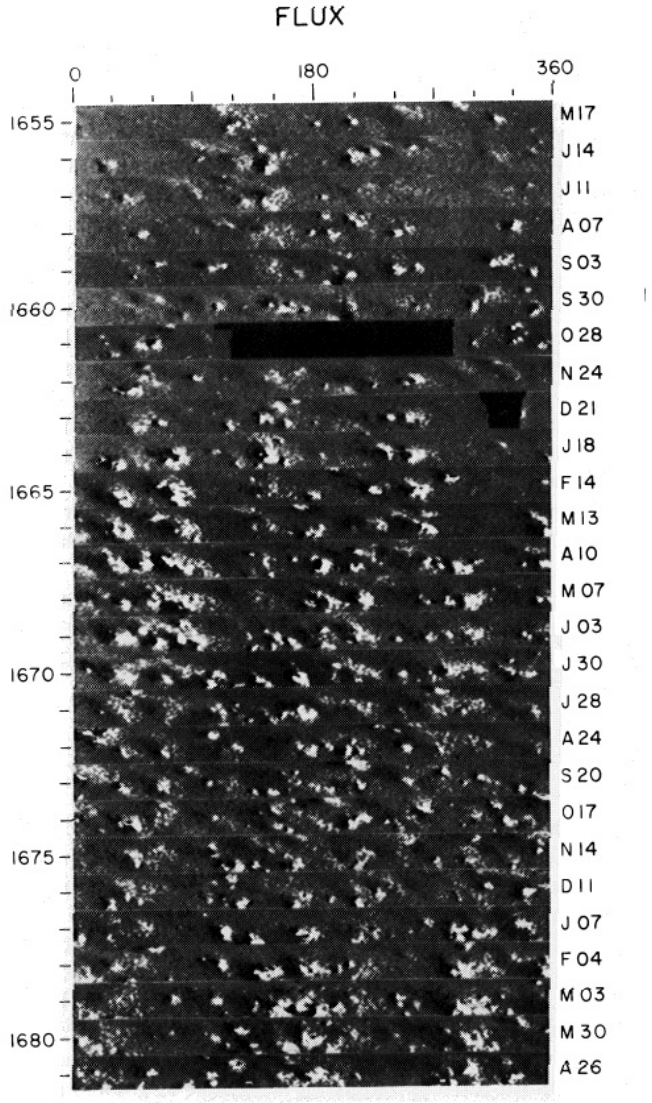

Figure 3.4.: Stackplot formed from strips of synoptic maps for latitudes N10-N40 over Carrington rotations 1655-1681 (1977-1979). The column is created from strips taken from FLUX maps. Numerals on the right specify month and day on which each Carrington rotation begins. Extended periods without observations are blacked-out. [45]

3.5 Solar Indices

To identify any apparent connection between discrepancies found in experimental nuclear decay data with activity occurring on the solar surface it is first necessary

to specify the various parameters and indices used to measure solar activity. Since almost all activity results from the spatial and temporal variation in magnetic flux, a value describing the solar magnetic flux would offer the best single index for solar occurrences. However, the magnetic flux cannot be measured directly, and various other factors determining this activity need to be studied. Solar indices describe the intensities and fluxes of various forms of radiation and energetic particles associated with flare activity. There are a large number of indices defined in the astrophysical community, but only those most relevant to this topic of research have been considered here.

3.5.1 10.7 cm Solar Flux

Sunspot number– a photospheric effect extrapolated from solar disk images, has now been supplanted by the more objective and consistent 10.7 cm solar flux index which measures a coronal effect. F10.7 is an estimation of the solar radio flux per unit frequency at a wavelength of 10.7 cm, emitted mainly by coronal plasma trapped in magnetic field loops. These radio emissions, measured in solar flux units (10^{-22} $\mathrm{Wm^{-2}Hz^{-1}}$), are observed over a range of wavelengths (2 - 50 cm) with greatest variability seen around 10 cm. The radio fluxes from active clusters correlate strongly with the sunspot number and general solar activity levels. Moreover, the F10.7 index has the added advantage of being a purely objective measurement, unbiased by the subjectivity of an observer. [41]

3.5.2 Ap Index & K Value

The Earth is under a constant shower of energetic charged particles from the Sun, where the particle flux and intensity varies with solar cycle and flare events. In general, the Earth's geomagnetic field is relatively unaffected by the small number of particles emitted by a 'quiet' Sun. However, during times of high sunspot activity and cycle maxima the increase in charged particle emission and radiation flux can interfere

considerably with the Earth's magnetic field and causing geomagnetic storms. The Ap and K values measure the condition of the Earth's geomagnetic field.

K value is a measure of the magnetic effects produced by solar particle fluxes. It is a local 3 hour average of magnetic activity, relative to an assumed *quiet* day, observed by a single geomagnetic observatory site. NOAA defines the planetary K index as the mean K value calculated from 13 different observatories from $46° - 6°$ geomagnetic latitude. It is a semi-logarithmic scale from 0 (quiet) to 9 (very disturbed) expressed in thirds of a unit. The Ap value is the earliest occurring maximum value within a 24 hour period calculated by an 8-point moving average of successive ap values— 3 hour "equivalent amplitude" of magnetic activity based on K index data. It is solely related to the solar event and does not take into account the start and end times of the UT day. The Ap index is a value from 0 to 400, and is a measure of the storm's peak intensity which makes it useful in categorizing solar storms events. Table 3.4 provides an indication of the relative intensities represented by each geomagnetic index.

Table 3.4: Ap index and K value relative strengths. Courtesy SWPC, NOAA.

Ap	K	Geomagnetic Field
0 - 3	0	Quiet
4 - 6	1	Quiet - Unsettled
7 - 14	2	Unsettled
15 - 47	3 - 4	Active
48 - 79	5	Minor storm
80 - 131	6	Major storm
132 - 207	7	Severe storm
208 - 400	8 - 9	Very major storm

3.5.3 Hard/Soft (Short/Long) X-rays

During solar flares a considerable amount of energy is transmitted to electrons present in the coronal plasma. A portion of these electrons are heated to super thermal temperatures while others accelerate out of the flare plasma at high energies. The latter couple with protons present in the plasma emitting bremsstrahlung radiation. X-ray photons with energies less than the electron energies are released and constitute the radiation signatures detected by satellite instruments. The spectral shape of such radiation helps distinguish between emissions from thermal electrons and accelerated non-thermal electrons. A thermal plasma emits lower energy (1 - 3 keV) soft (long) x-rays with a longer wavelength than the hard (short) x-rays produced by bremsstrahlung radiation from accelerated electrons at energies $>$ 30 keV. Hard x-rays in the lower energy range are produced from plasma with a temperature greater than 3 x 10^7 K. Data on hard and soft x-rays help construct the temporal evolution of flare activity and locate where flare energies are released. Figure 3.5 shows a 3 day plot of solar x-ray flux in the long (1 - 8 Å) and short (0.5 - 4.0 Å) x-ray passbands. Data are plotted in 5 minute averages, recorded by the SWPC primary and secondary GOES x-ray satellites.

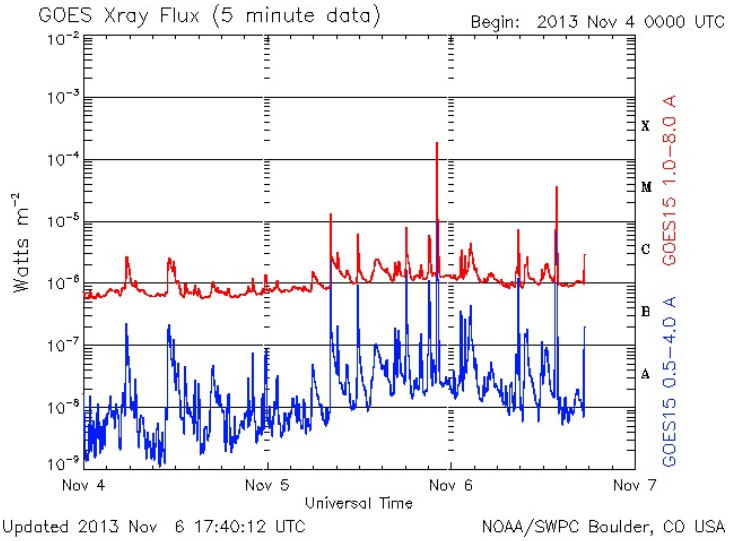

Figure 3.5.: A plot of 5 minute averaged solar x-ray flux in the long (1 - 8 Å) and short (0.5 - 4.0 Å) x-ray passbands. Courtesy SWPC, NOAA.

3.5.4 NOAA Solar Activity Indices

Space weather monitoring agencies, such as NOAA and SWPC, record a variety of observable phenomena that occur on the surface of the Sun, along with the corresponding geophysical effects. Following is a description of the solar events published by NOAA assembled from analyses of detected radiation and fluxes at various bandwidths, including observable phenomena on the Sun. Their close association with flare activity makes these indices of particular interest when studying the effects of solar conditions on radioactive decay rates.

1. Bright surge on the limb (BSL)- categorized as a bright stream of gas emanating radially outward from the chromosphere. Fanning outward, they surge over 0.15 solar radii over the limb.

2. Filament disappearance (DSF) - the sudden disappearance of a filament is a probable indicator of CMEs. The solar filament is often seen to ascend and then

either fall back into the Sun or simply fade within a time scale of minutes or hours.

3. Eruptive prominence on the limb (EPL) - the cloud-like prominences, which are filaments seen as bright ribbons over the limb, ascend into the solar atmosphere and are most often clearly seen in the H_α range (656.3 nm). Closely related to DSF.

4. Filament (FIL) - seen as dark ribbons against the solar disk, filaments form areas of gaseous masses suspended over the chromosphere by magnetic fields.

5. Optical flare observed in H_α (FLA) - A sudden explosion of energy in the atmosphere emitting particles and radiation. Generally on the time scale of minutes to hours. Flares are classified on the H_α scale according to the area of the eruptive site during maximum brightness (see Table 3.2).

6. Forbush decrease (cosmic ray decrease) (FOR) - associated with major magnetic field and plasma enhancements in the solar wind near Earth. FOR is a sudden decrease ($\geq$ 10%) in the cosmic background levels in near Earth space as recorded by neutron monitors. The change is presumed to arise from a deflection of charged cosmic ray particles by changes in the Earth's magnetic field brought about by the arrival of plasmic solar winds jettisoned by CMEs.

7. Ground-level event (cosmic ray increase) (GLE) - associated with solar proton events of energies $>$ 500 MeV. These are sudden surges in ground level cosmic ray levels ($\geq$ 10% of background). The initial relativistic burst is followed by fluxes of lower energy particles. Though rare events, occurring only a few times during each solar cycle, they generally follow after flare maxima lasting from a few minutes to hours.

8. Loop prominence system (LPS) - prominences form cloud-like features above the solar atmosphere and are observed as bright structures over the solar limb. LSP describes a system of prominences twisted into loops that bridge the magnetic

inversion line. With a lifetime of a few hours, they are most often associated with major flare activity.

9. Polar cap absorption (PCA) - Anomalous absorption and reflection of High frequency and Very-High frequency radio waves (3 - 300 MHz) and Low and Very-Low frequencies (3 - 300 kHz) respectively at lower altitudes in the Earth's polar ionosphere. PCAs follow the onset of major flares and reach a maximum value within 1 - 2 days of the onset. They occur simultaneously with high energy ($>$ 10 MeV) proton flux events and trans-polar radio paths may remain disrupted for days (up to weeks) after the end of such an event.

10. Fixed-frequency radio burst (RBR) - an RBR event indicates the peak value of radio bursts above pre-burst backgrounds at frequencies 245, 410, 610, 1415, 2695, 4995, 8800 and 15400 MHz. Intensities are reported in units of 1 flux unit (10^{-22} $Wm^{-2}Hz^{-1}$).

11. Radio Noise Storm (RNS) - short narrow-band bursts (300 - 50 MHz) of radio waves of variable intensity. (RNS) form Type I solar radio emissions and may last from several hours to days.

12. Sweep-frequency radio burst (RSP) - These events incorporate a variety of different types of radio noise associated with flare activities and complex active solar regions, spanning specific bandwidths. They are indicative of shock-waves moving across the solar atmosphere with intensities recorded on a relative scale from 1 (minor) to 3 (major).

    Type II - Slow drift burst (tens of minutes) across a narrow band (300 - 10 MHz).

    Type III - Rapid drift burst (seconds) across 500 - 0.5 MHz range.

    Type IV - Smooth continuum of broadband bursts across 300 - 30 MHz. Type IV emissions follow the onset of flare activity and can last up to several hours.

    Type V - Short-lived continuum burst in the dekameter range, generally associated with Type III activity.

Type VI - Series of Type III bursts over a period of 10 minutes or more, with no period longer than 30 minutes without activity.
Type VII - Series of Type III and V bursts over a period of 10 minutes with no period longer than 30 minutes without activity.

13. Spray (SPY) - luminous material ejected during solar flares propelled with velocities high enough (> 675 kms^{-1}) to escape the solar atmosphere. Sprays are measured in the H_α wavelength.

14. X-ray flare from GOES Solar X-ray Imager (XFL) : The Solar X-ray Imager (SXI) records full-disk soft x-ray images in the 0.6 - 6 nm band range. An SWPC algorithm is used to locate the brightest region in the SXI image associated with an x-ray event, which is assigned to the closest active solar region. XFL events record the regions of maximum area and intensity.

15. X-ray event from SWPC's Primary or Secondary GOES spacecraft (XRA) - XRA events measure the peak flux in the 1 minute 1 - 8 Å range. They are classified using the x-ray classification scheme outlined in Table 3.2, and are a direct measure of the strength of flaring regions.

Figure 3.6 lists a sample solar event report for November 2, 2013 generated by SWPC at NOAA. SWPC assigns an event number for each alert recording the start, end and peak times where applicable. In addition to the event type and its particulars, NOAA also reports the solar location in spherical heliographic coordinates of the active solar region, and its assigned region number.

```
:Product: 20131102events.txt
:Created: 2013 Nov 05 0332 UT
:Date: 2013 11 02
# Prepared by the U.S. Dept. of Commerce, NOAA, Space Weather Prediction Center
#
# Missing data: ////
# Updated every 30 minutes.
#                          Edited Events for 2013 Nov 02
#
#Event    Begin    Max       End  Obs  Q  Type  Loc/Frq   Particulars        Reg#
#-------------------------------------------------------------------------------

4040       0010   ////      0012  LEA  C   RSP  025-108   III/1

4050       0132   ////      0255  LEA  C   RSP  025-180   VI/1

4070       0431   ////      0503  LEA  C   RSP  025-180   VI/2

4060       0440   0446      0450  G15  5   XRA  1-8A      C8.2     2.7E-03   1885
4060       0443   0444      0458  LEA  3   FLA  S23W04    SF                 1885
4060       0446   ////      0450  LEA  C   RSP  076-180   II/1     584       1885
4060 +     0446   0447      0447  LEA  G   RBR  245       380                1885

4080 +     0554   ////      0648  LEA  C   RSP  025-180   VI/1

4090 +     0808   ////      0904  LEA  C   RSP  035-180   CTM/1
4090 +     0829   ////      0904  SVI  C   RSP  025-080   VI/1

4100      B0931  U0931     A0945  SVI  3   FLA  S12W05    SF                 1884

4250 +    A0949   ////     A2227  LEA  3   DSF  S24W02    7                  1885

4130       1035   1040      1047  G15  5   XRA  1-8A      C1.4     7.9E-04   1884
4130      B1037  U1040     A1134  SVI  3   FLA  S14W04    SF       ERU       1884

4140       1112   1115      1118  G15  5   XRA  1-8A      C1.6     3.5E-04

4150 +     1211   ////      1212  SVI  C   RSP  025-135   III/2

4160      B1252  U1312      1359  SVI  3   FLA  S12W06    1F       ERU       1884
4160       1254   1307      1319  G15  5   XRA  1-8A      C4.3     4.8E-03   1884

4170       1321   ////      1322  SVI  U   RSP  120-150   III/1
4170       1321   ////      1407  SAG  C   RSP  025-180   VI/1
```

Figure 3.6.: Sample list of SWPC/NOAA generated solar events for November 2, 2013. Detailed information on the event type including time of occurrence, observing facility, solar location and active region number are reported. Courtesy SWPC, NOAA.

4. Detection Algorithms

This section outlines the mathematics of all analysis methods employed in our investigation and in the signal detection code *Changemaster* . For each hypothesis, we tailor a number of testing algorithms that indicate which, if any, of the various data sets show signs of decay fluctuations that exceed statistical expectations. The following sections introduce the statistical background necessary for understanding the signal detection algorithms implemented. Also included are the mathematics describing change detection tests executed in *Changemaster* .

4.1 Correlation Coefficient

A correlation coefficient function between two random variables, X and Y, tests for a linear association between the two. The correlation coefficient $\rho_{(x,y)}$ depends on the covariance $\sigma_{(xy)}$ between two data sets and each set's standard deviation σ_x, σ_y.

For a set of measurements $\{x_i\}$ of a normally distributed variable X of sample size N, the standard deviation σ_x of X provides a reasonable measure of the random uncertainties, of x_i from the mean value $\bar{x}$.

$$\sigma_x^2 = \frac{1}{N}\sum_{1}^{N}(x_i - \bar{x})^2 \tag{4.1}$$

Similarly the covariance σ_{xy} provides a measure of the degree to which residuals of two variables track each other. Should there be no dependence, the covariance would approach zero.

$$\sigma_{xy} = \frac{1}{N}\sum_{1}^{N}(x_i - \bar{x})(y_i - \bar{y}) \tag{4.2}$$

The Pearson coefficient of correlation $\rho_{x,y}$, defined in Eq. (4.3), has a value between 1 and -1. A value of $\rho_{x,y}$ close to ± 1 implies a strong linear relationship between two variables. [46]

$$\rho_{x,y} = \frac{\sum(x_i - \bar{x})(y_i - \bar{y})}{\sqrt{\sum(x_i - \bar{x})^2(y_i - \bar{y})^2}} \tag{4.3}$$

The significance of obtaining any particular value ρ_o can be quantified as a probability $P_N(\rho_o)$ defined in Eq. (4.4). The probability $P_N(\rho_o)$, calculates the probability that two *uncorrelated* variables each of size N, will produce a correlation ρ_o. It follows that a small value for $P_N(\rho_o)$ is indicative of a highly correlated relationship between the two data sets. By convention, a probability $P_N(\rho_o) \leq 5\%$ is said to be a *significant correlation* and $P_N(\rho_o) \leq 1\%$ is a *highly significant correlation* [46].

$$P_N(\rho_o) = \frac{2\Gamma[(N-1)/2]}{\sqrt{\pi}\Gamma[(N-2)/2]} * \int_{|\rho_o|}^{1} (1 - r^2)^{(N-4)/2}\, dr \tag{4.4}$$

In Eq. (4.4) Γ denotes the standard gamma function $\Gamma(z)$ where:

$$\Gamma(z) = (z-1)! = \int_0^\infty t^{z-1} e^{-t} dt \tag{4.5}$$

4.2 Signal Detection Algorithms

A set of measurements $\{x_i\}$ of a random variable X with a sample size N, will be the source of any statistical inferences we make. If X is described by a probability density $p_\lambda(x)$ which depends on a scalar parameter λ, then a detection algorithm will be based on observing a change in this parameter [47]. To develop this technique we require the definition of the likelihood ratio

$$\frac{p_{\lambda_1}(x)}{p_{\lambda_0}(x)} \tag{4.6}$$

where $\lambda = \lambda_0$ characterizes the null hypothesis H_o before any change has occurred, while λ_1 is indicative of evidence for a different hypothesis H_1 after a change in the

sample has occurred. The sufficient statistic $l_i(x_i)$ is defined as the logarithm of the likelihood ratio

$$l_i(x_i) = ln\frac{p_{\lambda_1}(x_i)}{p_{\lambda_0}(x_i)} \tag{4.7}$$

For a data set of size N, the log-likelihood ratio S_N is simply the sum of all sufficient statistics $l_i(x_i)$ from $i = 1, ..., N$

$$S_N = \sum_{i=1}^{N} l_i \tag{4.8}$$

Detectability of a change in the signal follows the definition of an optimal decision rule d which depends on some given threshold h for a given test. If the log-likelihood ratio should exceed this threshold an alarm is triggered, indicating a deviation from the null hypothesis. The alarm time t_a occurs just after the first sample for which the decision function equals 1. That is

$$d = \begin{cases} 0 & \text{if } S_N < h; \quad H_0 \\ 1 & \text{if } S_N \geq h; \quad H_1 \end{cases} \tag{4.9}$$

4.2.1 Two-Sided Cumulative Sum

Following Refs. [47] and [48] we summarize the use of the two-sided cumulative sum statistic.

A two-sided cumulative sum (CUSUM2) test is a quality control scheme that tests for changes in the average level of a given variable. In this case, the detection rule is a measure of the difference between the cumulative sum S_k, see Eq. (4.8), and an adaptive threshold $\mu_0 \pm hs$, where μ_0 is taken as the reference mean value, s refers to standard deviation of variable X, and hs with $h > 0$, defines the interval within which the hypothesis being tested is true. Thus, the upper and lower bounds are given by

$$\begin{aligned} S_k^+ &= max\Big(S_{(k-1)}^+ + x_k - \mu_0 - \alpha s\Big) \\ S_k^- &= max\Big(S_{(k-1)}^- - x_k + \mu_0 - \alpha s\Big) \end{aligned} \tag{4.10}$$

where the first line in Eq. (4.10) checks for an increase in the mean value μ of variable X while the second equation tests for a decrease. Here $\alpha : \alpha > 0$ acts as a "forgetting factor" allowing a buffer around the mean. In general, the theory of sequential processing prescribes the parameter α to be half of the mean shift expressed in standard deviations. A CUSUM2 test, with $\alpha = \frac{1}{2}$, tests for a one standard deviation shift from the reference mean μ_o.

The triggered alarm time t_a will occur when either S_k^+ or S_k^- exceeds their respective upper or lower bounds defined in Eq. (4.10). That is

$$t_a = min(k : S_k^+ \geq hs \ \cup \ S_k^- \leq -hs) \tag{4.11}$$

4.2.2 Geometric Moving Average

The geometric moving average (GMA) is another example of a signal processing test that analyses the behaviour of the log-likelihood ratio $l_i(x_i)$ defined previously. The GMA test accomplishes this by introducing an exponential weighting factor W_i (see Eq. (4.12)), to the data set $\{x_i\}$ of an independent random variable X that follows a Gaussian distribution. Data are weighted temporally with weights decreasing as a geometric progression from more recent observations to older ones. [47] [49]

$$W_i = \alpha(1-\alpha)^i \ ; \qquad 0 < \alpha \leq 1 \tag{4.12}$$

where α is a forgetting factor with a value between 0 and 1 included. Thus, the most recent data are given a weight of α, and its immediate predecessor falls off as $(1-\alpha)$ successively. For a reference mean $Z_0 = \mu_o$, the weighted decision function for an independent random variable X is

$$
\begin{aligned}
Z_k &= \sum_{i=1}^{N} W_i \, l_{k-i} \\
&= (1-\alpha)^k \mu_o + \alpha(1-\alpha)^{k-1} l_1 + \alpha(1-\alpha)^{k-2} l_2 + ... + \alpha(1-\alpha) l_{k-1} + \alpha l_k \\
&= (1-\alpha) Z_{k-1} + \alpha \, l_k \\
&= (1-\alpha) Z_{k-1} + \alpha(x_k - \mu_o)
\end{aligned} \tag{4.13}
$$

The last line in Eq. (4.13) describes the decision rule for an independent normally distributed variable X. If X has a standard deviation σ, then the standard deviation σ_{Z_k} for the geometric moving average is [49]

$$\sigma^2_{Z_k} = \frac{\alpha}{2-\alpha}(1-(1-\alpha)^{2k})\sigma^2 \tag{4.14}$$

For the corresponding two-sided case the magnitude of the GMA function $|Z_k|$ tracks the changes in X up to a limiting value σ_Z which defines a threshold for detection $\mu_o + h\sigma_Z$ for $h > 0$,

$$\sigma_Z = \sqrt{\frac{\alpha}{2-\alpha}} \, \sigma \tag{4.15}$$

The alarm time t_a is the earliest time the magnitude of GMA crosses a defined threshold $\mu_o + h\sigma_z$.

$$t_a = min(k : \ |Z_k| \geq h\sigma_z) \tag{4.16}$$

4.2.3 Slope Test

An elementary, yet effective test, for detecting a change in an incoming signal is by analysing its slope. A set of measurements $\{A(t_i)\}$ that follow an exponential distribution is described by the probability function as

$$A(t) = A_o \exp(-\lambda t) \tag{4.17}$$

where A_o specifies an initial condition satisfying $A(t)$ and $\lambda > 0$ describes the rate of exponential change, which in this case is negative. Taking the logarithm of Eq. (4.17) will generate a straight line, where λ now describes the slope of this line based on a least squares fit to the measurements. The resulting fit will provide the averaged value λ_o which can can be used as a reference mean. If we consider a smaller window $\{A(t_k)\}$, described by A_{o_k} and λ_k for comparison, then the slope test defines a detectable change when the magnitude of difference between λ_k and λ_o reaches some threshold h; $0 < h < 1$ as a function of the mean value. The alarm times flagged will be

$$t_a = min(k : \ |\lambda_k - \lambda_o| \geq h\lambda_o) \tag{4.18}$$

Changemaster utilizes two variations of the slope test to detect regions of data showing significant deviations in half-life values. The Tslope test is a direct application of the procedure described above, where the reference value λ_o is obtained from a fitted model over a large sample size of data that extends beyond the region of interest on both sides. Tslope compares the deviation of the slope λ_k obtained from $\{A(t_k)\}$, to the reference value λ_o and looks for a detectable change. The second test, Dslope, is a more adaptive test where the size of the smaller data set $\{A(t_k)\}$ is increased by small increments $t_k \rightarrow t_{k+j}$ for some integer j. In this case, Dlsope triggers the alarm if the difference between any of the slopes calculated from the $\{A(t_{k+j})\}$ data sets and the reference λ_o exceed the threshold $h\lambda_o$.

4.2.4 Runs Test

The Runs test is adapted from the theory of runs to track changes in the incoming signal, and utilizes the longevity of disturbances as a measure for triggering a decay

anomaly. Given a sequence of data points $\{x_i\}$, the theory of runs defines a run as a succession of similar events that are preceded and followed by different events, and the number of elements in a run is referred to as its length [50]. Thus, the runs test searches for a region in the decay signal where consecutive data points act similarly to satisfy some condition αh. For instance, for a run of length 8, an alarm is triggered if a point x_i is found to exceed some threshold $\alpha_1 h$, where h is measured in number of standard deviations away from a reference mean μ_o, *and* 2 of the previous 3 data points $\{x_{i-2}, ..., x_i\}$ exceed $\alpha_2 h$, *and* 7 of the last 8 points $\{x_{i-7}, ..., x_i\}$ are either all greater than or less than the reference mean.

4.2.5 F-Probability Test

Following the properties of a negative binomial distribution, the F-Probability test (PROB) constructs an expected mode of decay to compare against experimental measurements. This test is a prediction algorithm that focuses on isolating intervals over which the count rate differs significantly from its probabilistic value, given the behaviour of past activity. For a radioactive sample of N_a atoms that follow the usual exponential decay law, the probability p_o of any one atom decaying within a time t_o is

$$p_o = \frac{N_a(0) - N_a(t_o)}{N_a(0)} \tag{4.19}$$

$$= 1 - \exp(-\lambda t_o) \tag{4.20}$$

where $\lambda = \ln(2)/T_{\frac{1}{2}}$ is the isotope's specific decay constant.

Assuming a number N_x decays, or successes, have occurred within this time period, the probability of $N_r = N_a - N_x$, atoms remaining, or failures, will follow a negative binomial distribution

$$P(N_r) = \binom{N_a - 1}{N_x - 1} p_o^{N_x} \, (1 - p_o)^{N_r} \tag{4.21}$$

where the binomial coefficient is defined as

$$\binom{n}{m} = \frac{n!}{m!\,(n-m)!} \tag{4.22}$$

If we wish to take account of possible dead-time effects in the detector, we can consider two cases: 1) apparatus dead-time is disregarded and the detector continues to operate until time t_1, or 2) dead-time is taken into account by assuming that the detector is insensitive to incoming disintegrations for some time t_d. For the first case, the decay probability p_1 of having N_y atoms decaying over a period t_1 is similar to the probability defined in Eq. (4.19), now over a time t_1. Since the detector observes all decays during t_1, the conditional probability of detecting a further N_y decays during the interval t_1 given N_r atoms survived at the end of interval t_o, is

$$P(N_y|N_r) = \binom{N_r}{N_y} p_1^{N_y} \, (1 - p_1)^{N_r - N_y} \tag{4.23}$$

where the complete probability of N_y atoms decaying is given by

$$P(N_y) = \sum_{r=0}^{\infty} P(N_y|N_r) P(N_r) \tag{4.24}$$

The expectation value and standard deviation are now:

$$\langle N_y \rangle = \frac{(N_x)(1 - p_o)}{p_o} p_1 \tag{4.25a}$$

$$\sigma = \frac{[N_x(1 - p_o)p_1(p_o + p_1(1 - p_o))]^{1/2}}{p_o} \tag{4.25b}$$

Equations (4.25a,b) predict the most likely number of decays that should occur within a time t_1 given a certain number of decays that have occurred in the past at t_o.

In the second case, the detector equipment is insensitive to incoming decays for dead-time t_d. We adjust for dead-time by determining the number of atoms remaining, N_s, at the end of time t_d, and then use N_s to predict the number of decays N_y over time $t_2 = t_1 - t_d$, instead of N_r. The binomial distribution describing the dead-time adjusted sample size at time t_d is

$$P(N_s|N_r) = \binom{N_r}{N_s}(1-p_d)^{N_s}(p_d)^{N_r-N_s} \tag{4.26}$$

where p_d is the probability of an atom decaying during time t_d. The resultant number of atoms that decay, N_y, within a period t_1 can be determined following the discussion outlined in the first case, where the surviving sample size is N_s instead of N_r. The resultant expectation values and standard deviations for the number of decays is

$$\langle N_y \rangle = \frac{(N_x)(1-p_o)}{p_o}(1-p_d)p_1 \tag{4.27a}$$

$$\sigma = \frac{[N_x(1-p_o)(1-p_d)p_1(p_o+p_1(1-p_d)(1-p_0))]^{1/2}}{p_o} \tag{4.27b}$$

Additionally, adjusting starting positions and time intervals allows us to generate multiple predictions $\{n_p\}$ for the projected number of decays N_y. The n_p predictions are weighted by their $(1-p_d)$ factors— predictions determined from more recent observations are weighted more heavily.

Once a weighted average of predictions is made, we can calculate the difference between this average and experimentally recorded decay data by

$$r = \frac{N_m - \langle n_p \rangle}{\langle \sigma_p \rangle}, \tag{4.28}$$

where r is the residual, N_m is the measured number of decays, $\langle n_p \rangle$ is the weighted average of the multiple predictions, and σ_p is the standard deviation of the weighted average. A PROB flag is produced when two or more consecutive residuals are either

greater than or less than the reference mean. Each flag is given two separate strengths defined as

$$A = \sum_{n=i+1}^{j} \frac{1}{2} \left(t_n - t_{n-1}\right) \left(r_n - r_{n-1}\right), \tag{4.29a}$$

$$E = \prod_{n=i}^{j} 2\mathrm{erfc}\left(|r_n|\right), \tag{4.29b}$$

where i and j are the indices of the initial and final residuals included in the flag, and $erfc(z)$ describes the complementary error functions at each point.

$$erfc(z) = \frac{2}{\sqrt{\pi}} \int_z^{\infty} e^{-t^2} dt \tag{4.30}$$

A measures the total area under the curve created by plotting the residuals and is used to produce AREA flags when it exceeds a threshold A_t. Whereas, E measures the probability of having a sequence of normally distributed random variables with residuals of at least the observed magnitudes and lead to ERFC flags.

4.3 Spectral Analysis

Spectral analysis techniques are robust methods for processing time series sinusoidal functions in statistics and signal processing theory. In its simplest form, spectral analysis calculates the power S, the square of the amplitude of an oscillating function, for a given frequency ω, in a normally distributed time series with a mean of zero and variance of unity. Depending on parameters available for adjustment (such as frequency, phase, etc.), and quality of data (resolution, etc.), there are a variety of algorithms to choose from. In the BNL and PTB experiments, the non-uniform sampling rate of data collection, and gaps in the Purdue ^{54}Mn data from routine detector down-times, play a deciding factor. This temporal non-uniformity in the data precludes use of a Fast Fourier Transform (FFT) which requires a uniform discrete

sampling frequency. For this reason, we employed a Lomb-Scargle search [51]. The standard deviation is used as the error term and the resulting power spectral density (PSD) or periodogram, is a graph of powers characterizing the presence of frequencies present in the sample tested.

4.3.1 Lomb-Scargle Procedure

The Lomb-Scargle process is a spectral analysis technique used to resolve an incoming data signal $X(t)$ into a series of sinusoids describing the frequency make up f of the original signal [51].

$$X(t_i) = A\cos(\omega t_i - \tau)Z(t_i) + B\sin(\omega t_i - \tau)Z(t_i) + n(t_i) \tag{4.31}$$

where $\omega = 2\pi f$ and A and B are the fitted amplitude to the cosine and sine functions. The noise at time t_i is given by $n(t_i)$ and a weighting function $Z(t)$ describes an arbitrary function that controls the modulation of amplitudes. $Z(t)$ could represent an exponential, Gaussian or any other function which describes the signal being modelled. If $Z(t)$ is a parametrized function, the parameters are presumed known—for an exponential decay function the decay constant is known. The resulting periodogram gauges the power S of a sinusoidal signal, i.e. the square of its amplitude, against a specified range of frequencies f. Hence, the periodogram ranks a series of models, each describing a specific frequency, and the width of each peak is a measure of the uncertainty associated with it. For a null hypothesis where data are drawn from a constant rate distribution, the powers are expected to follow an exponential distribution e^{-S}, where e^{-S} is a measure of the probability of obtaining such a power S or larger from the sample by chance.

A specific advantage the Lomb-Scargle procedure has over other spectroscopy methods is that it develops a working algorithm for dealing with unevenly-spaced data. The Lomb-Scargle test weights data on their measured value rather than by a specific sampling period. The non-uniform sampling rate then requires the definition

of a time delay parameter τ which satisfies an orthogonality condition between any pair of sinusoidal signals at time t_i. Thus, the periodogram remains unaffected if all t_i were shifted by a constant value. Under this premise, since X is assumed to be a random variable, the time delay parameter is given by

$$\tau \equiv \frac{1}{2\omega}\, arctan\left[\frac{\sum_i sin(2\omega t_i)}{\sum_i cos(2\omega_i t_i)}\right] \tag{4.32}$$

Let X denote an actual data sample of size N, let I refer to all information available a priori and assign a Gaussian noise prior probability distribution to the data. Using the sum rule of probability theory and the usual definitions for mean $\bar{x}$ and standard deviation σ, the posterior probability $p(\omega|XI)$ [51] is given by

$$p(\omega|XI) \propto \int_{-\infty}^{\infty} dA \int_{-\infty}^{\infty} dB \int_{0}^{\infty} d\sigma\ \sigma^{-(N+1)} \exp\left(-\frac{Q}{2\sigma^2}\right) \tag{4.33}$$

where

$$Q \equiv N\bar{x^2} - 2AR(\omega) - 2BI(\omega) + A^2C(\omega) + B^2S(\omega) \tag{4.34a}$$

$$\bar{x^2} = \frac{1}{N}\sum_{i=1}^{N} X(t_i)^2 \tag{4.34b}$$

$$R(\omega) \equiv \sum_{i=1}^{N} X(t_i)\cos(\omega t_i - \tau) \tag{4.34c}$$

$$I(\omega) \equiv \sum_{i=1}^{N} X(t_i)\sin(\omega t_i - \tau) \tag{4.34d}$$

$$C(\omega) \equiv \sum_{i=1}^{N} \cos^2(\omega t_i - \tau) \tag{4.34e}$$

$$S(\omega) \equiv \sum_{i=1}^{N} \sin^2(\omega t_i - \tau) \tag{4.34f}$$

Using the results of Eq. (4.34), Eq. (4.33) becomes

$$p(\omega|XI) \propto \frac{1}{\sqrt{C(\omega)S(\omega)}}[N\bar{x^2} - P_X(\omega)]^{\frac{2-N}{2}} \tag{4.35}$$

where $P_X(\omega)$ is the sufficient statistic. The sufficient statistic describes the power scale which will now be a function of frequency where the index i is summed over the length of a data series from 1 to N. Under this premise, since X is assumed to be a random variable one would expect the power spectrum $P_X(\omega)$ to also be randomly distributed

$$P_X(\omega) = \frac{R(\omega)^2}{C(\omega)} + \frac{I(\omega)^2}{S(\omega)} \tag{4.36a}$$

$$= \frac{1}{2\sigma^2}\left[\frac{[\sum_i (x_i - \bar{x})\ cos\ \omega(t_i - \tau)]^2}{\sum_j cos^2\omega(t_i - \tau)} + \frac{[\sum_j (x_i - \bar{x})\ sin\ \omega(t_i - \tau)]^2}{\sum_i sin^2\omega(t_i - \tau)}\right] \tag{4.36b}$$

Apart from uneven sample times, measurements may be recorded at a frequency higher than the average Nyquist frequency. In signal processing theory, the Nyquist frequency f_n is defined as half the sampling rate of the data set.

$$f_n = \frac{f_{sample}}{2} \tag{4.37}$$

Assuming the phase is known, to resolve the amplitude and frequency of a periodic signal, one requires a minimum of 2 data points, as shown in Fig. 4.1. If measurements are taken once a month then the shortest period that can be resolved from the data is

$$\frac{1}{f_n} = \frac{2}{1} = 2 \text{ months} \tag{4.38}$$

Frequencies lower than the sampling rate can be recovered from the original signal, but frequencies higher than the Nyquist frequency introduce an aliasing effect. Aliasing is a well known phenomenon in sampling theory where frequencies greater than the Nyquist frequency are indistinguishable from the lowest possible frequency which resolves the incoming signal. In particular it can be seen as a leakage of power from high frequencies into lower frequencies. Thus, the non-uniform sampling rate

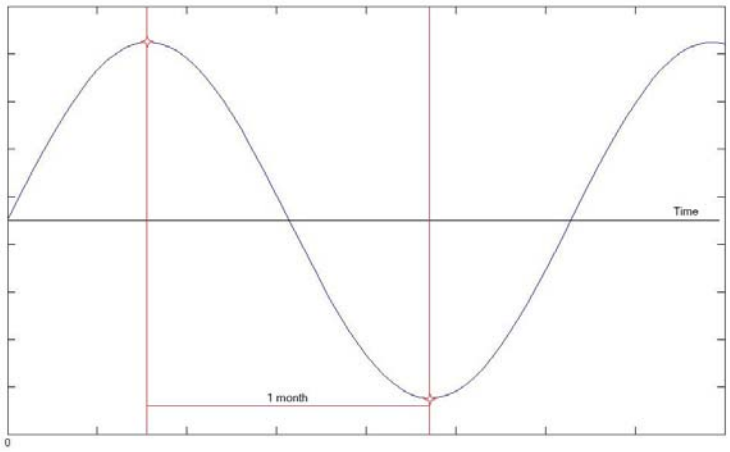

Figure 4.1.: Periodic signal sampled at a rate of 1 month^{-1}. The shortest period that can be resolved from this sampling rate is given by the Nyquist limit and is a signal with a period of 2 months.

requires us to define an average Nyquist frequency $\bar{f}_n$. The average Nyquist frequency provides an upper bound for the range of frequencies tested, while the experimental lifetime acts as a minimum frequency value. $\bar{f}_n$ also allows weighting based on the original sampling frequency spread.

False Alarm Probability

If the null hypothesis indicates that the power spectrum density $P_X(\omega)$ describes a purely random sequence, then the False-Alarm probability p_{FA} of obtaining a PSD $P_X(\omega)$, for a specified power S or greater, at a given frequency ω against the null hypothesis is given by Eq. (4.39). Since the Lomb-Scargle periodogram is normalised using σ^2, the resulting $P_X(\omega)$ for a particular frequency follows an exponential probability distribution with average unity

$$p_{FA} = 1 - (1 - e^{-S})^{N_\omega} \tag{4.39}$$

where N_ω is the number of independent frequencies tested for within a given bandwidth. Working with this definition for the False Alarm Probability, a statistically significant peak is one with $p_{FA} < 5\%$, i.e. the peak is deterministic at 95% confidence level.

5. CHANGEMASTER Algorithms

The primary computational package we have developed to run signal detection analyses on experimental nuclear decay measurements is called *Changemaster* . Code is written in C++ with the aid of MATLAB— a high-level language and interactive environment designed for numerical modeling and algorithm development. *Changemaster* utilizes a number of specifically designed routines to detect deviations in the incoming decay signal from a monotonically decreasing exponential model. The following algorithms (outlined previously in Sec. 4) identify specific anomalous structures within the incoming signal generating "decay hits". These hits are subsequently filtered and aggregated to produce "decay flags" that are strong indicators of regions of fluctuations.

i. Runs Test (Sec. 4.2.4)

ii. Two-Sided Cumulative Sum (Sec. 4.2.1)

iii. Geometric Moving Average (Sec. 4.2.2)

iv. TSlopes Test (Sec. 4.2.3)

v. DSlopes Test (Sec. 4.2.3)

vi. F-Probability Test (Sec. 4.2.5)

These tests are carried out on a set of normalised decay rate measurements $R(t)$. The decay data set is treated by calculating the difference between the natural logarithm of the incoming count rate N_m and that prescribed by the expected theoretical behaviour $N_{exp} = N_o e^{-\lambda t}$, where λ is obtained from a linear regression of the data.

The residuals are normalised, with a mean about 0 and an expected standard deviation of 1, by dividing out the expected standard deviation σ_N of the data set to give the normalised data set $R(t)$:

$$R(t) = \frac{1}{\sigma_N} \ln\left(\frac{N_m}{N_{exp}}\right) \tag{5.1}$$

Figure 5.1 depicts a short period of the natural logarithm of the measured ^{54}Mn data taken during May 2010, compared against the linear regression to the data along with the predicted behaviour of the isotope generated by the F-Probability test. These two comparison curves will be used as reference levels for measuring variations in

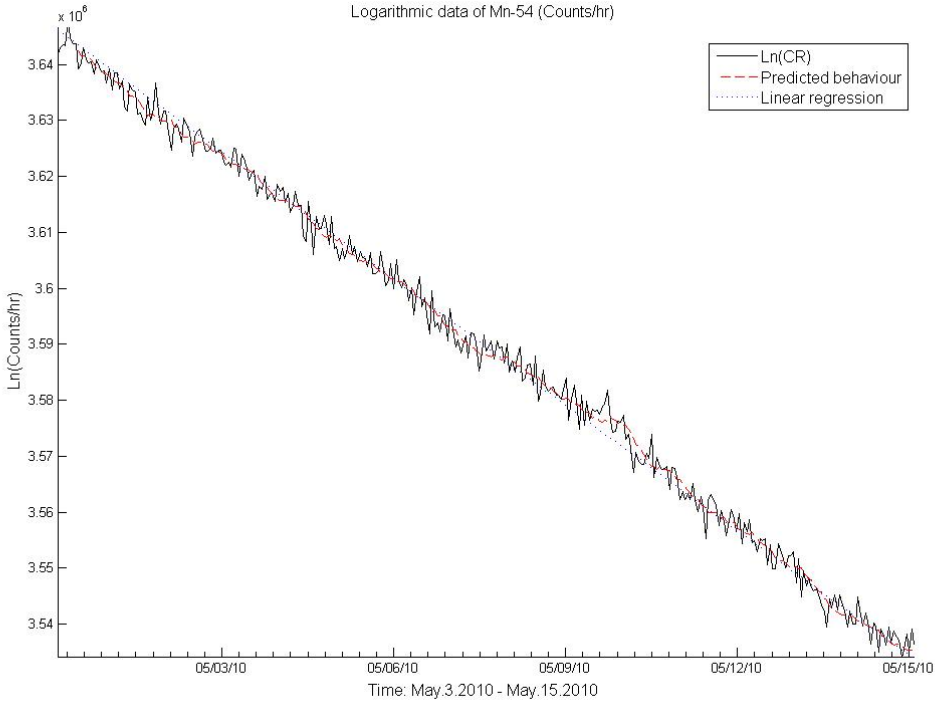

Figure 5.1.: Natural logarithm of ^{54}Mn data during May 2010. Expected decay behaviour (blued dashed curve) and predicted count rate produced using the F-Probability test (red curve) are also plotted.

the ^{54}Mn measurements. The parameters and thresholds for each algorithm testing for fluctuations have been optimised in 1-year periods. Table 5.1 lists the 2010 test parameters for the variables as described in Sec. 4.

The Two-sided Cumulative Sum (CUSUM2) checks for changes in the average level of an incoming signal and generates a decay hit when the cumulative sum of the number of decays exceeds a 2 standard deviation threshold from the expected mean [47,48]. The Geometric Moving Average (GMA) test introduces an exponential weighting factor $W_i = \alpha(1-\alpha)^i$ to the data set, where α is a forgetting factor set at 0.25. The data are weighted temporally with weights decreasing as a geometric progression from more recent observations to earlier ones [47,49]. The Runs test (RUNS), adapted from the theory of runs [50], analyzes data in 8 hour intervals. A hit is generated if all of the following conditions are met: (a) a measurement x_i is found to be h_1 standard deviations from the expected value μ_o, (b) 2 of the previous 3 measurements $\{x_{i-2}, ..., x_i\}$ exceed the expected model by h_2 standard deviations, and (c) 7 of the previous 8 measurements $\{x_{i-7}, ..., x_i\}$ show a positive increase from μ_o. In the following analysis, for data the year 2010, $h_1 = 1.6$, $h_2 = 1$ and the data are normalised with $\mu_o = 0$. The D-slope (Dslope) and T-slope (Tslope) tests assume a monotonic exponential decrease as the expected model of decay, and compare the measured ^{54}Mn half-life within a sliding window to a larger time frame over which the decay behaviour is averaged. The T-slope test calculates the decay constant obtained from a 40 hour interval and generates a hit when there is 35% discrepancy between this value and the decay constant describing a coincident 2 week region of data. The D-slope test works similarly with the addition of an adjustable inner window size, thus singling out regions of short-lived deviations in count rate as well as larger fluctuations in decay rates compared to the current rate. Finally, the F-probability test (PROB), described in detail in Sec. 4.2.5, makes a projection for each measurement from the average of 10 predictions calculated using previous data to project forward in time.

It follows that test thresholds are increased for periods of high anomalous activity within the data and vice versa. Once the alarm times from every test are recorded, the

resulting "hits" are filtered to produce 4 different types of decay flags: Variety (VRTY), Multiplicity (MULT), Area (AREA), and Complementary Error Function (ERFC). The VRTY and MULT flags are constructed by aggregating the first 5 types of hit tests, while the AREA and ERFC flags are produced separately via probabilistic predictions made from the PROB test.

Table 5.1: Optimized *Changemaster* test parameters for 2010. The parameters for each test are adjusted to provide the optimal quality control schemes (a.k.a detection algorithms) to identify changes in the incoming signal. See text for details.

Test	2010	Parameters		
Runs	1.6 (std)	1.0 (std)	8	
GMA	2.0 (std)	α =0.25		
CUSUM2	2.1 (std)			
TSlope	35 %	40 (hr)	336 (hr)	
DSlope	28 %	6 (hr)	54 (hr)	264 (hr)
Prob	10 predictions	$T_{\frac{1}{2}} = 311.4$	2	

VRTY and MULT flags are generated when hits created by the first five tests listed in Table 5.1 are analyzed and grouped according to frequency and type. A VRTY flag is then produced when there are 2 or more hits of distinct types within a 48 hr interval. To prevent repetitive flagging of overlapping 48 hr windows, the initial period is extended by 6 hours incrementally until either no new hits are found in the extended window or it reaches a maximum length of 72 hours. All hits within this window are grouped into a single VRTY flag, and the flag mean-time is calculated from an average of every included hit time. The MULT flags are similarly generated when a minimum of 5 hits are triggered within an initial 48 hour interval. Thus, the VRTY flags indicate positions where a variety of tests create hits at approximately the same time in the data, and the MULT flags identify groupings of hits. Figure 5.2 shows a sample output of the Purdue ^{54}Mn data for the period August 2011 to October 2011.

The first graph plots the total number of hits within a given window and the second graph plots the number of distinct tests that were triggered within a given window. For each graph the threshold levels are noted in red. Of particular interest to this analysis are locations which produce both MULT and VRTY flags coincident in time.

The AREA and ERFC flags are calculated using the results of the F-Probability test (PROB) outlined in Sec.4.2.5. Multiple predictions made by the PROB test are used to generate a weighted average for the count rate. The difference between the measured counts and averaged prediction expressed in standard deviations, produces a strength of deviation, r_s in the decay rate:

$$r_s = \frac{N_m - \bar{n_p}}{\sigma_{n_p}} \tag{5.2}$$

where N_m is the measured number of decays, $\bar{n_p}$ is the weighted average of the multiple predictions, and σ_{n_p} is the standard deviation of the averaged predictions.

Changemaster scans these r_s values for regions where two or more consecutive points are either all positive or all negative. Each of these instances is flagged, and the resulting flags are filtered by strength. Each probability flag uses a specific method for determining the strength of the flag. The first method, used to create AREA flags, defines the strength as the numerical value of the integral of r_s values over the time frame of the flag. The second method, used to create ERFC flags, defines the strength as the product of the complementary error functions *erfc(z)* at each point. For example, if a flag consists of 2 points both with a r_s value of 1, then the ERFC strength would be approximately $(0.32)^2$. This can be interpreted as a standard normal random variable having $\approx 32\%$ probability of being 1 or more standard deviations away from the mean. Only AREA flags with strength above a pre-determined bound are retained. Similarly, ERFC flags are issued when the product of complementary error functions surpasses an upper limit.

A data tree detailing the flow of decay data through *Changemaster* is outlined in Fig. 5.3 . *Changemaster* inputs the normalised ^{54}Mn count rate producing an array of hits triggered from the 6 signal detection tests. Hits from the 5 hit tests: RUNS,

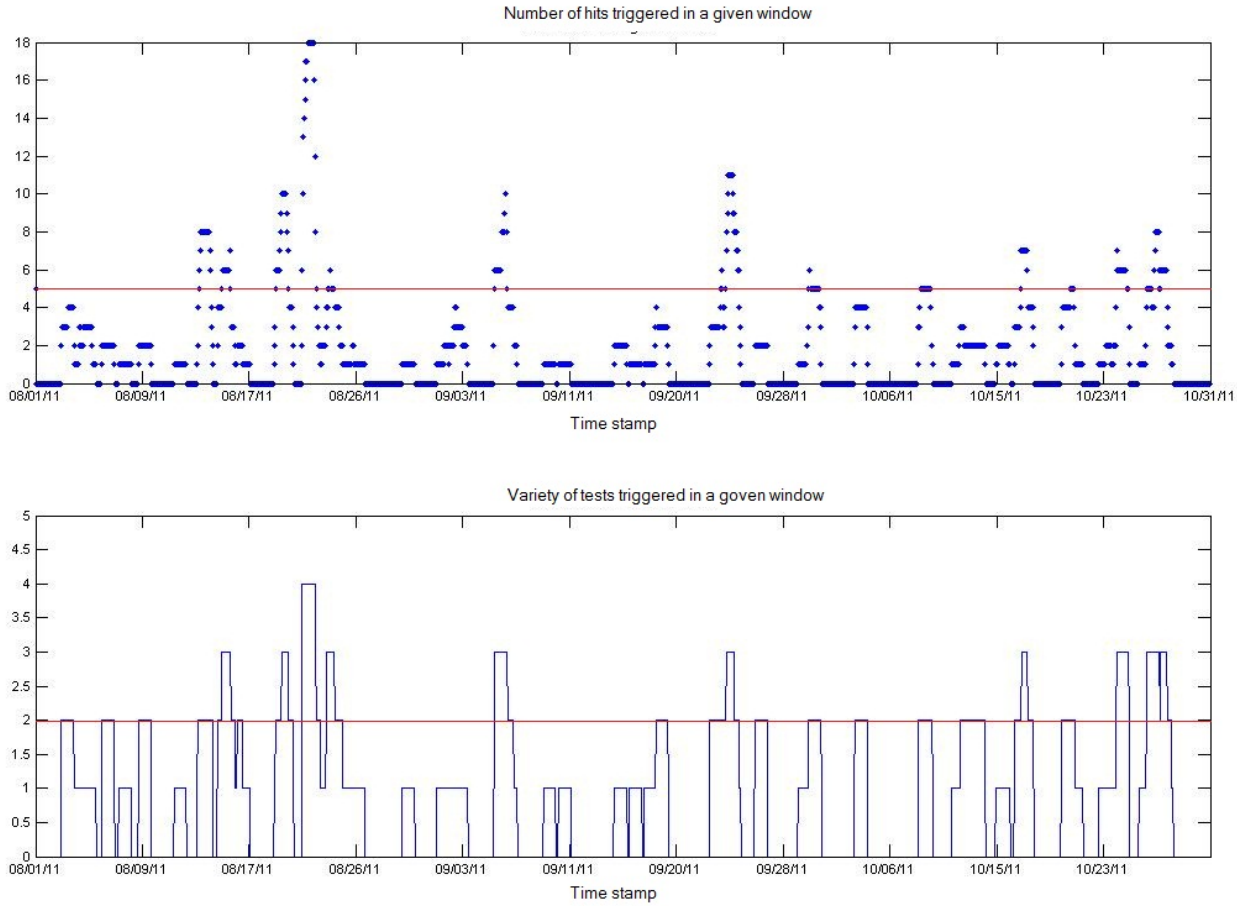

Figure 5.2.: Multiplicity and Variety flag outputs for August-October 2011. Normalised ^{54}Mn data are processed by the CUSUM2, GMA, RUNS, Tslope and Dslope tests, generating triggers during periods of fluctuations in decay rate. The resulting hits are aggregated and filtered to produce decay flags. Thresholds in red indicate that 5 or more hits are required to produce a MULT flag, and 2 or more distinct hit types will generate a VRTY flag. Note the coincidence in times between the MULT and VRTY flags, suggesting the occurrence of solar events.

CUSUM2, GMA, Tslope and Dslope are combined to form the MULT and VRTY decay flags. Regions of the projected data which exceed thresholds set by the PROB test will produce AREA and ERFC flags. The resulting decay flags are complied into the output file *Masterflaglist*. It is the contents of *Masterflaglist* which will be used to check for correlations between distributions of solar events.

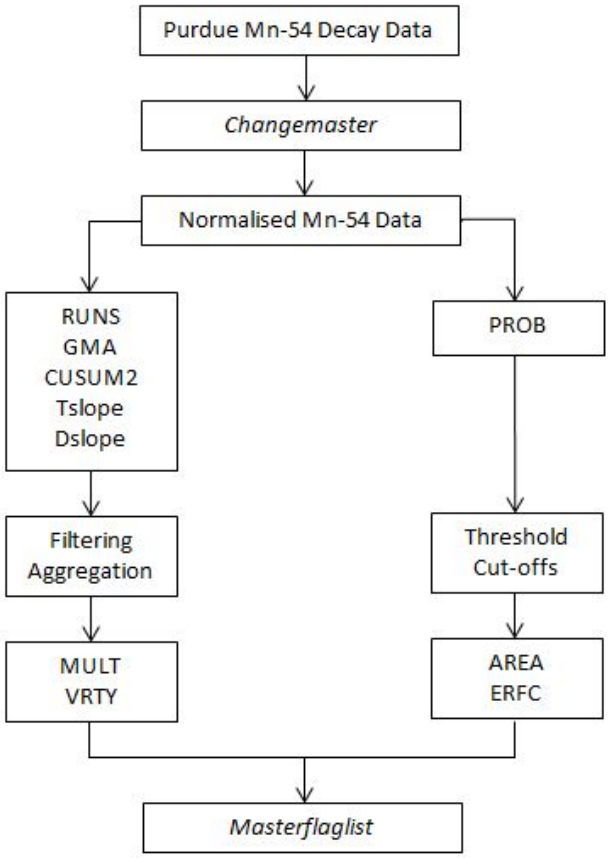

Figure 5.3.: Flow of decay data through *Changemaster* . The program analyses normalised decay data for anomalies in the incoming signal. Using a variety of signal detection algorithms and cut-off thresholds, aggregated decay flags are listed in the text file *Masterflaglist*.

Figure 5.4 shows the output of the *Changemaster* analysis for hourly normalised Purdue ^{54}Mn decay data for August 2011 to October 2011. Superimposed in black are positions of the decay hits produced by the signal processing algorithms. As can be seen, not all hits result in decay flags, which are ultimately indicators of significant deviation in decay behaviour. Additionally, in a number of instances different flag types overlap temporally, reducing the total number of distinct anomalous regions in the decay signal.

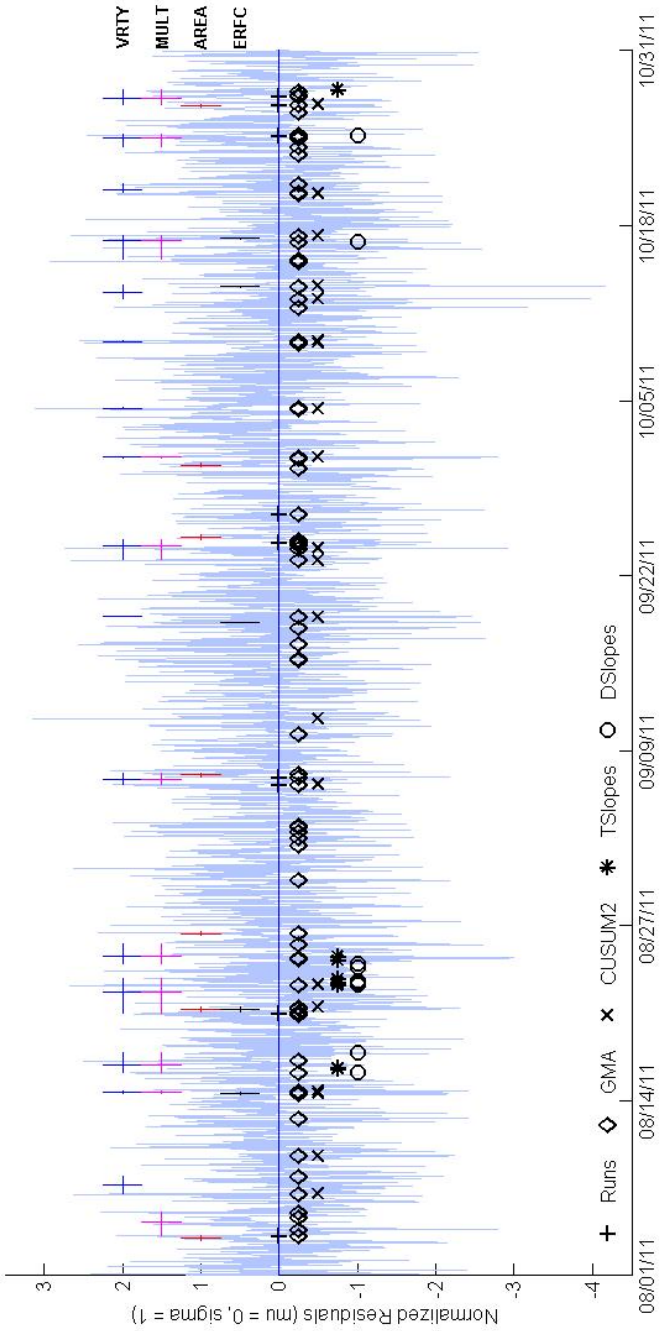

Figure 5.4.: Normalised ^{54}Mn hourly count rate recorded from August - October 2011. Superimposed below the horizontal axis in black are the hits triggered by each statistical test. In color, above the horizontal axis, are positions of aggregated decay flags VRTY, MULT, AREA, ERFC indicating areas of statistically relevant anomalous activity in the signal.

6. Correlation Analysis

6.1 Correlation to Solar Activity

As the minimum of Solar Cycle 23 came to a close, 2010 saw the beginning of Solar Cycle 24, which has proven to be a fairly inactive cycle compared to previous years. The following results are obtained from analysing ^{54}Mn data during the 2 year period from January 3, 2010 - December 30, 2011 coincident with the rise in Sunspot activity as Cycle 24 begins. After the filtering process, there were 239 decay flags produced by the *Changemaster* detection algorithm and the next step in this investigation will be to compare the decay flags with activity recorded from the Sun.

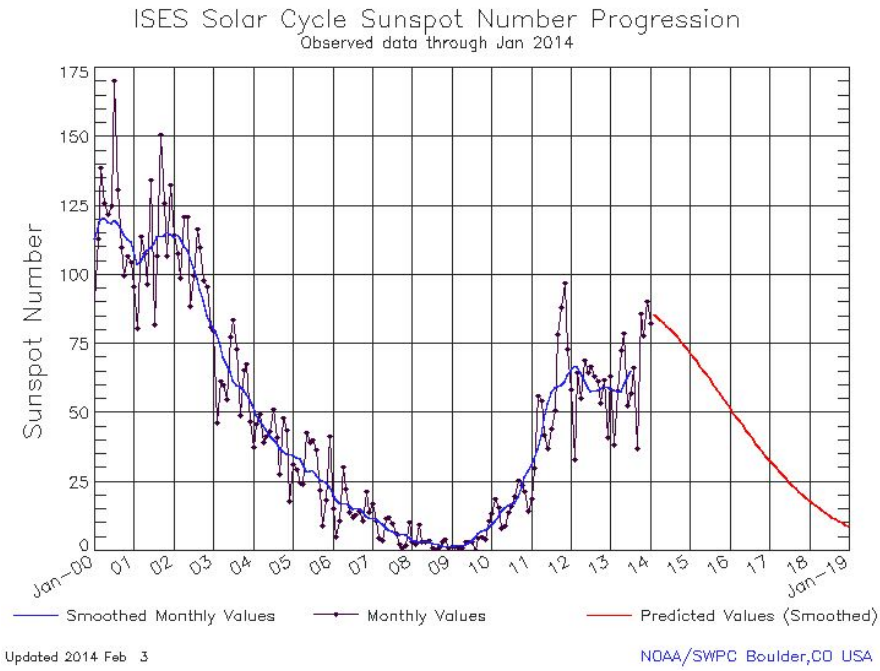

Figure 6.1.: Solar Cycle 24 Sunspot number progression. The 11-year solar cycle can be clearly seen with a minimum in observed Sunspots occurring during 2009. The vertical lines denote January 1 of the indicated year. Courtesy SWPC, NOAA.

Figure 6.2 gives a visual comparison of the distribution of the decay flags produced from Purdue ^{54}Mn data between January 3, 2010 and December 30, 2011, against occurrences of high-level solar activity index alerts reported during that period. The solar event distribution is constructed from daily activity reports published by NOAA . Figure 6.2 graphs the alerts associated with the strongest levels of flare activity for FLA, RBR, RSP and XRA indices, which are direct measures of flare strength. Specifically, our search is focused on x-ray flares of strength M-class (associated with peak flux emissions $\geq 10^{-5}$ Wm^{-2}) and higher and the equivalently powerful radio storms which accompany them; Table 6.1 lists the cut-off thresholds used to filter the more energetic events. This reduces the number of issued warnings from 12033 to 413 alerts which, in cases of strong flare eruptions, overlap in time. Particulars about the activity of each index are detailed in Sec. 3.5.4. We note the presence of regions where there are no solar event alerts and, correspondingly, no decay flags either.

Table 6.1: Four solar indices issued by NOAA which are direct measures of flare strength during solar eruptions. These thresholds filter out small scale storms, focusing on flare strengths of M-class and higher.

Index	Threshold
FLA	Importance ≥ 2 & Brightness $\geq$ N
RBR	Peak value ≥ 1000 flux units
RSP	Major Intensity
XRA	M-class or higher

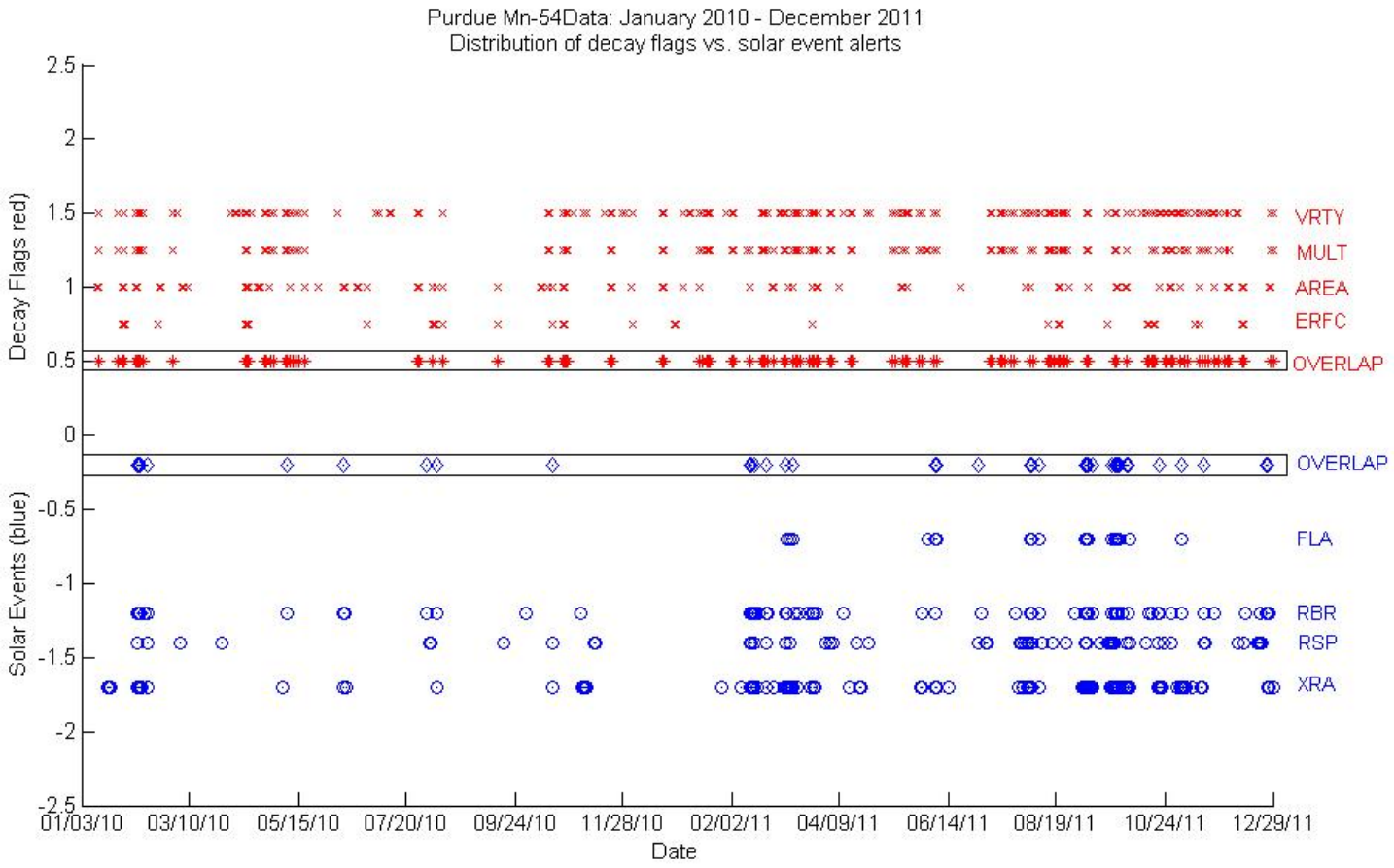

Figure 6.2.: Distribution of Purdue ^{54}Mn decay flags and solar events from January 3, 2010 through December 30, 2011. Decay flags are listed in red from top to bottom: VRTY , MULT , AREA , ERFC . The red stars indicate regions where two or more decay flags overlap. In blue from bottom to top are the solar indices: XRA, RSP , RBR , FLA . The blue diamonds indicate regions where more than one type of index is issued. We note the presence of regions where there is an absence of both solar event alerts as well as decay flags.

To test for possible correlations between fluctuations in nuclear decay rates and energetic solar activity, we compare the distributions of decay flags and solar indices shown in Fig. 6.2. The following results are obtained using a 48 hour window of coincidence. Table 6.2 lists the fraction of each solar event type that was preceded within 48 hours by each type of decay flag (SPD). Of particular note is the ANY-ALL value which calculates a cumulative comparison between the two data sets. We see from Table 6.2 that 49.2% of all indices indicative of strong flare activity were preceded by some form of decay rate fluctuation in the ^{54}Mn sample. Specifically, considering the development of some form of alert system for potentially dangerous flare eruptions, we see that for XRA events, 48.9% of all M-class and higher x-ray flares during 2010 and 2011 were associated with some deviation in ^{54}Mn decay rates 48 hours prior to their occurrence. Table 6.3 lists the fraction of each decay flag type that was followed within 48 hours by each solar index (DFS). We find that 37.2% of all decay flags identifying regions of significant variations in decay rate were followed (within 48 hours) by a warning report issued by NOAA.

Table 6.2: Fraction of Solar events preceded by a decay flag within 48 hours (SPD). Results are obtained from comparison of distributions from 2010-2011. The ANY-ALL entry indicates an overall 49.2% of the 413 strongest flare alerts issued were preceded by a decay flag identifying variations in the ^{54}Mn decay rate.

TYPE	VRTY	MULT	AREA	ERFC	**ANY**	# Events
FLA	0.500	0.563	0.375	0.000	0.625	16
RBR	0.345	0.415	0.316	0.070	0.509	171
RSP	0.253	0.172	0.195	0.115	0.437	87
XRA	0.396	0.367	0.252	0.036	0.489	139
ALL	0.349	0.354	0.271	0.065	**0.492**	413

Table 6.3: Fraction of decay flags followed by a solar index warning within 48 hours (DFS). Results are obtained from comparison of distributions taken from 2010-2011. The ANY-ALL entry shows that 37.2% of the 239 decay flags identified by *Changemaster* were indeed followed by NOAA flare alerts.

TYPE	FLA	RBR	RSP	XRA	**ANY**	# Flags
VRTY	0.065	0.204	0.151	0.215	0.376	93
MULT	0.117	0.267	0.150	0.283	0.433	60
AREA	0.079	0.254	0.127	0.254	0.333	63
ERFC	0.000	0.217	0.087	0.130	0.304	23
ALL	0.075	0.234	0.138	0.234	**0.372**	239

6.1.1 Computational Checks

Next we address the question of whether these values could simply be the result of random coincidences. Modeling such a scenario, we calculate the expected or average rate that a decay flag will precede a solar alert by considering the cumulative percentage of 48 hour intervals preceding each alert ϕ_s over the entire range of data, where care has been taken to avoid overlapping intervals. Thus, the event frequency window ϕ_s is defined as

$$\phi_s = \frac{\text{aggregate of 48 hour intervals prior to every solar event}}{\text{entire interval}} \tag{6.1}$$

Then, given a certain number of decay flags f_d, we would expect to find $f_d \times \phi_s$ flags to fall randomly within a 48 hour window prior to an alert. Hence, assuming variations in decay rates are uncorrelated to solar activity, Table 6.4 lists the average rates of coincidence between the them. The average SPD and DFS rates based on Eq. (6.1) are 34.1% and 28.1% respectively; in both cases lower than the actual experimental values of correlation calculated above.

Table 6.4: Expected fractions of coincidence between decay flags and solar events assuming no correlation between them. The expected fraction of solar events randomly preceded by decay flags is 34.1%. The fraction of flags randomly followed by an alert within 48 hours is 28.1%. These are both lower than the actual SPD and DFS values which are 49.2% and 37.2% respectively.

TYPE	VRTY	MULT	AREA	ERFC	ANY
Average SPD	0.251	0.161	0.158	0.061	**0.341**

TYPE	FLA	RBR	RSP	XRA	ANY
Average DFS	0.035	0.140	0.128	0.159	**0.281**

As a second test, we introduce a shuffling procedure to test the significance of the results listed in Tables 6.2 and 6.3. Each data point in the set of normalised decay measurements $\{x(t_i)\}$ is randomly assigned to a different time bin leading to the construction of a new shuffled data set $\{r(t_i)\}$. The shuffling of decay data suppresses any intrinsic fluctuations or trends in the measured count rate should they exist. This data set is subsequently processed by the same signal detection algorithms, calculating new values for the SPD and DFS fractions. For a set of 10,000 randomized trials, the resulting ANY-ALL values are plotted in Figs. 6.3 and 6.4. The mean DFS value obtained from these trials indicates that only 28.4% of randomly generated decay flags would be followed by any solar event compared to the 37.2% obtained from the actual measured data. Thus, the experimental DFS test produces results that are 2.8 standard deviations above the random mean. Similarly, the SPD histogram in Fig. 6.4 shows the average number of solar events preceded by decay flags is 42.2% while the experimental result (49.2%) is 0.9 standard deviations away from this mean.

The "pac-T" test was developed as a third check to test the significance of the SPD and DFS values obtained from the experimental data. This test preserves the normalised residuals, while the time bins are cyclically permuted in 6 hour increments over the entire 2 year interval. With each time shift, the new data set $\{x(t_{i+6p})\}$, where

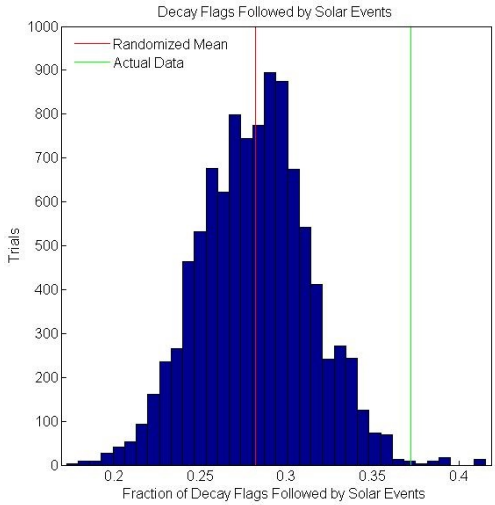

Figure 6.3.: Results from 10,000 shuffle tests for the DFS fraction. Randomized mean and standard deviation are found to be 0.282 and 0.0324 respectively. The actual results are thus statistically more significant than the randomized results by 2.79σ.

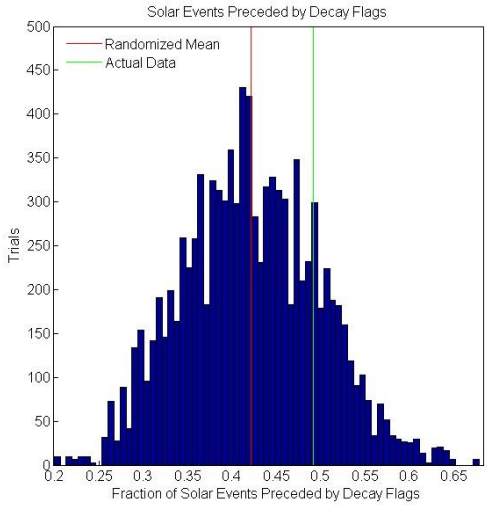

Figure 6.4.: Results from 10,000 shuffle tests for the SPD fraction. Randomized mean and standard deviation are found to be 0.422 and 0.0773 respectively. The actual results are thus statistically more significant than the randomized results by 0.91σ.

p is an integer, produces a set of decay flags whose flag times are similarly adjusted. This flag distribution is then compared to the solar event list, and a new level of correlation is calculated. The pac-T test preserves the grouped nature of the decay flags and allows us to the investigate any connection with periods of solar inactivity as well.

Figure 6.5 depicts the SPD correlation results for the entire two year period. The average SPD value for the entire cyclic permutation is found to be 35.2%. We find that 96.9% of all the SPD values calculated for each time-shift are lower than the actual SPD value obtained from the experimental data (49.2%).

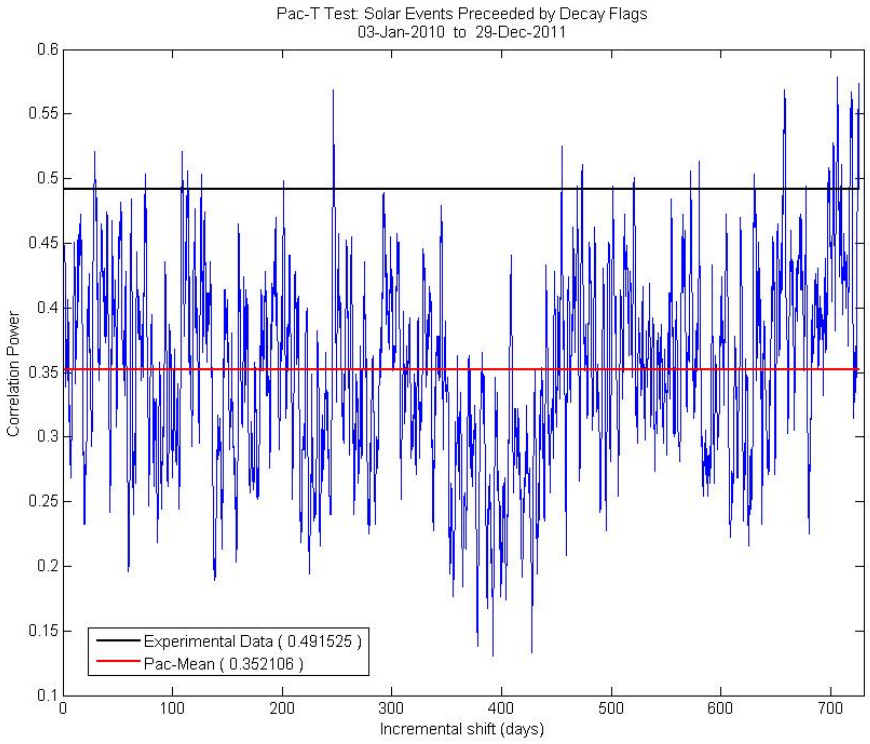

Figure 6.5.: Results of the SPD pac-T test for ^{54}Mn data from January 2010 to December 2011. For a cyclic 6 hour time shift in data, the average SPD value is 35.2% compared to 49.2% for the actual measured data. Since 96.9% of the cyclically permuted SPD correlations are smaller than those arising from the experimental data, the results of the pac-T test are significant at the 1.8 σ level.

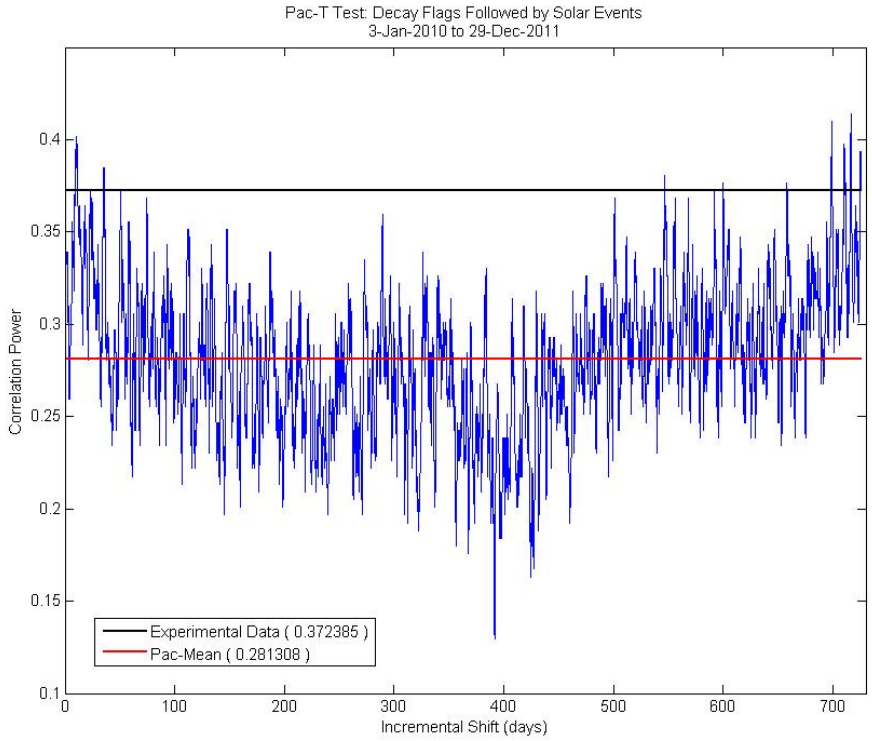

Figure 6.6.: Results of the DFS pac-T test for ^{54}Mn from January 2010 to December 2011. Data are cyclically permuted in 6 hour increments. The average DFS value obtained from time shifted data is 28.1% compared to 37.2% from actual experimental data. The results of the pac-T test are significant to the 2.3 σ level since 98.4% of the permuted DFS correlations are smaller than the actual data.

Similarly, Fig. 6.6 depicts the results of the time shifted DFS values. The average permuted value calculated is 28.1%, with 98.4% of all DFS values calculated from the pac-T test occurring lower than the actual 37.2%. Thus, the mean SPD and DFS results produced by the pac-T test are significant at the 1.8 σ and 2.3 σ levels respectively.

6.1.2 Negative Findings

Prompted by the original paper by Jenkins et al. [14] which presented evidence for a connection between decay perturbations and heightened solar flare activity, some searches have reported a failure to observe such an effect during other solar events. One such case is by Parkhomov who employed two G-M counters to study the disintegrations from samples of ^{90}Sr and ^{60}Co, and a silicon detector that monitored ^{239}Pu [52]. Since solar storms are generally short-lived, typically on the time-scale of several minutes to a few hours, our experience indicates that decay data should ideally be acquired no less frequently than hourly. This condition is necessary in order to resolve any relevant signals from the decay data when comparing to flare occurrences. Thus, his claim for the absence of a connection between solar flares and decay rates can be understood in this way. As can be seen by Table 1 in Ref. [52], due to the "low count rate from (their) installation" data were aggregated in bins ranging from 17-23 hours which is too long to resolve effects from short-lived flares. Also, in Ref. [53], Parkhomov did claim to see evidence for an annual modulation in several β-decaying isotopes. The author reported 1 year periodicities in ^{3}H, ^{32}Si, ^{36}Cl, ^{56}Mn, ^{60}Co, ^{90}Sr, ^{137}Cs and decay products of ^{226}Ra with amplitudes from 0.1 - 0.35% from the average count rate with *phases*[1] occurring between January and March.

Another negative claim appears in the work of Belotti et al. in Ref. [54] who studied samples of ^{137}Cs, ^{40}K and ^{nat}Th for variations in count rate coincident with two X-class flares in 2011 and 2012. To begin with, while Ge and NaI detectors were measuring ^{137}Cs and ^{40}K sources at Gran Sasso, the Sun erupted in an X5.4 strength flare on March 7, 2012. Belotti et al. reported "no significant dip or excess in correspondence with the x-ray main peak". However, a region of perturbation in the ^{54}Mn decay rate coincident in time is identified by our algorithms, as is evidenced in Fig. 6.7. Between March 6-13 there is a clear grouping of decay flags, and the lack

[1]The *phase* of a sinusoidal signal denotes the calender day during the year when the observed count rate is a maximum.

of flag production on either side of this interval supports the presence of a significant association with heightened solar activity.

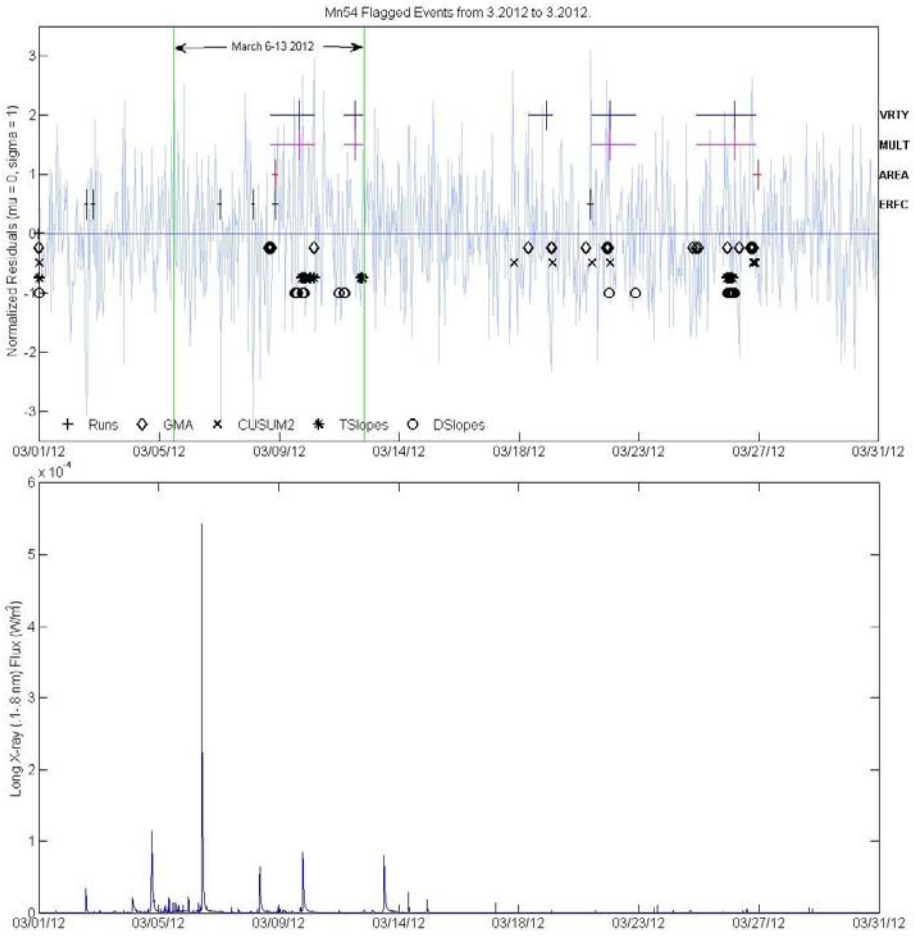

Figure 6.7.: ^{54}Mn data analysed over March 2012. NOAA issued an alert for an X5.4 flare on 7 March 2012. The associated sunspot remained active until March 13 with the eruption of an M-class flare. During March 6-13 we find a grouping of decay flags coincident in time with the heightened solar activity.

In 2011, Bellotti et al. reported a failure to see deviations in measurements of ^{137}Cs and ^{nat}Th coincident in time with an X6.9 flare on August 9 at 8:08 UTC. While our detection system produces only a minimal response on August 9, a considerable effect is seen during August 3-5. It is interesting to note that Sunspot 11263, which

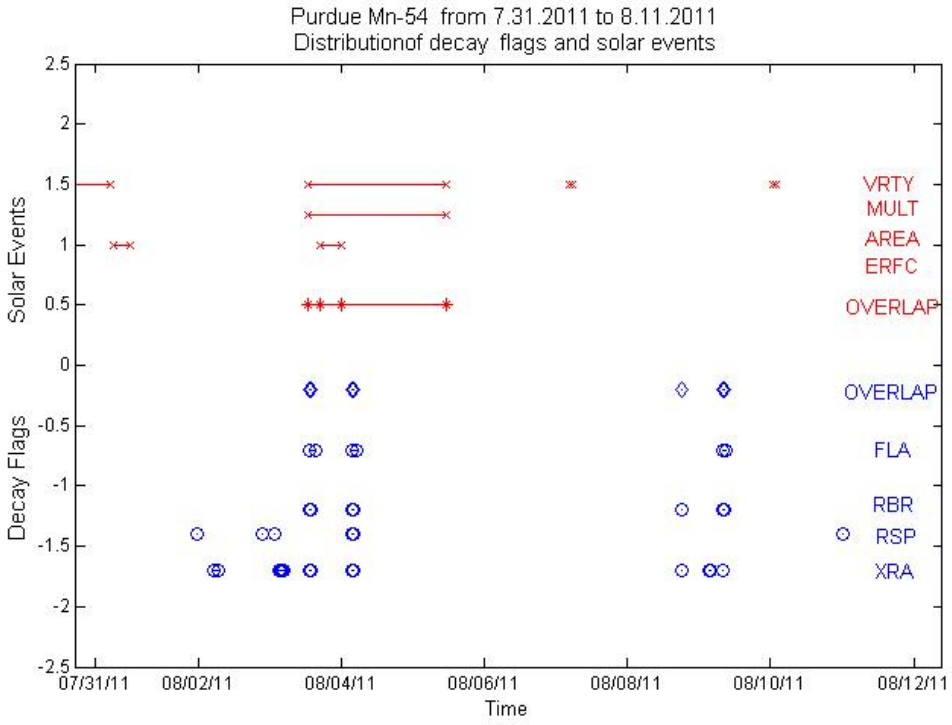

Figure 6.8.: Distribution of Solar events (blue) and ^{54}Mn decay flags (red) for August 2011. Although the decay data fail to show significant perturbations on August 9$^{\text{th}}$ following the X6.9 flare, several decay flags are issued on August 3-5 in conjunction with several M class flares originating from the same Sunspot 11263 a few days earlier, as well as an M9.3 flare from the neighboring spot 11261.

produced the X-class flare on August 9, was already fairly active with several M-class storms in conjunction with an M9.3 strength eruption from the nearby Sunspot 11261 during that interval. Figure 6.8 depicts the results of our analysis on ^{54}Mn for the beginning of August 2011 along with the list of flare alerts issued by NOAA during the same period.

Of particular note is that although the X6.9 flare is stronger on the x-ray scale with peak flux $> 10^{-4}$ Wm^{-2}, it was the M9.1 flare on August 5$^{\text{th}}$ that produced a

larger proton event which peaked at 96 pfu[2]. The X-class flare produced a smaller proton shower with a peak flux of 26 pfu. Similarly, The X5.4 flare on March 7, 2012 was followed by a very intense proton event that peaked at 6530 pfu. It is clear from our examination of the NOAA data, that solar storms are not all identical in terms of the effects we observe on Earth, and hence it is not surprising that different storms may register more prominently in different combinations of the 15 NOAA indices.

[2]Proton fluxes are integral 5-minute averages for energies > 10 MeV, given in Particle Flux Units (pfu), measured by GOES spacecraft at Geosynchronous orbit: 1 pfu = 1 p cm^{-2} sr^{-1} s^{-1}.

7. Discussion

7.1 Multiple Decay Sites

To increase the robustness of our signal detection system, *Changemaster* , it is our intention to combine data signals from multiple decay sites positioned at various geographical locations. Data from multiple sites will be analysed in parallel by *Changemaster* and the resulting decay flags from each site will have to pass further filtering criteria. The increased statistics will help single out regions of truly anomalous activity that are shared among decaying isotopes from multiple locations, weeding out flags that are the products of systematic or environmental influences specific to any one experiment. To illustrate the significant improvement that can be realised by combining data from several decay sites, we analysed 10 sets of simulated data, where each set represents an individual site.

The simulated data $N(t)$ were created by assuming a monotonically decreasing exponential function for a two year period. A regularly spaced spike, at a frequency of 12 yr^{-1}, was introduced to mimic an atypical response in the data to heightened solar activity. Random noise with a $\sqrt{N}$ standard deviation was incorporated to reflect the stochastic nature of nuclear decay. Each set of simulated data is then independently analysed by the signal detection algorithms, and Fig. 7.1 illustrates the results from a single site. Decay flag distributions from each of the 10 sites were compared, and aggregated flags were produced when a filtering condition was satisfied: if 75% or greater of all sites produced a flag of the same type, i.e. VRTY, MULT, AREA, or ERFC, within a prescribed time interval then that flag is retained as a successful indicator of fluctuations in the signal. Figure 7.2 shows the results of the combined 10 sites. The combined data are calculated by normalising the averaged simulated data from all 10 sites. Superimposed in color are the surviving 4 types of decay flags. Flags

that occur within a 24 hour period surrounding the induced peak plus one additional day are considered successful in identifying the regions of anomalous activity. From a single site, we find that only 13% of flags occur within the 48 hour period beginning at the start of each peak, whereas after the filtering criterion is applied to 10 sites, 63% of the surviving flags fall within this interval. In this manner, the effect that analysing multiple sites will have on the robustness of our signal detection algorithms is evidenced by the reduction in false positive rate from 87% for 1 site down to 37% for 10 sites. Additionally, the figures clearly show that while a single site analysis is not particularly helpful in discerning the induced monthly spike, a 10 site comparison generates flags at a clear monthly rate with noticeable spikes in the normalised data.

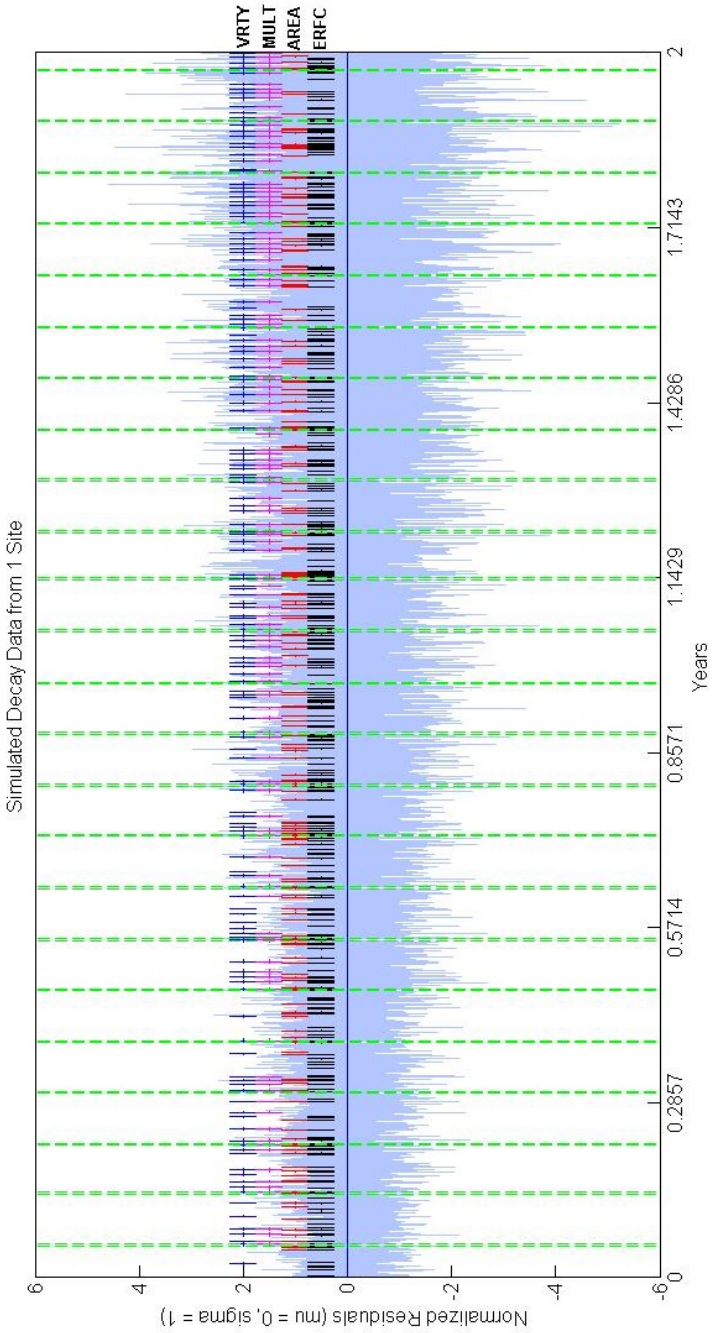

Figure 7.1.: Simulated decay data for 1 site. Data describe a decaying exponential over 2 years. The green dashed lines identify regions of heightened activity, introduced at a frequency of 12 yr^{-1}, along with a spread of random noise. 13% of flags occur in a 48 hour period beginning at the start of each peak. The false positive rate is considerably high at 87%.

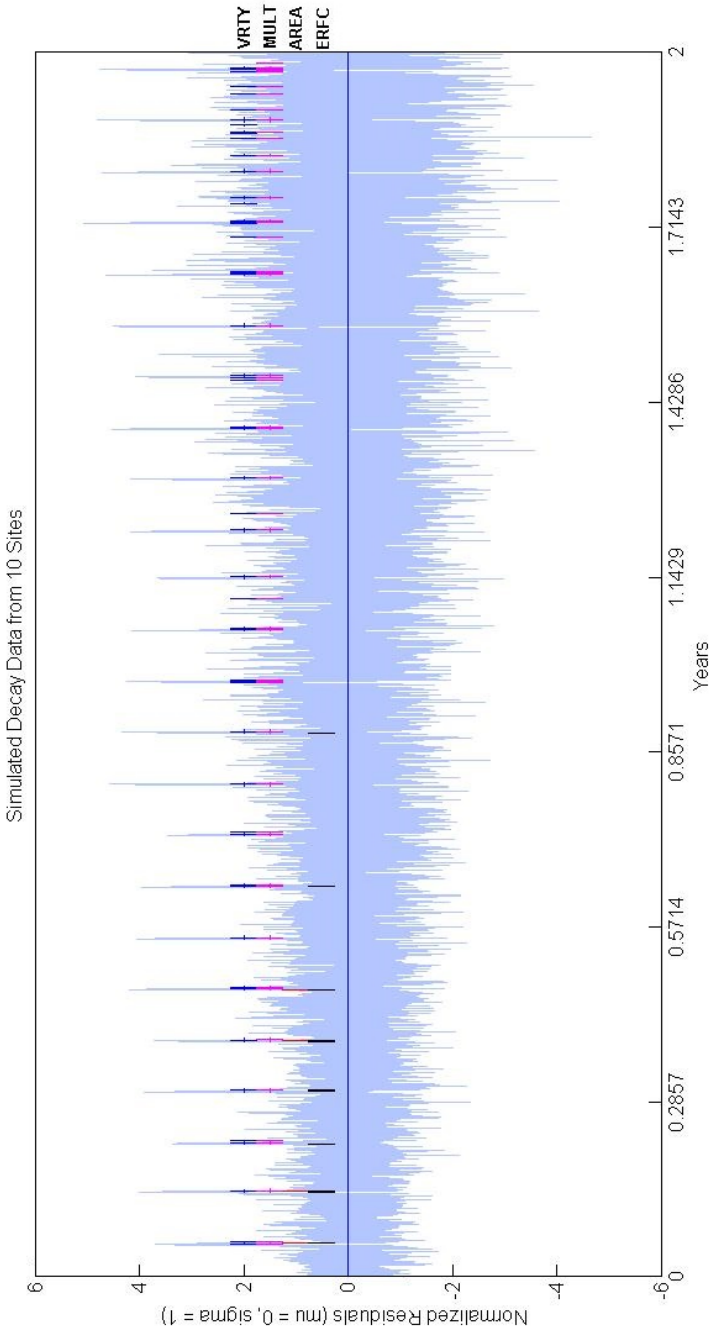

Figure 7.2.: Averaged simulated decay data, with identical periods of heightened activity, from 10 sites over 2 years. The aggregated decay flags from a 10 site comparison clearly picks out the monthly spike generated in each of the simulated data sets. After the filtering criterion is applied, 63% of the surviving flags fall within a 48 hour period beginning at the start of each peak.

7.2 Conclusions & Remarks

This work was motivated by the numerous recent reports of anomalies detected in decaying radioactive isotopes using a variety of different detector set-ups in several different regions [5,9,55,56]. In Chapter 2, detailed investigations of measurements of ^{32}Si /^{36}Cl at BNL and ^{226}Ra at PTB showed annual periodicities with amplitudes of $\sim 0.15\%$ that could not entirely be attributed to systematic or environmental factors. Additional power spectrum analyses of these data sets corroborated these findings in Refs. [11, 24]. These frequencies are presumably related to the annual variation in the Earth-Sun distance, sub-annual periodicities which may be related to solar rotation [24] and a Rieger-like period at 2.11 yr^{-1} [12]. A discussion of how a novel interaction between $\beta-$decaying isotopes and neutrino or neutrino-like particles could affect $\beta-$decay rates is explored in Appendix B. However, the detailed mechanism for such an interaction is as yet unknown. The results presented by Jenkins et al. [14], which uncovered short-lived anomalies in ^{54}Mn count rates concomitant with an X-class solar flare, prompted the question of whether this seeming correlation between decay rates and short-term but highly energetic solar events was a simple coincidence or an instance of a broader interaction with the capability for prediction. To answer this question, we developed a series of unique signal-detection algorithms to analyse several years of ^{54}Mn decay data and identify regions of statistically significant fluctuations. Chapter 6 details the results of this analysis: within a 48 hr window, 49.2% of solar events indicative of strong flare activity were preceded by some form of fluctuation in the ^{54}Mn decay rate, while 37.2% of all decay flags were followed (within 48 hours) by a warning report issued by NOAA .

The results of each of the tests detailed in Sec. 6.1.1 strongly support the claim that the level of correlation found between perturbations in the decay rate of ^{54}Mn and patterns of surface flare activity could not simply arise from random coincidence. A shuffling procedure, where the residuals of the recorded measurements were shuffled in time during 10,000 randomized trials, showed that the SPD correlations are signifi-

cant at the 0.9 σ level, while the DFS events are significant at the 2.8 σ level. Neither the random expected rate of flag correlation for a specific distribution of solar events, nor shifting the decay flag distribution incrementally in time, were able to generate results at the level seen in the actual experimental data.

Although measurements on the Purdue ^{54}Mn sample were taken up to the beginning of 2013, the increased fractional uncertainty and subsequently higher number of false positives that occurred during the more recent recordings prompted focusing our analysis on data taken during 2010 and 2011. To start with, assuming an expected rate of decay, the count rate of the ^{54}Mn sample at the end of the two year run would be given by

$$\frac{N(t_1 = 2 \text{ years})}{N(t_0 = 0)} = \exp(-\lambda(t_1 - t_0)) \tag{7.1}$$

Thus, the count rate at the end of 2 years is only $\approx 20\%$ of what it was initially, which means that the $\sqrt{N}$ random fluctuations would have been almost 2.2 times larger. To counteract this effect in an actual detection system, new samples would necessarily be inserted into detectors on a frequent basis to maintain an appropriately high count rate.

Additionally, in an actual system, even with a fresh sample the $\sqrt{N}$ fluctuations from a single sample are still a problem, but one which can be readily overcome by the addition of on-line sites. The results of a simulated multi-site analysis motivated the construction of several new experiments:

(i) Samples of ^{54}Mn are monitored in Santiago, Chile. The unique location of this experiment in the Southern hemisphere, offers an excellent opportunity to test whether the annual periodicities seen in decaying isotopes are influenced by seasonal changes.

(ii) Khalifa University in Abu Dhabi, U.A.E. A nuclear physics group at Khalifa University plans to run extended campaigns on the investigation into this phenomenon. With current crystal NaI detectors recording data on ^{60}Co and ^{54}Mn

sources, they plan to add scintillation detection of ^{90}Sr to their set-up, with the possibility of additional sources and detectors. The geographic location and climate of U.A.E would provide insight into any effect that a phase shift associated with the Earth's rotation, seasonal, or day-night changes in temperature might have on the decay rate.

(iii) Oak Ridge National Laboratory (ORNL), TN. The experiment at ORNL monitors several isotopes exhibiting both beta and alpha decay structures: ^{241}Am,^{60}Co, ^{152}Eu, and ^{22}Na, and will expand to include 8 NaI and hpGe detectors, as well as, additional sources. The current apparatus, housed in a 4" thick lead cave, sits approximately 7 m from the core of the nuclear reactor. The group conducting this experiment is addressing the question of whether the $\bar{\nu_e}$ flux from the 85 MW High Flux Isotope Reactor (HFIR) can affect the rates of nuclear decays.

Finally, as was seen in Sec. 6.1.2, we note that it is not necessarily the case that the strongest storms (measured by various combinations of NOAA indices) must produce the largest signals in decay data. We see evidence for this in Tables 6.2 and 6.3, and indeed, the varying powers of correlation with different types of violent solar phenomenon may shed light on the nature of influence the Sun poses on decaying isotopes. In addition to the indices listed in Table 6.1, Fig. 7.3 lists the (non-trivial) levels of correlation of solar events preceded by any type of decay flag (within 48 hr) for all the indices reported by NOAA . The values are calculated over the two year period from January 2010 to December 2011. We see that the highest correspondence is with FLA events which categorizes flares on the H_α scale according to the area of the eruptive site during maximum brightness. Furthermore, the location of the flaring Sunspot on the solar surface would supposedly have an effect if there is an anisotropy in the flux of neutrinos emitted. In future work we intend to explore this question in greater detail.

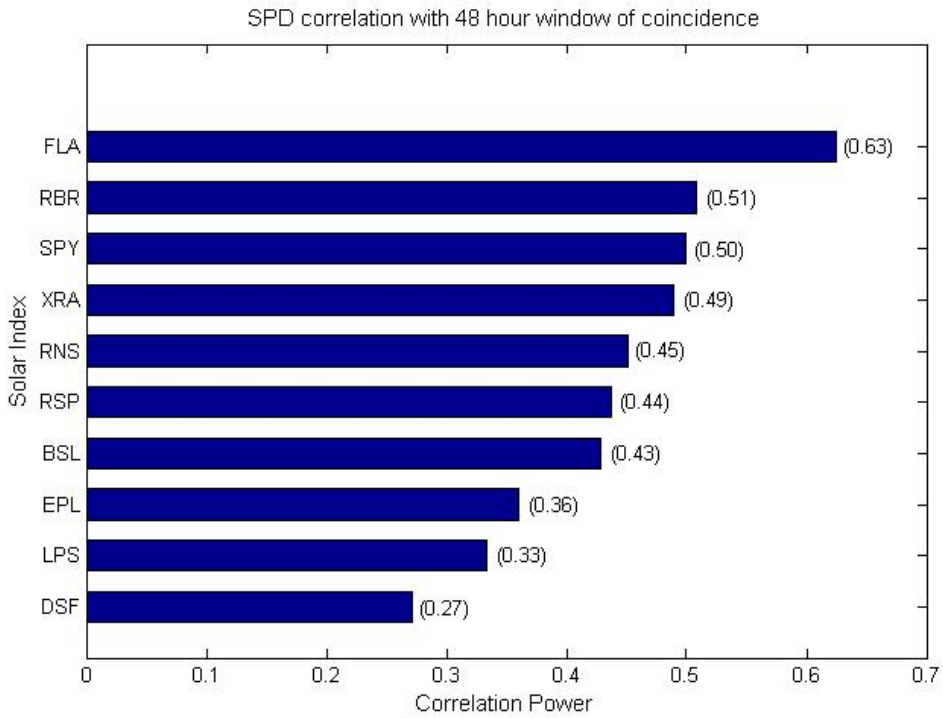

Figure 7.3.: Comparison of all (non-zero) NOAA indices that were preceded by any type of decay flag within a 48 hour window. These indices were compared to ^{54}Mn decay data over the 2 year period from January 2010 to December 2011.

APPENDICES

A. Isotope Decay Schematic

A.1 ^{32}Si via β^- decay

^{32}Si is the longest-lived radioisotope of silicon with a half-life of 153(19) yr. ^{32}Si decays via β^- decay into the daughter ^{32}P, which has a half-life 14.3 d which in-turn decays to the ground state of ^{32}S. During the 224 keV disintegration, a β^- particle and an anti neutrino $\bar{\nu}$ are ejected.

$$^{32}\mathrm{Si} \longrightarrow {}^{32}\mathrm{P} + \bar{\nu} + \beta^- \tag{A.1.1}$$

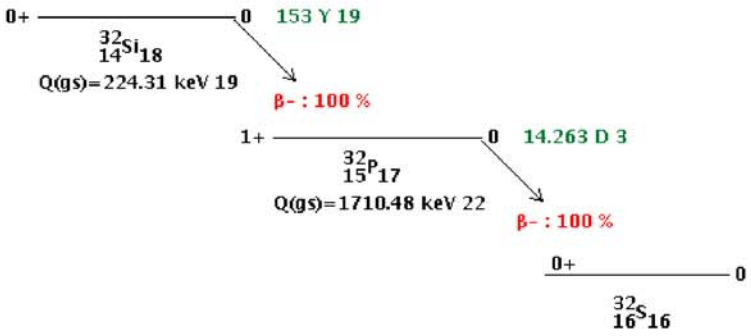

Figure A.1.: Beta Decay of ^{32}Si . ^{32}Si decays by β^- to ^{32}P which then decays 100% by beta emission to the ground state of ^{32}Si .

A.2 ^{226}Ra via alpha decay

^{226}Ra is the longest-lived isotope of radium with $T_{\frac{1}{2}} = 1600(7)$ yr. Because of its long half-life, it was used as the control element during the PTB experiment. ^{226}Ra itself decays via the emission of an alpha particle to ^{222}Rn. However, there are several daughters that decay through β^- decay and almost all remain in equilibrium with the initial ^{226}Ra concentration. The somewhat complex decay chain for

^{226}Ra is given in following figure, where decays to the right represent alpha emissions while decay branches to the left indicate β^- disintegrations.[1]

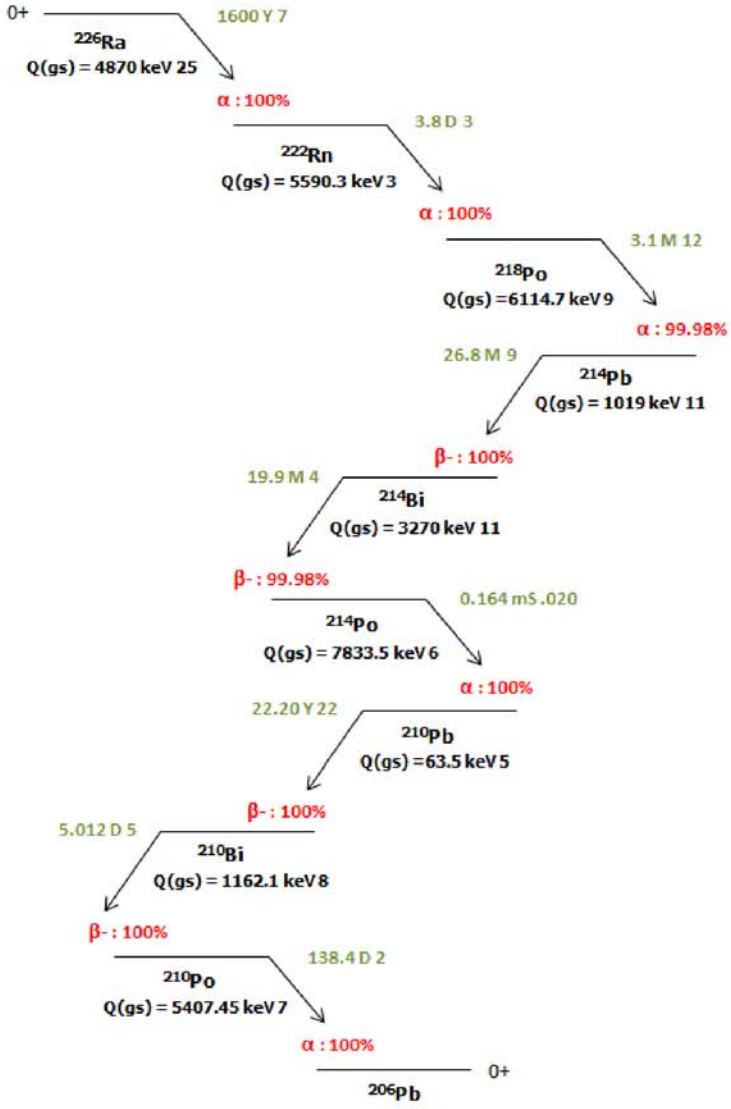

Figure A.2.: ^{226}Ra decay chain. The decays of interest are noted with α decays directed to the right and β^- decays proceed leftwards. The concentration of daughter production are almost entirely in equilibrium with the parent ^{226}Ra .

[1]Figure (A.2) does not list all possible modes of decay. Only the decay evolution of interest is shown.

A.3 ^{54}Mn via K-capture

^{54}Mn is a relatively short-lived isotope with a half-life of 312.05(4) d and decays only through K-capture (Q_{gs} = 1377(10) keV) to an excited state of ^{54}Cr. The daughter nucleus then de-excites to its ground state, accounting for the energy transferred.

$$^{54}\mathrm{Mn} + e \longrightarrow {}^{54}\mathrm{Cr} + \nu \tag{A.3.1}$$

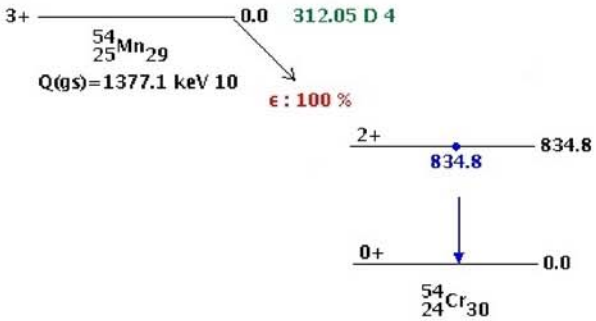

Figure A.3.: Beta Decay of ^{54}Mn . ^{54}Mn decays by K-capture to ^{54}Cr emitting an electron neutrino in the process.

B. Perturbation of β decay rates

Findings obtained from PTB, BNL, and Purdue investigations discussed in previous sections, indicate that the nuclear decay processes occurring during the experiments do not strictly follow the simple exponential decay law prescribed by theory, a discrepancy which cannot be attributed solely to systematic or environmentally induced errors. In this section we attempt to outline possible interaction mechanisms which may explain the phenomenology behind these findings.

In general, the modification to decay rates has been well documented in literature. Research conducted by Emery [57] discussed changes recorded in electron capture rates– a process that involves the coupling between atomic electrons surrounding the inner core and the nucleus. It was noted that the introduction of a suitable chemical environment can cause a redistribution of the atomic electron configuration, altering the electron overlap densities with the nucleus. Since the electron capture rate is proportional to $|\Psi(0)|^2$, where $\Psi(0)$ is the electron wave function at the nucleus [58], this can affect decay transitions by approximately 0.1%. In fact, Hensley et al. [59] published increases up to 0.6% in electron capture rates when subjected to intense high-pressure effects. Additionally, in 1983 Reiss proposed a formalism to describe modified β decay rates in the presence of very strong electromagnetic fields [60]. Motivation for investigating such an effect becomes clear when we recognise that even conventional β^+ and β^- decays, under no external field influences, experience transition rates modified due to the Coulomb interaction between the emitted β particle and nucleus. For the particular case of strong electromagnetic fields, Reiss supposed that the effective interaction between the emitted particle and the field would occur on a time scale smaller than the Heisenberg uncertainty time Δt_H of the decay event, if the intensity field parameter associated with β decay is sufficiently large. Here $\Delta t_H \sim \dfrac{\hbar}{M_W c^2} \sim 10^{-26} s$ where $M_W = 80.4$ GeV/c^2 is the mass of the $W^{\pm}$ boson. In the case of strong magnetic fields, Reiss predicts that field strengths of order 10^{12} G are required to produce a change of 0.1% in the rate of free neutron β^- decay rates. More recently, the deviation in decay rates was documented by Ohtsuki et al. who carried out an experiment measuring the electron capture rate of ^{7}Be in ^{7}Be doped C_{60} (^{7}Be@C_{60}), and ^{7}Be in Be-metal which was used as a reference compound [61].

The unique structure attributed to C_{60} – a fullerene forming a large spheroidal 'cage' of atoms, ensures that the electron density of C_{60} significantly alters the electron contact density with the ^{7}Be nuclei. They performed direct counting measurements on the two samples, of almost identical initial radioactivity, using a high-purity Ge detector under stringent experimental conditions. Ohtsuki et al. conclude that the half-lives obtained for ^{7}Be in ^{7}Be@C_{60}, and in Be-metal were 52.68(5) d and 53.12(5) d respectively, resulting in a 0.83% difference between their two samples. They attribute the unique electronic environment of the C_{60} cages as a possible explanation for the deviations observed in electron capture decay rates.

B.1 General Theoretical Framework

In recent work by our colleagues J. Buncher and J. Mattes, a model is outlined which may describe the coupling interaction experienced by decaying nuclei in the presence of an isotropic, homogeneous, spin-dependent field [62]. In doing so the authors find a possible alternate explanation to the puzzling negative neutrino mass range m_ν^2, obtained by numerous experimental groups trying to measure the neutrino mass, a phenomenon generally known as the ^{3}H endpoint anomaly. Recent experiments attempting to resolve the neutrino mass by direct measurement of the low energy spectrum produced by the β^- decay of tritium yield "negative values for the best fit value of m_ν^2" obtained from the resulting Kurie plot [63]. Before introducing an external field ϕ, to explain both the annual variations in decay rate and the negative m_ν^2 we summarize the simple case of a free neutron spontaneously disintegrating in the absence of any external field or influence [64] ($n \longrightarrow p + e^- + \bar{\nu}_e$). This weak neutron β^- decay is described by the Feynman diagram shown in Fig. B.1.

The differential transition rate $\frac{d\Gamma_o}{dE}$ describing the distribution of emitted electron energy E is given by [64]:

$$\frac{d\Gamma_o}{dE} = \frac{1}{(4\pi)^3\hbar c^2}\Big(\frac{g_w}{M_w c}\Big)^4 [\frac{1}{2}(m_n^2 - m_p^2 - m_e^2)c^2(E_+^2 - E_-^2) - \frac{2m_n}{3}(E_+^3 - E_-^3), \quad \text{(B.1.1)}$$

where $E_\pm$ is:

$$E_\pm = \frac{\frac{1}{2}(m_n^2 - m_p^2 + m_e^2)c^2 - m_n E}{m_n - E/c^2 \mp |\mathbf{p}|/c} \quad \text{(B.1.2)}$$

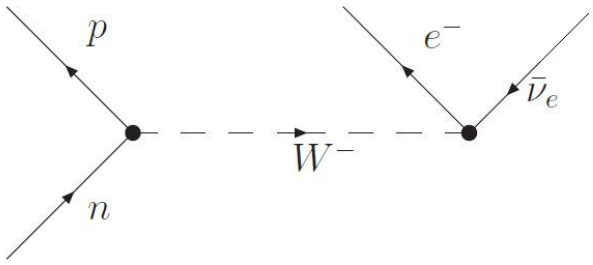

Figure B.1.: Feynman diagram describing neutron β^- decay. A neutron spontaneously decays via weak interaction into a proton and electron, emitting an electron antineutrino.

Here m_n, m_p, m_e are the mass of the neutron, proton, electron respectively and the neutrino mass is taken to be negligible. E, $\mathbf{p}$ describe the electron energy and vector-momentum. g_w is the weak coupling constant and M_w is the mass of the intermediate weak vector boson which can traditionally be expressed as the Fermi coupling constant $G_F \equiv \frac{\sqrt{2}}{8}\left(\frac{g_w}{M_w c^2}\right)^2 (\hbar c)^3$. At this stage it helps to simplify the above equations by setting $\hbar = c = 1$ and using of the following approximations:

$$\frac{m_n - m_p}{m_n} = 0.0014, \qquad \frac{m_e}{m_n} = 0.0005,$$
$$\frac{E}{m_n c^2} \ll 1, \qquad \frac{|\mathbf{p}|}{m_n c} \ll 1,$$

We can now expand Eq. (B.1.1) to the lowest order term to obtain:

$$\frac{d\Gamma_o}{dE} = \frac{1}{\pi^3}\left(\frac{g_w}{2M_w}\right)^4 E\sqrt{E^2 - m_e^2}[E_o - E]^2, \tag{B.1.3}$$

where $E_o \equiv m_n - m_p$ is the total energy available to the decay products. Specifically, for free neutron decay there is 782 keV available to the decay products after accounting for the electron rest mass; in comparison, tritium decay only has 18.6 keV available to distribute among its emitted decay particles due to the difference in parent and daughter nucleus masses. Buncher et al. find that this difference in available energy plays a pivotal role in how the transition rate of the decaying nucleus is affected by

an external potential [62]. The above expression describes the electron differential transition rate when emitted from a free decaying neutron for a given energy band. To obtain the total transition rate, or decay rate, we integrate Eq. (B.1.3) over energy E:

$$\Gamma_o = \frac{1}{4\pi^3}\Big(\frac{g_w}{2M_w}\Big)^4 m_e^5\Big[\frac{1}{15}(2E_o^4 - 9E_o^2 m_e^2 - 8m_e^4)\sqrt{E_o^2 - m_e^2} + E_o m_e^4 \ln(\frac{E_o - \sqrt{E_o^2 - m_e^2}}{m_e})\Big] \quad \text{(B.1.4)}$$

Now that the expression describing the decay rate for free neutron β^- decay has been established, the authors introduce an external static potential field ϕ which couples to the decay products with an interaction energy V. For definiteness, they assume the field interacts solely with the emitted antineutrino, and the Feynman diagram given earlier can be modified to reflect such a scenario is given in Fig. B.2.

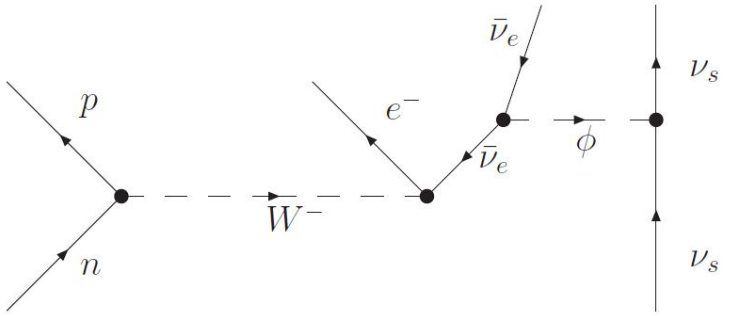

Figure B.2.: Feynman diagram describing modified β^- decay. There is an additional proposed interaction between the emitted antineutrino by neutron decay and a solar neutrino ν_s. [62]

For the interaction of a spin independent field ϕ, the energy spectrum available to the decay products experiences a shift and conservation of energy dictates $E + E_{\bar{\nu}} + V = E_o$. This shift $E_o \longrightarrow E_o - V$ alters the differential transition rate to:

$$\frac{d\Gamma}{dE} = \frac{1}{\pi^3}\Big(\frac{g_w}{2M_w}\Big)^4 E\sqrt{E^2 - m_e^2}[E_o - V - E]^2 \quad \text{(B.1.5)}$$

Equation (B.1.5) indicates that the sign of the interaction energy V can change the phase-space energy available, resulting in an increase or decrease in the overall

decay rate. Following the procedure used previously to calculate the total transition rate for free neutron decay, Eq. (B.1.4), the total decay rate for a parent nucleus affected by an interacting field ϕ can similarly be calculated by taking into account the change in overall energy available to the system. The limits of integration are adjusted so that the interaction energy V has an upper limit of $V < E_o - m_e$ which accounts for energy considerations in the decay process. Consequently we can solve for the change in differential transition rates $\Delta\Big(\frac{d\Gamma}{dE}\Big) = \frac{d\Gamma}{dE} - \frac{d\Gamma_o}{dE}$:

$$\Delta\Big(\frac{d\Gamma}{dE}\Big) = \frac{1}{\pi^3}\Big(\frac{g_w}{2M_w}\Big)^4 E\sqrt{E^2 - m_e^2}[(E_o - V - E)^2 - (E_o - E)^2] \quad \text{(B.1.6)}$$

$$= \frac{1}{\pi^3}\Big(\frac{g_w}{2M_w}\Big)^4 E\sqrt{E^2 - m_e^2}[-2V(E_o - E) + V^2] \quad \text{(B.1.7)}$$

The result above indicates that the fractional difference in decay rates, $\Delta\Big(\frac{\Gamma}{\Gamma_o}\Big)$ will be linear in V to the leading order. This means that decay processes which have a lower available energy E_o will experience greater changes in their fractional decay rates than those with a larger E_o range, for a given interaction energy $|V|$. Following this methodology we see that free neutron decay, which has $E_o - m_e \approx 782$ keV, requires an interaction energy $V = \pm 200$ eV to affect a $\pm 0.1\%$ change in its transition rate. In comparison, tritium decay ($E_o - m_e \approx 18.6$ keV) would require a much smaller interaction energy on the order of a few electron-volts, $V = \pm 5$ eV, to produce a change of similar magnitude in the transition rate describing its decay.

At this stage it is of some interest to consider the effect an isotropic, homogeneous but *spin-dependent* field would have on the transition rate describing β^- decays [62]. Since much effort has gone into investigating the influence of strong magnetic fields on $\beta-$decay rates [60] [65], this will allow us to reference an analogous scenario with the spin-dependent field ϕ_s. For simplicity, Buncher et al. discuss the simplifying case where an electron emitted during the decay process will couple to the constant magnetic field with interaction energy $V = -\vec{\mu}_e \cdot \vec{B}$. For an unpolarized sample, this can be approximated by assuming that half the sample experiences a positive effect while the rest experiences a negative effect, that is $V = -\vec{\mu}_e \cdot \vec{B} \longrightarrow V = \pm\mu_e B$. For such a scenario the expected value for the transition rate can be modeled as follows:

$$\langle \Gamma_s \rangle = \frac{1}{2}\Gamma(-|V|) + \frac{1}{2}\Gamma(+|V|)\,; \quad |V| < E_o - m_e \quad \text{(B.1.8)}$$

where $\Gamma(V)$ is given by,

$$\Gamma(V) = \int_{m_e}^{E_{max}} dE \frac{1}{\pi^3} \Big(\frac{g_w}{2M_w}\Big)^4 E\sqrt{E^2 - m_e^2}[E_o - V - E]^2, \tag{B.1.9}$$

The upper limit of integration is calculated assuming that the electron has maximum energy when emitted with its momentum p_e equal and opposite to that of the proton, and the antineutrino acquires no momentum, i.e. it is emitted at rest. This gives:

$$\begin{aligned} E_{max}(V) &= \sqrt{m_e^2 + p_{max}^2} && \text{(B.1.10)} \\ &= \frac{1}{2}\frac{m_e^2 + (m_P - V)^2 - m_D^2}{m_P - V} && \text{(B.1.11)} \end{aligned}$$

where m_P and m_D are the masses of the parent and daughter nuclei respectively. Following the procedures previously outlined, the authors show that the fractional change in decay rate $\Delta\Big(\frac{\langle\Gamma\rangle}{\Gamma_o}\Big) = \frac{\langle\Gamma\rangle - \Gamma_o}{\Gamma_o}$ has a leading term that is quadratic in V. Specifically, the change in the expected differential transition rate[1] is:

$$\begin{aligned} \Delta\Big\langle\frac{d\Gamma}{dE}\Big\rangle &= \Big\langle\frac{d\Gamma}{dE}\Big\rangle - \frac{d\Gamma_o}{dE} \\ &= \frac{1}{\pi^3}\Big(\frac{g_w}{2M_w}\Big)^4 E\sqrt{E^2 - m_e^2}[\frac{1}{2}(E_o - V - E)^2 + \frac{1}{2}(E_o + V - E)^2 - (Eo - E)^2] \\ &\approx \frac{1}{\pi^3}\Big(\frac{g_w}{2M_w}\Big)^4 E\sqrt{E^2 - m_e^2}V^2 \end{aligned} \tag{B.1.12}$$

The authors conclude that a spin-dependent field interaction produces a smaller fractional change to weak $\beta-$ decay rates compared to the spin-independent case discussed earlier. The reason for this difference can be attributed to the opposite changes to the transition rate caused by $+|V|$ and $-|V|$ which would largely cancel each other until " $V = +|V|$ decays would be significantly blocked" in the spin-dependent case. Thus, as $|V|$ increases they expect the simplistic treatment of spins in Eq. (B.1.8) to no longer hold. This result is reflected in the fractional change in decay rate $\Delta\Big(\frac{\langle\Gamma\rangle}{\Gamma_o}\Big)$ of free neutron decay which would now require an interaction energy of $|V|= 3.2$ keV to produce a 0.1% difference in its transition rate. Similarly, for tritium decay the interaction energy needed would now increase to $|V|= 280$ eV from 5 eV calculated in the spin-independent case.

[1]The differences in electron end point energies have been disregarded here.

The authors note an additional consequence of the spin-dependent field discussion in Ref. [62], particularly an alternate interpretation of the near end-point energy spectrum of tritium β^- decay that experimental results interpret as a negative squared neutrino mass ($m_\nu^2 < 0$) [62]. In tritium decay ($^3H \longrightarrow ^3 He + e^- + \bar{\nu}_e$), the emitted electron energy spectrum is described using the Kurie plot, $K(E)$:

$$K(E) \equiv \sqrt{\frac{d\Gamma}{dE}\frac{1}{E\sqrt{E^2 - m_e^2}}} \tag{B.1.13}$$

where the transition rate is taken to be the following, given the emitted neutrino has non-zero mass m_ν:

$$\frac{d\Gamma}{dE} = \frac{1}{\pi^3}\Big(\frac{g_w}{2M_w}\Big)^4 E\sqrt{E^2 - m_e^2}(E_o - E)\sqrt{(E_o - E)^2 - m_\nu^2} \tag{B.1.14}$$

For a sufficiently small neutrino mass the expression in Eq. (B.1.14) can be expanded in powers of $\Big(\frac{m_\nu}{E_o - E}\Big)^2$ which produces a leading term of the form:

$$\frac{d\Gamma}{dE} \approx \frac{1}{\pi^3}\Big(\frac{g_w}{2M_w}\Big)^4 E\sqrt{E^2 - m_e^2}[(E_o - E)^2 - \frac{1}{2}m_\nu^2] \tag{B.1.15}$$

Alternately the expected differential transition rate describing weak decays in a spin-dependent field is:

$$\Big\langle \frac{d\Gamma}{dE} \Big\rangle = \frac{1}{2}\frac{d\Gamma}{dE}\Big|_{V=-|V|} + \frac{1}{2}\frac{d\Gamma}{dE}\Big|_{V=+|V|} \tag{B.1.16}$$

$$= \begin{cases} \frac{1}{\pi^3}\Big(\frac{g_w}{2M_w}\Big)^4 E\sqrt{E^2 - m_e^2}[(E_o - E)^2 + V^2] & ;\ |V| \leq E_o - E \\ \frac{1}{2\pi^3}\Big(\frac{g_w}{2M_w}\Big)^4 E\sqrt{E^2 - m_e^2}[E_o + |V| - E]^2 & ;\ E_o - |V| < E \leq E_o + |V| \end{cases} \tag{B.1.17}$$

where we have accounted for the difference in electron end-point energies introduced by the particular sign of V. When $V^2 \ll (E_o - E)^2$, the influence of a spin-dependent field on $\beta-$decays can be compared to the tritium spectrum produced in the absence of an external field but with massive neutrinos emitted– i.e. $V^2 \cong -\frac{1}{2}m_\nu^2$. Consider for example, the results obtained by Stoeffl et al. [63] when studying the low-energy $\beta-$decay spectrum from a gaseous tritium source. Their data imply a negative best-fit value for the electron antineutrino mass squared $m_\nu^2 = -130$ eV^2. This result could now be interpreted as an interaction with a spin-dependent external field with interaction energy $|V| \approx 8$ eV. Buncher et al. publish a Kurie plot demonstrating how

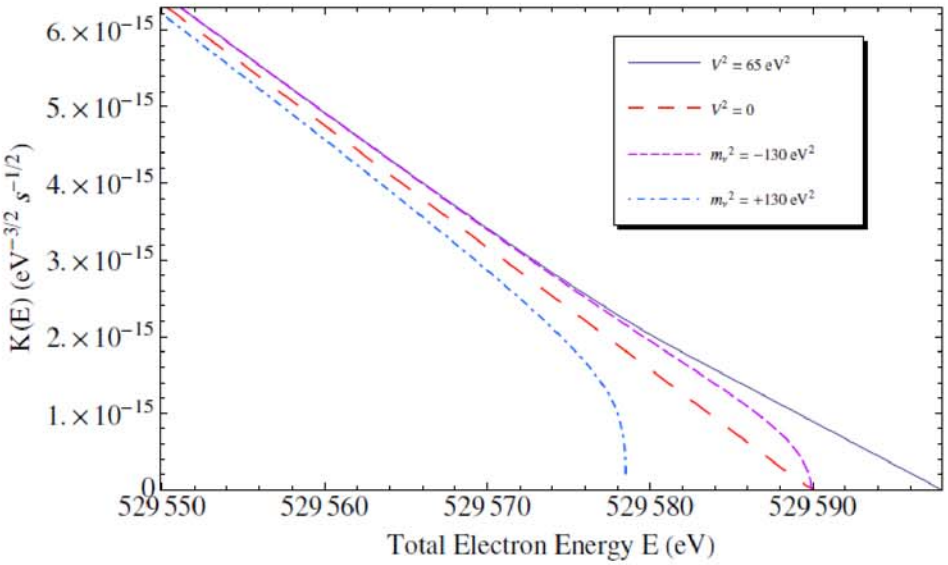

Figure B.3.: The Kurie plot for ^{3}H decay, demonstrating how a static, spatially constant and spin-dependent potential V produces a Kurie function which mimics the experimentally observed anomalous end-point behaviour. The red straight-dashed line is the Kurie function for $V^2 = 0$, $m_\nu^2 = 0$, and intersects the horizontal axis at E = $E_o \sim 529$ keV. The blue dotted-dashed curve is the Kurie function corresponding to Eq. (B.1.3) for $m_\nu^2 = +\ 130$ eV^2, while the purple dashed line is the Kurie function for Eq. (B.1.14) with $m_\nu^2 = -130$ eV^2. The solid line is the Kurie function for Eq. (B.1.17) with $V^2 = 65$ eV^2. [62]

their formalism describing the influence of an isotropic, homogeneous spin-dependent field could mimic the experimentally observed tritium end-point behaviour. Figure B.3 references the ^{3}H Kurie plots for $V^2 = 0$, $V^2 = 65$ eV^2, and $m_\nu^2 = \pm\ 130$ eV^2 [62]. The interaction of a spin-dependent field with the decay neutrino with an interaction energy of $V^2 \approx 65$ eV^2 could provide a possible explanation to the findings published by Stoeffl et al. and others. Though, the difference in behaviour of the two spectra at energies close to the end-point energy ($E - E_o \leq V^2$) should be noted. While the theorized framework predicts the electron spectrum should extend past the expected E_o by $\sim |V|$, the counting statistics are poor in this region and the difference may be difficult to resolve in practice.

LIST OF REFERENCES

LIST OF REFERENCES

[1] E. Rutherford, J. Chadwick, and C. Ellis. Radiations from radioactive substances. *Cambridge University Press*, 1951.

[2] E. Rutherford and J.E Petavel. The effect of high temperature on the activity of products of radium. *Abstract of the British Association Report*, pages 456–457, 1907.

[3] D.E Alburger, G. Harbottle, and E.F Norton. Half-life of si^{32}. *Earth and Planetary Science Letters*, 1986.

[4] H. Siegert, H. Schrader, and U Schotzig. Halflife measurments of europium and the long-term stability of detectors. *Appl. Radiat. Isot.*, 1998.

[5] J.M Nistor, J.M Heim, E. Fischbach, J.H Jenkins, and P.A Sturrock. Phenomenology of Rate-Related Nonlinear Effects in Nuclear Spectroscopy. *ArXiv e-prints*, 2014.

[6] E. D. Falkenberg. Radioactive decay caused by neutrinos? *Apeiron*, 8(2):32 – 45, 2001.

[7] S. Shnoll, V. Kolombet, E. Pozharskii, T. Zenchenko, J. Zvereva, and A. Konradov. *Phys.Usp.*, 41, 1998.

[8] V.M. Lobashev, V.N. Aseev, A.I. Belesev, A.I. Berlev, E.V. Geraskin, et al. Direct search for mass of neutrino and anomaly in the tritium beta spectrum. *Phys.Lett.*, B460:227 – 235, 1999.

[9] D. O'Keefe, B.L Morreale, R.H Lee, John B. Buncher, J.H Jenkins, Ephraim Fischbach, T. Gruenwald, D. Javorsek, and P.A Sturrock. Spectral content of 22na/44ti decay data: implications for a solar influence. *Astrophysics and Space Science*, 344(2):297–303, 2013.

[10] J. H. Jenkins, E. Fischbach, J. B. Buncher, J. T. Gruenwald, D. E. Krause, and J. J. Mattes. Evidence of correlations between nuclear decay rates and earth-âsun distance. *Astroparticle Physics*, 32(1):42 – 46, 2009.

[11] P.A Sturrock, J.B Buncher, E. Fischbach, J.T Gruenwald, D. Javorsek, J.H Jenkins, R.H Lee, J.J Mattes, and J.R Newport. Power spectrum analysis of BNL decay rate data. *Astroparticle Physics*, 34:121–127, September 2010.

[12] P. A. Sturrock, E. Fischbach, and J. H. Jenkins. Further Evidence Suggestive of a Solar Influence on Nuclear Decay Rates. *Solar Phys.*, 272:1–10, 2011.

[13] J. H Jenkins, K. R Herminghuysen, T. E Blue, E. Fischbach, D. Javorsek, et al. Additional experimental evidence for a solar influence on nuclear decay rates. *Astropart.Phys.*, 37:81–88, 2012.

[14] J. Jenkins and E. Fischbach. Perturbation of nuclear decay rates during the solar flare of 2006 december 13. *Astroparticle Physics*, 31:407–411.

[15] J.H Jenkins, E. Fischbach, P.A Sturrock, D.W Mundy, E. Auge, J. Dumarchez, and J.T.T Van. Xlviith rencontres de moriond and gphys colloquium. *Gravitational Waves and Experimental Gravity, Gioi Publishers, La Thuile, Aosta Valley, Italy*, pages 403–408, 2011.

[16] K. J Ellis. The effective half-life of a broad beam 238 pu/be total body neutron irradiator. *Physics in Medicine and Biology*, 35(8):1079, 1990.

[17] A.G. Parkhomov. Researches of alpha and beta radioactivity at long-term observations. *ArXiv e-prints*, 2010.

[18] A.G. Parkhomov. Periods detected during analysis of radioactivity measurements data. *ArXiv e-prints*, December 2010.

[19] Y. Ryabov V. Kushniruk Y. Baurov, Y. Sobolev. *Phys.Atom.Nucl.*, 70, 2007.

[20] H. Schrader. Half-life measurements of long-lived radionuclidesânew data analysis and systematic effects. *Applied Radiation and Isotopes*, 68(7â8):1583 – 1590, 2010. Proceedings of the 17th International Conference on Radionuclide Metrology and its Applications (ICRM 2009).

[21] P. A. Sturrock, A. G. Parkhomov, E. Fischbach, and J. H. Jenkins. Power Spectrum Analysis of LMSU (Lomonosov Moscow State University) Nuclear Decay-Rate Data: Further Indication of r-Mode Oscillations in an Inner Solar Tachocline. *Astropart.Phys.*, 35:755–758, 2012.

[22] D. J. II P. Sturrock J. Jenkins, E. Fischbach. *Nucl.Instrum.Meth.*, A73, 2013.

[23] P. A. Sturrock, G. Steinitz, E. Fischbach, D. Javorsek, and J. H. Jenkins. Analysis of Gamma Radiation from a Radon Source: Indications of a Solar Influence. *Astropart.Phys.*, 36:18–25, 2012.

[24] P.A Sturrock, J.B Buncher, E. Fischbach, J.T Gruenwald, D. Javorsek, J.H Jenkins, R.H Lee, J.J Mattes, and J.R Newport. Power Spectrum Analysis of Physikalisch-Technische Bundesanstalt Decay-Rate Data: Evidence for Solar Rotational Modulation. *Solar Physics*, 267:251–265, December 2010.

[25] D. Elmore, N. Anantaraman, H.W Fulbright, H.E Gove, H.S Hans, K. Nishizumi, M.T Murrell, and M. Honda. Half-life of ^{32}Si from tandem-accelerator mass spectrometry. *Phys. Rev. Lett.*, 45:589 – 592, 1980.

[26] W. Kutschera, W. Henning, M. Paul, R.K Smither, E.J Stephenson, J.L Yntema, D.E Alburger, J.B Cumming, and G. Harbottle. Measurement of the ^{32}Si half-life via accelerator mass spectrometry. *Phys. Rev. Lett.*, 45:592–596, Aug 1980.

[27] V.N Nijampurkar, D.K Rao, F. Oldfield, and I. Renberg. The half-life of 32si: a new estimate based on varved lake sediments. *Earth and Planetary Science Letters*, 163(1 -â 4):191 – 196, 1998.

[28] Brookhaven National Laboratory National Nuclear Data Center. Nudat (nuclear structure and decay data), March 18 2008.

[29] J. Jenkins, D.W Mundy, and E. Fischbach. Analysis of environmental influences in nuclear half-life measurements exhibiting time-dependent decay rates. *Nuclear Physics B*, 2009.

[30] A. Abbady, A.G.E Abbady, and R. Michel. Indoor radon measurement with the lucas cell technique. *Appl. Radiat. Isot.*, 61:1469, 2004.

[31] Adam Bouchta. Seasonal variation of the muon flux seen by amanda. In *International Cosmic Ray Conference*, volume 2, page 108, 1999.

[32] Nepal Ramesh, Martin Hawron, Clayton Martin, and Abdel Bachri. Flux variation of cosmic muons. *arXiv preprint arXiv:1203.0101*, 2012.

[33] F. Wissmann. Variations observed in environmental radiation at ground level. *Radiation Protection Dosimetry*, 118:3–10.

[34] J.R Elliott, M.S Miesch, and J. Toomre. Turbulent solar convection and its coupling with rotation: The effect of prandtl number and thermal boundary conditions on the resulting differential rotation. *The Astrophysical Journal*, 533(1):546, 2000.

[35] N. Brummell, J. Toomre, and F. Cattaneo. Turbulent dynamics in the solar convection zone. *Science*, 269(5229):1370–1379, 1995.

[36] J. Schou, H.M Antia, S. Basu, R.S Bogart, R.I Bush, S.M Chitre, J. Christensen-Dalsgaard, M.P Di Mauro, W.A Dziembowski, A. Eff-Darwich, et al. Helioseismic studies of differential rotation in the solar envelope by the solar oscillations investigation using the michelson doppler imager. *The Astrophysical Journal*, 505(1):390, 1998.

[37] M.J Thompson, J. Toomre, E.R Anderson, H.M Antia, G. Berthomieu, D. Burtonclay, S.M Chitre, J. Christensen-Dalsgaard, T. Corbard, M. DeRosa, et al. Differential rotation and dynamics of the solar interior. *Science*, 272(5266):1300–1305, 1996.

[38] P.D.M Parker and C.E Rolfs. *Nuclear energy generation in the solar interior*, pages 31–50. 1991.

[39] E. Adelberger, S. Austin, J. Bahcall, A. Balantekin, Gilles Bogaert, L. Brown, Lothar Buchmann, F. Cecil, A. Champagne, Ludwig De Braeckeleer, et al. Solar fusion cross sections. *arXiv preprint astro-ph/9805121*, 1998.

[40] John N Bahcall. *Neutrino astrophysics*. Cambridge University Press, 1989.

[41] *Encyclopedia of Astronomy and Astrophysics*. Nature Publishing Grp., 2001.

[42] A.O Benz. Flare observations. *Living Reviews in Solar Physics*, 2008.

[43] R.C Carrington. Description of a Singular Appearance seen in the Sun on September 1, 1859. , 20:13–15, November 1859.

[44] C. Zwaan and K.L Harvey. Patterns in the solar magnetic field. *Solar Magnetic Fields*, pages 27–48, 1994.

[45] V. Gaizauskas, K.L Harvey, J.W Harvey, and C. Zwaan. Large-scale patterns formed by solar active regions during the ascending phase of cycle 21. , 265:1056–1065, February 1983.

[46] J.R Taylor. *An Introduction to Error Analysis*. University Science Books, second edition, 1997.

[47] M. Basseville and I.V Nikiforov. *Detection of Abrupt Changes: Theory and Applications*. Prentice Hall, Inc., 1993.

[48] R.B Crosier. A two-sided cumulative sum quality control scheme. *Technometrics*, Vol. 28(3):187–194, 1986.

[49] S.W Roberts. Control charts based on geometric moving averages. *Technometrics*, Vol. 42(1):97–101, 2000.

[50] A.M Mood. The distribution theory of runs. *The Annals of Mathematical Statistics*, 11(4):pp. 367–392, 1940.

[51] G.L Bertthorst. Generalising the lombscargle periodogram. AIP Conf. Preceedings, 2001.

[52] A.G Parkhomov. Effect of radioactivity decrease. Is there a link with solar flares? *ArXiv e-prints*, May 2010.

[53] A.G Parkhomov. Deviations from Beta Radioactivity Exponential Drop. *Journal of Modern Physics*, 2:1310–1317, 2011.

[54] E. Bellotti, C. Broggini, G. Di Carlo, M. Laubenstein, and R. Menegazzo. Search for correlations between solar flares and decay rate of radioactive nuclei. *Phys.Lett.*, B720:116–119, 2013.

[55] Peter A. Sturrock, Ephraim Fischbach, and Jere Jenkins. Analysis of Beta-Decay Rates for Ag108, Ba133, Eu152, Eu154, Kr85, Ra226 And Sr90, Measured at the Physikalisch-Technische Bundesanstalt from 1990 to 1996. *ArXiv e-prints*, 2014.

[56] P.A Sturrock, E. Fischbach, D. Javorsek, J.H Jenkins, R.H. Lee, J. Nistor, and J.D Scargle. Comparative study of beta-decay data for eight nuclides measured at the physikalisch-technische bundesanstalt. *Astroparticle Physics*, 59(0):47 – 58, 2014.

[57] G.T Emery. Perturbation of nuclear decay rates. *Annual Review of Nuclear Science*, 22(1):165–202, 1972.

[58] C.S Wu and S.A Moszkowski. Beta decay, interscience monographs and texts in physics and astrophsyics, edited by a, 1966.

[59] W.K Hensley, W.A Bassett, and J.R Huizenga. Pressure dependence of the radioactive decay constant of beryllium-7. *Science*, 181(4105):pp. 1164–1165, 1973.

[60] Howard R. Reiss. Nuclear beta decay induced by intense electromagnetic fields: Basic theory. *Phys. Rev. C*, 27:1199–1228, Mar 1983.

[61] T. Ohtsuki, H. Yuki, M. Muto, J. Kasagi, and K. Ohno. Enhanced electron-capture decay rate of ^{7}Be encapsulated in c_{60} cages. *Phys. Rev. Lett.*, 93:112501, Sep 2004.

[62] E. Fischbach, J.B Buncher, J.T Gruenwald, J. H Jenkins, D.E Krause, J.J Mattes, and J.R Newport. Time-dependent nuclear decay parameters: New evidence for new forces?. *Space Science Reviews*, 145(3/4):285 – 335, 2009.

[63] Wolfgang Stoeffl and Daniel J. Decman. Anomalous structure in the beta decay of gaseous molecular tritium. *Phys. Rev. Lett.*, 75:3237–3240, Oct 1995.

[64] D. Griffiths. *Introduction to Elementary Particles*. Wiley-VCH, 2004.

[65] L. Fassio-Canuto. Neutron beta decay in a strong magnetic field. *Phys. Rev.*, 187:2141–2146, Nov 1969.

VITA

VITA

Tasneem M. Mohsinally was born in Colombo, Sri Lanka on June 28, 1985. In 2007 she graduated with Highest Distinction from Purdue University in West Lafayette, IN with a Bachelor of Science in Physics. She entered the doctoral Physics program in the Department of Physics and Astronomy at Purdue University in the fall of 2007 with the Chappelle Fellowship and received a Masters of Science degree in December 2009. During her time at Purdue University from 2008 to 2014, she was a teaching assistant for several graduate and undergraduate courses and also served as lead instructor for a graduate level course. She received her Ph.D in phenomenology/computational physics in May 2015 from Purdue University.